

# Electronic Multi-material Fibers and Textiles: Novel Designs and Applications

Présentée le 4 mars 2021

Faculté des sciences et techniques de l'ingénieur  
Laboratoire des fibres et matériaux photoniques  
Programme doctoral en science et génie des matériaux

pour l'obtention du grade de Docteur ès Sciences

par

## Chaoqun DONG

Acceptée sur proposition du jury

Prof. J. Brugger, président du jury  
Prof. F. Sorin, directeur de thèse  
Prof. X. Tao, rapporteuse  
Prof. L. Wei, rapporteur  
Prof. S. Lacour, rapporteuse

*To my family*

## Acknowledgements

First of all, I would like to express my deepest gratitude to my supervisor Professor Fabien Sorin, for giving me such a golden opportunity to start my PhD journey and work on such an exciting field. His enthusiasm and interest toward research inspire me to build a correct academic attitude; his trust and vision always encourage me to explore challenging projects; his training and guidance make me a better and independent researcher; his expertise offers me deep insight into the projects. The knowledge and attitude I learned from him, not only in scientific work but also in many other aspects in life, are critical to reshape my career and are highly valuable in my life.

I am grateful to Prof. Stéphanie Lacour, Prof. Xiaoming Tao, Prof. Lei Wei and Prof. Jürgen Brugger for accepting to be members in my thesis. Their insights and comments are highly valuable for this thesis. In particular, Prof. Lacour was also the expert in my candidacy exam committee and the annual meetings. She could always give valuable comments on my work during our discussion and stimulate my deeper thinking on the projects.

It was a great honor to work in the warm and cooperative FIMAP group with the amazing people here. It is difficult to find a word to describe them. Colleagues? Friends? They are indeed my second family members! It was them who helped me and warmed me up to get through some “dark time”. I enjoyed a lot of the relaxed atmosphere created by their great sense of humor, and also the serious environment as we concentrate on work. I would like to thank my elder brothers Dr. Tung Nguyen-Dang, Dr. Wei Yan, Dr. Yunpeng Qu, Dr. Tapajyoti Das Gupta, Dr. Bastien Schyrr and sister Dr. Federica Sordo, who kindly helped me to get familiar with everything in FIMAP, supported my research and encourage me to keep confidence. I am also thankful to Shahrzad Shadman Yazdi, Nicola Bartolomei, Louis Marie Philippe Martin-Monier and Inès Richard, who have accompanied me for this “four years’ marathon” and brought a lot of happiness, laughter and precious memories. It is also a great pleasure to work with Dr. Rajasundar Chandran, William Esposito, Pierre-Luc Eloi Piveteau, Marco Volpi and Hritwick Banerjee. I would like to express particular thanks to my officemate Andreas Leber. I cannot imagine how I could finish my projects without his kind help and I enjoyed a lot of our fruitful and stimulating discussions on research. I could not have imagined having a better officemate. I would like to give a big hug to our Swiss mother Anne Roy, who is always efficient and kind to help dealing with many problems!

This thesis could not have been accomplished without the support and help of the following professors and researchers: Prof. Pedro Reis, Dr. Dong Yan from FLEXLAB, for the fruitful collaboration and finite element analysis in my project; Prof. Xiaosheng Zhang from LMIS1, who answered me many questions on triboelectric nanogenerators as I just stepped into this field; Dr. Enrico Colla, who was always there to offer support whenever I have problems on LabView; Prof. Esther Amstad from SMaL, who kindly offered me access to their instruments; Dr. Huachuan Du, Michael David Kessler, Mathias Steinacher, Matteo Hirsch, who helped me on some characterizations; Prof. Véronique Michaud and Dr. Yves Leterrier from LPAC, who provided me access to their machines; Dr. Kyungjin Kim, who offered valuable help on the water vapor transmission experiment; Michael Giffin and Shuichi Haraguchi from LMOM, who always offer me help on using the micro-extruder; Dr. Giuseppe Schiavone, Michael Shur, for their discussion with me on soft materials and bioengineering; Prof. Yuanyuan Guo from Tohoku University for sharing with me her experience on conductive composites and neuroengineering; Dr. Nadezda Pankratova from LSI and Dr. Lei Zhang from LSCI, for their support on electrochemistry. In addition, I would like to acknowledge master students Luca Francesco and Tao Zhang, who worked with me on their semester project.

My sincere thanks also go to my Chinese friends in Switzerland, thank you all for your patient listening, offering me advice, and accompanying me to travel and explore many places in Europe through this entire journey. Special thanks to Huayan Yang, Lulu Liu, Shiyu Sui, Jun Ma, Tingyong Jiang, Zhaoyang Wang, Ya Wang, Minghua Zhu, Xiaotong Du, Chengmin Li, Wenjiao Xie, Zonglei Li, Zhangli Hu, Jiangtao Zhao, Siyu Chen, Xianwei Wang, Guoxiong Zheng. Also, I express my thanks to my friends scattered around the world, thank you for your caring, phone calls, visits and valuable advice, and always being there whenever I needed a friend. In particular, I wish to acknowledge my previous supervisor Prof. Zhonghua Zhang in Shandong University, who enlightened me the first glance of research and is always very delighted to offer me continuous and insightful support and suggestions about research and my career.

Finally, I would also like to show my deep appreciation to my parents for their love, caring and sacrifices for educating me. I am very much thankful to my partner Yawen for his love and understanding. I am very grateful for the support from my family on my decision to pursue my PhD in Switzerland, even it means I am always away. This thesis is dedicated to you!

## Abstract

Flexible electronics and particularly soft fibers and textiles are becoming key components in rapidly developing fields such as robotics, health and personal care, sensing, or implantable and wearable devices. Thus far however, the ability to impart soft and stretchable fibers with advanced electronic functionalities, including efficient energy harvesting, remains limited. The recent development of the concept of multi-material fiber drawing has opened novel opportunities in the integration of novel materials and their organization into complex architectures, resulting in unexpected functionalities. Yet, two limitations have resisted this line of research: using fiber-based constructs for advanced microfluidics, and demonstrating state-of-the-art fibers and textiles for energy harvesting and self-powered sensing. In this thesis, via a combination of fundamental understanding and engineering of materials processing, rheology, mechanical and electrical engineering, we significantly advanced the range of materials, architectures and functionalities achievable for multi-material electronic fibers. We in particular achieved three main objectives. First, we demonstrate a uniform capillary-like fiber that integrates an encapsulated micro-channel and an embedded capacitor system within a polymeric cladding. It shows versatile functionalities applicable to microfluidic sensing including the monitoring of the presence and travel distance of a fluid, real-time sensing of a wide range of flowrate, and high-accuracy identification of the static dielectric constant of fluid. We then demonstrate the scalable fabrication of advanced triboelectric fibers that combine a micro-textured elastomer surface with the integration of several liquid metal electrodes. Such fibers exhibit high efficiencies on par with planar systems regardless of repeated large deformations. They can be woven into machine-washable textiles with high electrical outputs up to 490 V, 175 nC. We also demonstrate their self-powered breathing monitoring and gesture sensing capabilities. The third objective arose in the course of the second project – attempting to circumvent the limitations associated with single-electrode triboelectric fibers and unravel more activation states of the devices. We design and fabricate a stretchable multi-material contact-separation mode triboelectric fiber that can generate electricity from reversible compression and stretching. The fiber is constituted of two stretchable and conductive composite-based micro-structured triboelectric parts, which are separated by a large gap and surrounded by a water repellent elastomeric cladding. Finite element analysis is performed to deeply understand the kinetic deformations of the fiber system, and show the level of control and engineering of the mechanical behaviors that can be achieved through application-targeted fiber designs. The novel triboelectric fiber designs that we propose, the unprecedented simplicity and throughput of the manufacturing process, together with the inherent

deformability and excellent electrical outputs of the demonstrated fibers and textiles, alleviate the challenges associated with the integration of high performance energy-harvesting systems within soft and wearable constructs. With novel sensing and energy harvesting soft fibers, the results of this thesis pave the way towards novel devices and applications in health and personal care, implantable systems and wearable devices.

**Keywords:** thermal drawing, multi-material fibers, functional fibers, electronic devices, sensing, microfluidics, triboelectric nanogenerators, energy harvesting, smart textiles, finite element analysis.

## Résumé

Les composants électroniques flexibles et en particulier les fibres et textiles souples sont devenus des composants clés dans des domaines en développement rapide tels que la robotique, la santé et soins personnels, la détection et les dispositifs implantables et portables. Jusqu'à présent cependant, la capacité à intégrer des fonctionnalités avancées, telles que la récupération efficace d'énergie, dans des fibres souples et extensibles reste limitée. Le développement récent du tirage à chaud a ouvert la voie à l'intégration de nouveaux matériaux organisés en architectures complexes, aboutissant à des fonctionnalités inattendues. Pourtant, deux limites ont résisté à cette ligne de recherche: l'utilisation de ces fibres pour la microfluidique avancée et la conception de fibres et de textiles de pointe pour la récupération d'énergie et la détection autoalimentée. Dans cette thèse, nous avons fait de considérables progrès en terme de diversité des matériaux, d'architectures et de fonctionnalités réalisables dans des fibres électroniques, grâce à une combinaison de compréhension fondamentale et d'ingénierie de la fabrication de matériaux, de la rhéologie et du génie mécanique et électrique. Nous avons en particulier atteint trois objectifs principaux. Premièrement, nous démontrons une fibre capillaire uniforme qui intègre un micro canal et un système de condensateur dans une gaine polymère. Elle présente des fonctionnalités polyvalentes applicables à la détection microfluidique, telles que le monitoring de la présence et de la distance de déplacement d'un fluide, la détection en temps réel d'une large plage de débits et l'identification précise de la constante diélectrique statique du fluide. Ensuite, nous démontrons la fabrication à haut rendement de fibres triboélectriques sophistiquées qui combinent une surface micro-texturée et des électrodes en métal liquide. De telles fibres présentent des rendements électriques élevés, comparables aux systèmes planaires, même après de grandes déformations répétées. Elles peuvent également être tissées en textiles déformables lavables en machine avec des puissances électriques élevées jusqu'à 490 V, 175 nC. Nous démontrons aussi leur capacité de surveillance respiratoire et de détection de mouvement autoalimentée. Le troisième objectif est apparu au cours du deuxième projet : tenter de contourner les limitations associées aux fibres à électrode unique et d'augmenter la diversité des modes de stimuli. Nous concevons une fibre triboélectrique multi matériaux extensible en mode de séparation de contact qui peut générer de l'électricité à partir de compressions et étirements réversibles. La fibre contient deux composants triboélectriques composites micro structurés étirables et conducteurs, qui sont séparées par un grand espace et entourés par une gaine élastomère hydrofuge. Une analyse par éléments finis est effectuée pour comprendre les déformations des fibres et montre le niveau de contrôle et d'ingénierie du comportement mécanique possible via la conception de fibres pour des applications

spécifiques. La nouvelle géométrie des fibres triboélectriques, la simplicité et le haut rendement du procédé de production, ainsi que la déformabilité et les excellentes performances électriques de nos fibres et textiles, répondent aux défis associés à l'intégration de systèmes de récupération d'énergie de haute performance dans des produits souples et portables. Avec ces fibres flexibles de détection et récupération d'énergie, les résultats de cette thèse ouvrent la voie à de nouveaux dispositifs et applications dans les domaines de la santé et des soins personnes, des systèmes implantables et dispositifs portables.

**Mots-clés:** tirage à chaud, fibres multi matériaux, fibres fonctionnelles, systèmes électroniques, détection, microfluidique, nano générateurs triboélectriques, récupération d'énergie, textiles intelligents, analyse par éléments finis.



## List of abbreviations

<b>CNT(s)</b>	Carbon nanotubes
<b>COCE</b>	Cyclic olefin copolymer elastomer
<b>CPE</b>	Carbon-black filled polyethylene
<b>MEMS</b>	Microelectromechanical systems
<b>PC</b>	Polycarbonate
<b>PEI</b>	Polyetherimide
<b>PMMA</b>	Poly(methyl methacrylate)
<b>PSu</b>	Polysulfone
<b>PS</b>	Polystyrene
<b>PTFE</b>	Polytetrafluoroethene
<b>PVDF</b>	Polyvinylidene fluoride
<b>P(VDF-TrFE)</b>	Poly(vinylidene fluoride-trifluoroethylene) copolymer
<b>P(VDF-TrFE-CFE)</b>	Poly(vinylidene fluoride-trifluoroethylene-chlorofluoroethylene) terpolymer
<b>SEBS</b>	Poly(styrene-b-(ethylene-co-butylene)-b-styrene)
<b>TENG(s)</b>	Triboelectric nanogenerator(s)
<b>WVTR</b>	Water vapor transmission rate

# Contents

Acknowledgements .....	i
Abstract .....	iii
Résumé .....	v
Chapter 1 Introduction.....	1
1.1 Advanced fiber electronics .....	1
1.2 Multi-material thermal drawing .....	2
1.3 Multi-material electronic fibers.....	5
1.3.1 Conductive materials.....	5
1.3.2 Semiconductors .....	8
1.3.3 Dielectric materials.....	9
1.4 Soft multi-material electronic fibers.....	11
1.5 Objectives and outline of the thesis.....	14
Chapter 2 Microstructured multi-material fibers for microfluidic sensing .....	18
2.1 Fiber fabrication .....	19
2.2 Capacitive behavior of the fiber device.....	20
2.3 Discussion on the flowrate detection function .....	22
2.4 Discussion on the static dielectric constant detection function .....	25
2.5 Methods .....	27
2.6 Summary .....	28
Chapter 3 High-efficiency super-elastic liquid metal based triboelectric fibers and textiles .....	30
3.1 Materials characterization and fiber fabrication.....	32
3.2 Working mechanism.....	37
3.3 Electrical output performance of triboelectric fibers.....	39
3.4 Woven triboelectric textiles for energy harvesting.....	43

3.5 Demonstration of wearable applications of triboelectric fibers and textiles .....	50
3.6 Methods .....	52
3.7 Summary .....	54
Chapter 4 Design and fabrication of self-encapsulated and stretchable multi-material triboelectric fibers.....	56
4.1 Identification and characterization of the encapsulating material .....	58
4.2 Fabrication and characterization of stretchable and conductive electrodes.....	61
4.3 Fiber microstructure engineering, processing and characterization .....	65
4.4 Methods .....	73
4.5 Summary .....	74
Chapter 5 Electrical and mechanical properties of contact-separation mode soft triboelectric fibers	76
5.1 Electrical output performance under compression .....	77
5.2 Finite element analysis of the mechanical deformation under compression .....	84
5.3 Energy harvesting from other mechanical stimuli.....	90
5.4 Methods .....	93
5.5 Summary .....	93
Chapter 6 Conclusions.....	96
6.1 Conclusions .....	96
6.2 Novel perspectives: Hydrogel-integrated functional fibers .....	98
Bibliography .....	101
Curriculum Vitae .....	114

# Chapter 1 Introduction

In this chapter, we will first present an in-depth review of the field of electronic fibers, and focus on thermally drawn multi-material fibers. This will give an overview of the materials, processes and type of electronic functionalities that can be imparted to fibers. We will then identify two areas where the tremendous potential of electronic thermally drawn fibers was yet to be exploited: capacitive-based microfluidic sensing and triboelectric energy generation and self-powered monitoring. We will then expose the thesis objectives and briefly summarize the content of the following chapters. Some parts of this chapter are adapted from a publication in Materials Today, for which I am a co-author.<sup>1</sup>

## 1.1 Advanced fiber electronics

Advanced devices with electronic and optoelectronic functionalities are realized through the integration of multiple materials with significantly different properties that are precisely organized within prescribed configurations. Benefiting from the combined advances in material science, mechanical and electrical engineering, these devices are currently evolving from typical planar and rigid systems to flexible and ultimately stretchable structures, enabling a seamless interfacing of electronics within our daily life.<sup>2-4</sup> Applications of such innovations include sensing<sup>5</sup> and health monitoring,<sup>6</sup> therapeutic diagnosis and treatment,<sup>7</sup> implants<sup>8,9</sup> and prosthesis<sup>10</sup>, soft robotics,<sup>11</sup> human-machine interactions,<sup>12</sup> as well as energy harvesting<sup>13</sup> and storage<sup>14</sup>.

Among different device strategies, fibers are envisioned as versatile platforms that can offer unique properties and functionalities, given their peculiar geometry, high aspect ratio, ability to be integrated into soft fabrics or tissues, as well as excellent adaptability to curved lines and surfaces, and to dynamic movements.<sup>15</sup> However, the integration of multiple materials and intricate architectures within thin fibers still remains a challenge from both scientific and engineering point of views. This is partially because the state-of-the-art processing techniques, such as photolithography and nanoimprinting, typically used for planar and rigid wafer-like substrates, are not well applicable for long, thin and extremely curved fiber structures.

Current fiber manufacturing techniques include extrusion, electrospinning and melt spinning. However, the produced fibers are usually of simple architectures and single material, and can only be

endowed with functionalities after being processed with other, often complex, methods. The approaches include, but not limited to, wrapping, dip coating, spin coating, physical vapor deposition, anodization, electrochemical deposition, and hydrothermal synthesis.<sup>16</sup> Different from planar devices with typical stacking structures, these fiber constructs usually feature coaxial, twisted, and interlaced configurations. It is highly encouraging that decades of research has led to numerous advanced electronic fiber devices, such as biosensors, supercapacitors, batteries, nanogenerators, solar cells, light-emitting electrochemical cells, or light-emitting devices.<sup>17</sup>

Despite the capability of exploiting various well-established materials, most of the approaches entail multi-step and complex processes, which is labor-intensive and has not yet demonstrated a strong potential for scalability. In addition, the fabrications only allow for simple geometries, and the performances might vary along the fiber length. It is highly possible that the coated film or nanoparticles would suffer from the vulnerabilities to delaminate or break under large deformation conditions, such as during weaving, wearing or washing manipulations for wearable electronics, which might lead to structural collapse and ultimate failure of the devices.

## **1.2 Multi-material thermal drawing**

Among various fiber processing approaches, preform-based thermal drawing is an efficient and scalable technique for the fabrication of multi-material fibers with complex architectures at micro- and nano-scale feature sizes and with multiple functionalities. It is the conventional industrial approach to fabricate optical fibers at extremely scale. For a long time, this method was restricted to single material, simple geometry and larger feature sizes. In the last two decades, this field has experienced a revolutionary expansion, driven by the demonstration of the multi-material concept in 2002. The fiber consisted of 21 alternative layers of polymer and chalcogenide glass that surround a polymer core, creating a Bragg mirror that can guide light at desired wavelengths inside the fiber.<sup>18</sup> The next milestone was made by M. Bayindir and F. Sorin et al., who developed the first in-fiber metal-insulator-semiconductor optoelectronic device. Composed of an amorphous semiconductor core contacted by metallic wires, and surrounded by a cylindrical-shell resonant optical cavity, the fiber was sensitive to illumination along its entire length of potentially kilometers.<sup>19</sup>

As schematically shown in Figure 1.1a, the thermal drawing technique typically starts with the preparation of a multi-material preform, which is a macroscopic version of the predesigned fiber. The

preform is subsequently fed into a closed furnace and heated over the materials' glass transition temperature. As the viscosities of the materials decrease by several orders of magnitudes, the bottom region of the preform necks down pulled by its own weight or with an attached extra weight. The fiber, once coming out of the furnace, is rapidly quenched and can be attached to capstan that continuously pull at a constant speed to draw hundreds of meters of fiber. The dimension and internal stress of the fiber can be well controlled by the temperature distribution in the furnace, the feeding velocity of the preform, as well as the drawing speed of the fiber. Unless otherwise engineered, the fiber retains exactly the same composition and geometry as the initial preform, but with smaller sizes in the transverse dimensions, and longer in length.

This technique exhibits several distinctive features. 1) Since the preform is made at the millimeter or centimeter scales, complex cross-sectional architectures and the precise arrangement of materials and micro-devices can be easily realized. Inheriting the features of the preform, the resulting fibers can therefore be endowed with complex structures. 2) Fibers with sub-microscale and even nanoscale feature sizes can be achieved, which is particularly important for some applications. For instance, a deep understanding of the fluidic dynamics during drawing has enabled the fabrication of sub-micrometer structures on 2D surfaces or 3D structures. It was demonstrated that such textured fibers can create enhanced hydrophobicity surfaces, and can exhibit interesting optical effects for large-scale and flexible surfaces and textiles. Textured fibers are also capable of working as templates for the growth and alignment of biological cells (Figure 1.1b).<sup>20</sup> Recently, W. Yan and I. Richard et al. could thermally draw well-ordered and uniform metallic glasses with feature sizes down to tens of nanometers and aspect ratio greater than  $10^{10}$ , which exhibited particular promise as electrodes for high-performance optoelectronic fibers and textiles, as well as implantable probes for stable brain-machine interfaces (Figure 1.1c).<sup>21</sup> 3) A deeper look into the rheological properties of materials has enabled the exploration of novel processable materials. For instance, different biodegradable polymers compatible with thermal drawing have been identified and successfully processed. Figure 1.1d shows the fabricated microstructured poly(D,L-lactic-co-glycolic acid) (PLGA) biodegradable fibers with advanced and predictable release profiles of different drugs.<sup>22</sup> The discovery of such biodegradable polymers has established a novel platform for fibers used for sutures, implants, or tissue scaffolds. 4) From the perspective of manufacturing, thermal drawing enables the scaling down of a preform into kilometer-long fibers in a short time, which reveals industry-relevant scalability and yield. 5) While these fibers

can be used alone, they can also be easily incorporated into woven fabrics given their extended length and unique mechanical attributes.

The recent scientific and technological breakthroughs on thermal drawing have significantly advanced the field of multi-material fibers, allowing the realization of fibers with new materials, sophisticated architectures, novel functionalities, better performances as well as a wide range of innovative applications. In what follows, we will go deeper in the review of recently developed fibers with advanced electronic properties, as well as fibers with soft, elastomeric claddings.

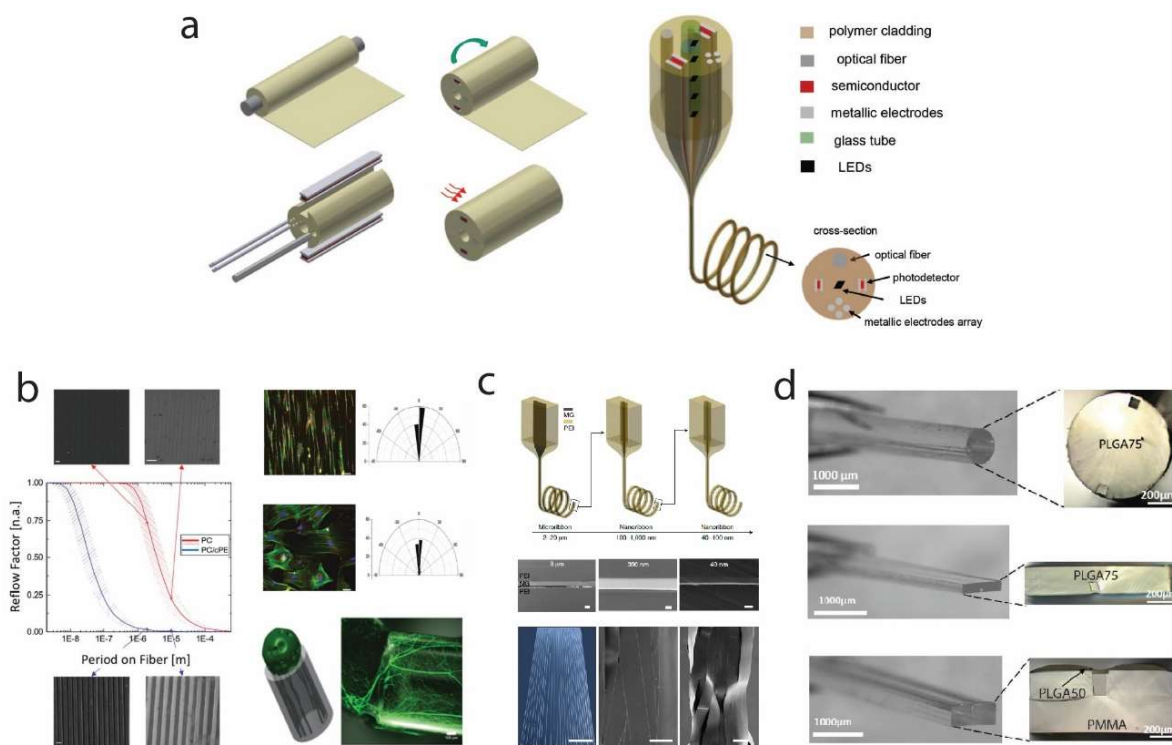


**Figure 1.1** (a) Schematic showing the thermal drawing of multi-material fibers with various embedded materials and functionalities.<sup>16</sup> (b) Graph showing the reflow factor and SEM images for textured fibers with (bottom) and without (top) a CPE sacrificial layer.<sup>20</sup> The right images show the alignment of adipose-derived stem cells on textured fiber surfaces and the growth of dorsal root ganglions inside a textured hollow conduit. (c) Fabrication of long and uniform micro- and nanoscale metallic glasses via thermal drawing.<sup>21</sup> (d) Optical microscopy images showing several fiber structures integrated with biodegradable materials.<sup>22</sup>

### 1.3 Multi-material electronic fibers

In this section, we will structure the discussion into three parts, based on the main functional materials typically integrated within fiber devices: 1) metals and polymer composites with high electric conductivities as electrodes or resistors; 2) semiconducting materials; 3) insulating materials that are used for their dielectric properties.

#### 1.3.1 Conductive materials

Low melting point metals and alloys are commonly used as conductive materials in thermally drawn fibers.<sup>19</sup> They are melt during the drawing and flow within their predefined channels acting as an encapsulation within highly viscous polymer boundaries. As an alternative to crystalline metals, the integration of various carbon filled polymer composites has not only broadened the materials choices for electrodes, but also enabled new electronic functionalities such as resistors or electrodes for neural interrogation. For example, the versatile fiber drawing technique allows an integration of multiple interrogation modalities including conductive polymer composite electrodes, optical waveguides and microfluidic channels (Figure 1.2a). Such fibers enable simultaneous long-term *in vivo* recordings, optogenetic stimulation and pharmacological modulation of neural circuits in the brain.<sup>23</sup> Implanting similar fiber probes in the spinal cord also allows the optical control of limb movements by correlating evoked neural activity with behavior responses.<sup>24</sup> However, the spatial recording resolution of such probes is relatively poor due to the low electrical conductivity of carbon-black filled polyethylene (CPE) composites. One improvement for this limitation was achieved by introducing carbon nanofibers into CPE composites, and the *in situ* unidirectional alignment of the nanofibers during fiber processing results in drastically increased electrical conductivity along the fiber longitudinal direction (Figure 1.2b). The resulting probe exhibited a miniature footprint, with an achievable recording site down to the size of a single neuron, but still with proper impedance for high-quality neural recording.<sup>25</sup> Metallic glasses form a unique class of materials that combine high electrical conductivities comparable to their crystalline counterparts, and thermal drawing compatible rheological features. They have enabled new advanced all-in-fiber neuro-probes. In addition to long-term recordings, such fiber devices are capable of *in vivo* electrical stimulation for more than three months, a feature that has never been demonstrated using other conductors in fiber platforms.<sup>21</sup>



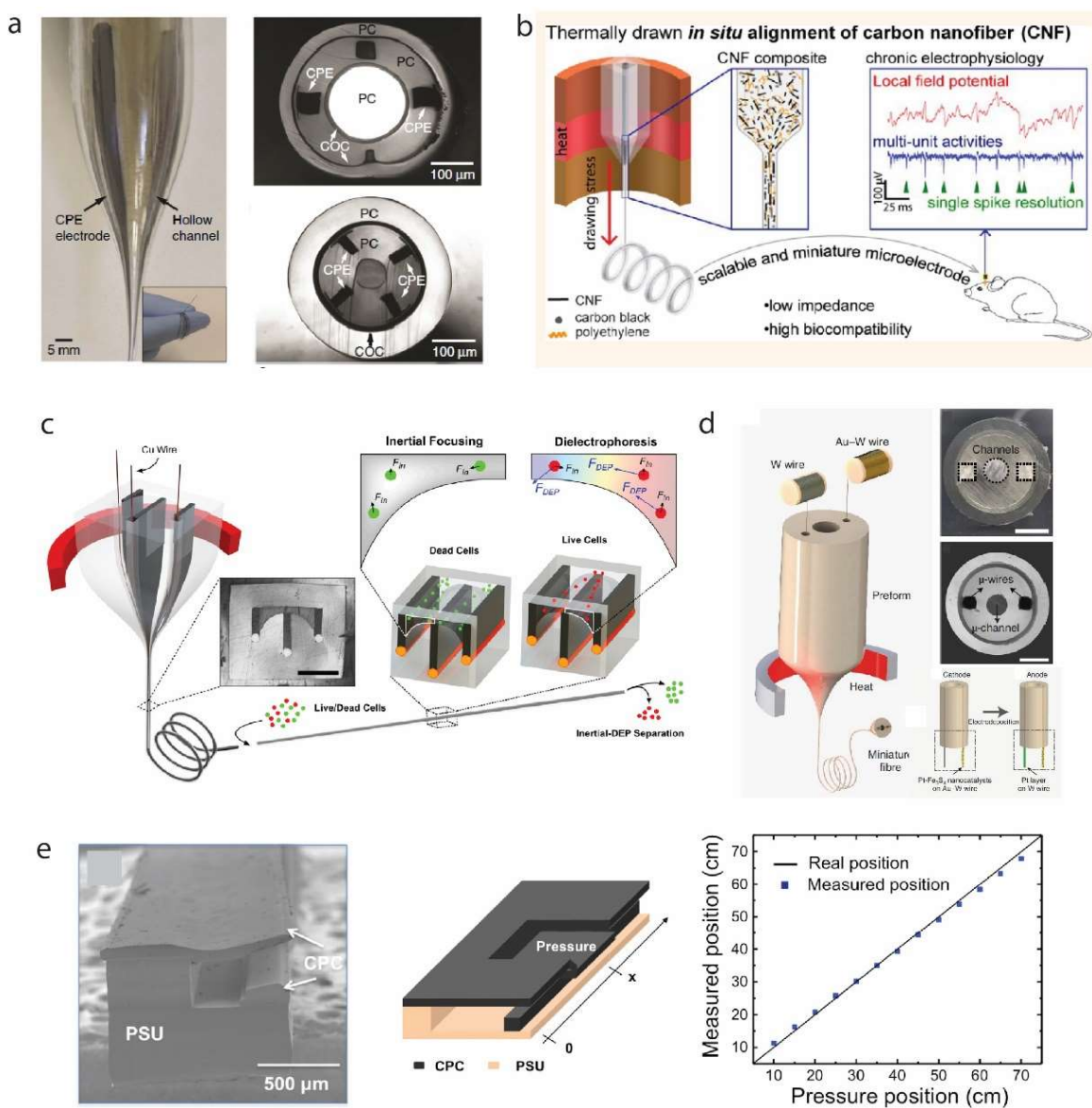


**Figure 1.2** (a) Examples of the structure of a preform together with thermally drawn fibers that integrate waveguides, composite electrodes and microchannels for neural interrogation.<sup>23</sup> (b) In situ alignment of carbon nanofibers within CPE during drawing yields enhanced electrical conductivity and thus enables chronic neural interfaces with miniature footprint.<sup>25</sup> (c) Inertial-dielectrophoretic particle manipulation fiber as a microfluidics system for high-throughput cell separation.<sup>26</sup> (d) Multi-material fibers functioned with on-demand electrochemical generation of nitric oxide for neural modulation.<sup>27</sup> (e) Electromechanical fiber for the detection and localization of pressures based on conductive polymer electrodes in cantilever-like polymeric structure.<sup>28</sup>

Another interesting use of conducting materials beyond electrodes are the dielectrophoretic effect they can create, or temperature sensing capabilities, in the context of advanced microfluidic devices. While being versatile, conventional planar microfluidic systems are still restricted by the size of silicon wafers, and in the limited control over geometry and positioning of microchannels. The inherent scalability and design freedom over the cross-sectional geometry make thermally drawn fibers an intriguing microfluidics platform. R. Yuan et al. have fabricated microfluidic fibers with complex microchannel shapes, including crosses and stars, in order to study the inertial particle focusing behavior in the channels. Additional functional elements could be integrated and coupled with the microchannels for new applications. For instance, by incorporating conductive materials along the surface of a crescent-shaped channel, an optimized inertial-dielectrophoretic particle manipulation fiber for high-throughput cell separation was realized (Figure 1.2c).<sup>26</sup> Another appealing example is a fiber-based micro-flowrate sensor, which incorporates a hollow microfluidic channel and an adjacent temperature-sensitive CPE film within a polymeric insulator matrix.<sup>29</sup> It exhibited higher sensitivity, smaller temperature rise and pressure drop compared to standard MEMS sensors. The creation of these fiber-based microfluidic devices has opened new possibilities for the application of lab-in-fiber technologies in chemical, biochemical and medical fields.

In-fiber conducting materials were also recently used in the context of electrochemical systems. Lee et al. recently invented fiber-based Li-ion batteries and supercapacitors by designing thermal drawing compatible electrodes and electrolyte gels.<sup>30</sup> Each gel domain includes a porous host matrix material and an entrapped ionically conducting liquid solvent component, which provides good electron and ion conductivities and thus exhibits sufficient electrochemical activities in operation. Also, the convergence drawing method has brought new functions and applications, for example diode fibers for all fabric based optical communications<sup>31</sup>, copper wire embedded transmission lines for distributed sensing<sup>32</sup>. As shown in Figure 1.2d, by combining convergence drawing and post-drawing processing approach, an electrocatalytic system, centered in Pt and Pt-Fe<sub>3</sub>S<sub>4</sub> nanoclusters decorated W and Au-W wires, was implemented in thermally drawn multi-material fibers, which allows on-demand in situ electrochemical generation of nitric oxide for neuronal modulation.<sup>27</sup>

Finally, another function of polymer composites with significant lower electrical conductivities compared to metal, is to serve as resistors to control the potential drop along a fiber device. For instance, conductive polymer composite sheets placed opposite to one another in a bendable cantilever-like

polymer structure are capable of detecting and localizing pressures along the fiber.<sup>28</sup> As shown in Figure 1.2e, under a mechanical load, the initially separated conductive domains are brought in contact, acting as a switch in an electrical circuit. The pressure position is determined by measuring the electrical load of this circuit, which depends linearly on the distance from the contact point to the interrogated fiber end.

### 1.3.2 Semiconductors

Semiconductors have been integrated in multi-material fiber to fabricate optoelectronic,<sup>33,34</sup> thermoelectric and thermal sensing, or phase change devices. The unique combination of metals, semiconductors and insulators into fibers enables optoelectronic functionalities over large-area substrates for applications including photosensing,<sup>19</sup> lensless imaging,<sup>35</sup> chemical sensing<sup>36</sup> and optical communications<sup>31</sup>. While we emphasize on electronic devices in this thesis, more details on the optoelectronic fibers have been discussed in our review paper.<sup>1</sup> The integration of thermally sensitive semiconductors, whose electrical conductivity varies with the surrounding temperature, into fibers has allowed the detection of temperature changes over large areas. The first multi-material thermal sensing fiber involved a  $\text{Ge}_{17}\text{As}_{23}\text{Se}_{14}\text{Te}_{46}$  glass, intimately contacted with four  $\text{Sn}_{96}\text{Ag}_4$  metallic electrodes (Figure 1.3a).<sup>37</sup> Incorporated into fabrics or any other host structure, it is capable of localizing the source of a thermal excitation with a high spatial resolution. Another example involves the processing of crystalline thermoelectric materials within a glass tube, as shown in Figure 1.3b. Two types of thermoelectric fiber generators covered on different curved surfaces were constructed, which can provide a  $\text{mW}/\text{cm}^2$ -level output power density. A wearable two-dimensional active-cooling textile with a maximum cooling rate of  $5\text{ }^\circ\text{C}$  was also assembled with these thermoelectric fibers.<sup>38</sup>

Materials that exhibit reversible amorphous/crystalline phase transitions under applied electric fields are extensively used in modern data storage media. The ideal trade-off between the high thermal stability required for processing and the low stability needed for phase change was established for high tellurium-content glasses ( $\text{Ga}_{10}\text{Ge}_{15}\text{Te}_{75}$  and  $\text{Ge}_{22}\text{As}_{18}\text{Se}_{15}\text{Te}_{45}$ ) and ovonic memory-switching fibers were realized (Figure 1.3c).<sup>39</sup> An electric field generated by adjacent metallic electrodes in the fiber can modulate the electronic structure of the semiconductor domain, leading to a reversible switching between a high resistance (OFF) and a low resistance state with a difference of four orders of magnitude. Beyond this, the in situ phase transition of a glassy chalcogenide compound ( $\text{As}_{40}\text{Se}_{52}\text{Te}_8$ ) from its amorphous to

crystalline state allows the construction of a fiber-based p-channel field-effect device (Figure 1.3d).<sup>40</sup> It is envisioned that the processing of such materials could implement complex circuits along kilometer-long fibers and further contribute to crossbar fabric-array flexible electronic devices.

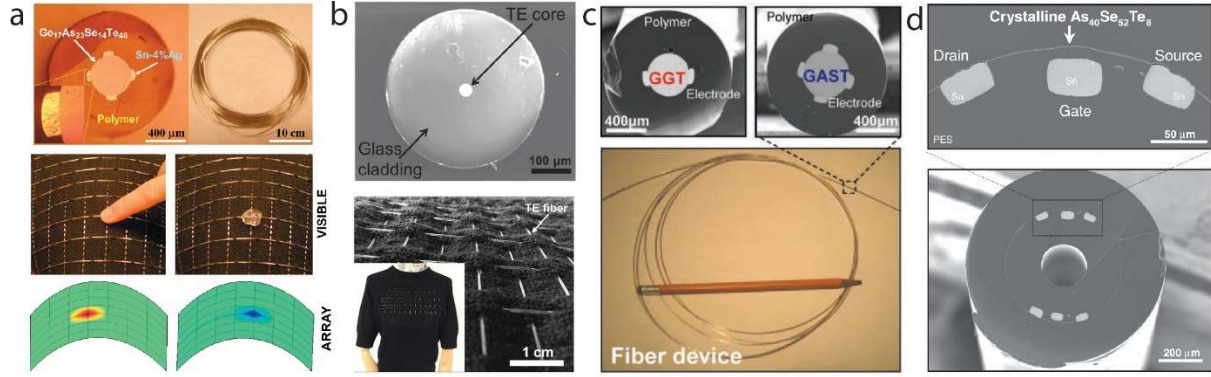


**Figure 1.3** (a) Images showing the cross-section and length of a thermal-sensing fiber (top). Fiber arrays to detect the localized heating by the touch of a finger and cooling with an ice cube (bottom).<sup>37</sup> (b) Image of the structure of a crystalline thermoelectric fiber with a glass cladding (top). A wearable thermoelectric fabric assembled with these fibers (bottom).<sup>38</sup> (c) Fibers with phase-change high tellurium-content chalcogenide glass and metallic electrodes for ovonic memory switch.<sup>39</sup> (d) Fiber field-effect device with Sn electrodes and an in situ crystallized  $\text{As}_{40}\text{Se}_{52}\text{Te}_8$  film.<sup>40</sup>

### 1.3.3 Dielectric materials

The combination of electrically conductive electrodes with dielectric materials in fibers allows the construction of various capacitive fiber devices. Owing to the high dielectric constant, poly(vinylidene fluoride) (PVDF) is a particularly promising dielectric material in the multi-material thermal drawing field. For instance, all-in-fiber capacitors with a low-loss capacitive behavior of up to 20kHz were demonstrated, by sandwiching a PVDF thin film between CPE electrodes.<sup>41</sup> Optimizing the design of the fiber architecture by folding a wide PVDF film shows increased capacitances up to 47 nF m<sup>-1</sup> (Figure 1.4a). A further increase in capacitance of 100 nF m<sup>-1</sup> was achieved through a swiss-roll like structure, where two dielectric and two conductive polymer layers were rolled up together (Figure 1.4b). The sub-millimeter thick fiber containing 30 layers could additionally function as a 1D touch sensor (Figure 1.4c). By integrating an array of the capacitive fibers into a woven textile, a touchpad sensor without inter-channel crosstalk was also demonstrated.<sup>42</sup>

P(VDF-TrFE), as a copolymer of the piezoelectric poly(vinylidene fluoride), has opened the door to a novel generation of fiber-based acoustic transducers that can be used both in emission and reception modes over frequency ranges spanning from Hertz to Megahertz.<sup>43</sup> The challenges that the thermal drawing process poses could be overcome with this material, because it can be confined in its low-viscosity state surrounded by highly viscous composite electrodes, and subsequently crystallizes directly into its ferroelectric phase without necessitating any mechanical stress. The transducer performance could be improved through targeted modifications in the design of the fiber architecture, including the maximization of the active surface area through the use of interdigitated electrodes (Figure 1.4d).<sup>44</sup> The benefit of imparting the piezoelectric functionality to fibers is significant given the collective effect of fiber arrays, which enables coherent interference and beam steering as a transmitter<sup>44</sup> and acoustic positioning as a receiver<sup>45</sup>. Realizing such a functionality at large scale offered by thermal drawing represents an attractive prospect for applications in flow monitoring, acoustic communication, and energy conversion.<sup>43</sup>

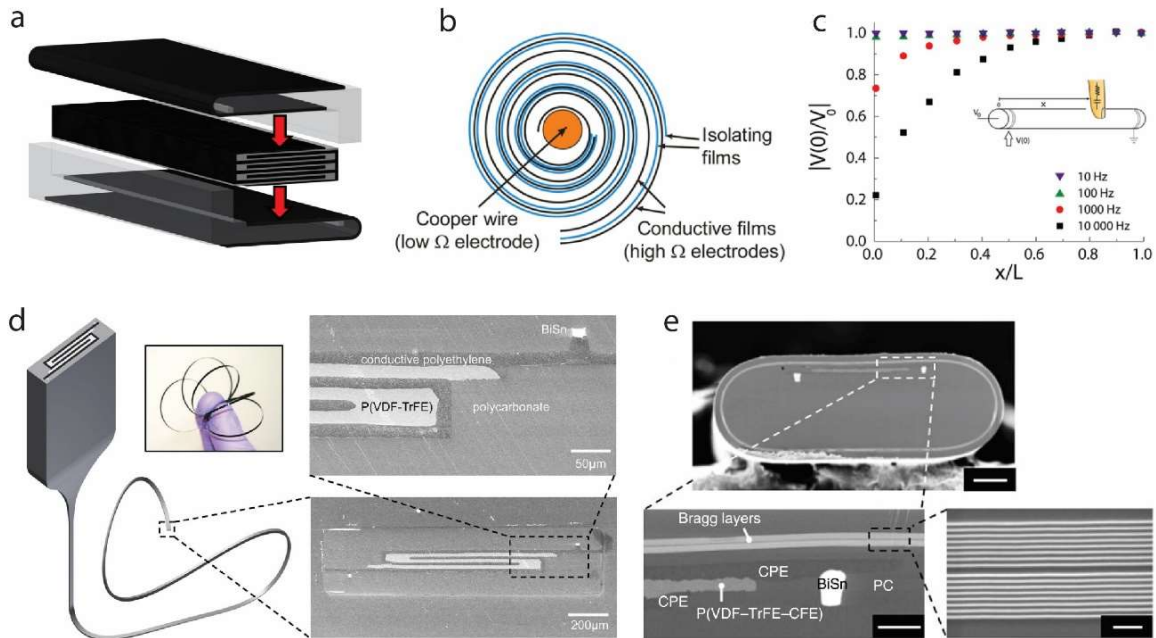


**Figure 1.4** (a) A multilayered structure of interdigitated CPE layers separated by a PVDF film for an enhanced capacitance.<sup>41</sup> (b) Schematic of a capacitor fiber that features a Swiss roll like structure with two conductive and two isolating films.<sup>42</sup> (c) Measured voltage at the extremity of the fiber in (b) opposite to the fiber's grounded end for detection of touch.<sup>42</sup> (d) A piezoelectric fiber for acoustic emission and reception.<sup>44</sup> (e) A fiber with an

electrostrictive domain consisting of P(VDF–TrFE–CFE) and CPE electrodes for electromechanical actuation and modulation of integrated Fabry–Pérot cavity.<sup>46</sup>

Beyond acoustic transduction, a poly(vinylidene fluoride) derivative, P(VDF–TrFE–CFE), was employed to establish electromechanical actuation in fibers.<sup>46</sup> By sandwiching such an electrostrictive layer between polymer composite electrodes and placing the construct off-axis, the resulting fiber could be triggered to bend through electrical stimulation (Figure 1.4e). By applying 200 V DC, a fiber with a 3.5 cm free standing length could be deflected transversely up to 80  $\mu\text{m}$ . Applications of such shape-changing fibers are foreseeable in various domains, such as in-body navigation in the form of a steerable catheter.

## 1.4 Soft multi-material electronic fibers

There has been growing interest in the development of stretchable or soft multi-material fibers, which is heavily motivated by the exciting opportunities of electronics that are able to conform to the human skin, biological tissue, soft robotics and textiles. Multi-material electronic fibers that can maintain their complex functionalities while bearing large deformations hold important promises in the fields of electronic skins, artificial muscles, implantable medical devices and smart textiles. Thus far however, while thin fibers can be flexible, the elastic deformation of the thermally drawn fibers has been restricted to a few percent, which is a typical value for rigid thermoplastic materials.

A recent improvement in the mechanical performance of multi-material fibers consists of the post-drawing dip coating processing of cyclic olefin copolymer elastomer (COCE) fibers for the production of flexible and stretchable spinal cord probes (Figure 1.5a).<sup>47</sup> The study suggested that such hybrid probes could maintain both low optical transmission losses in the visible light range and low impedance, suitable for extracellular recording even under strain levels that exceed those occurring in mammalian spinal cords. Despite the improved mechanical properties, some restrictions still remained to be alleviated. The polymer COCE has a higher value of Young's modulus (34 MPa), which is still far beyond the softness of our body tissues. Moreover, the low melting temperature of COCE (84 °C) is quite low, making it difficult to be co-processed with the commonly used polymers ( $T_g$  higher than 100 °C) for the creation of fibers with complex architectures, or function as the cladding material of multi-material fibers. Lastly, the fabrication procedures can be simplified if the elastomeric cladding can be directly drawn instead of relying on extra dip coating.



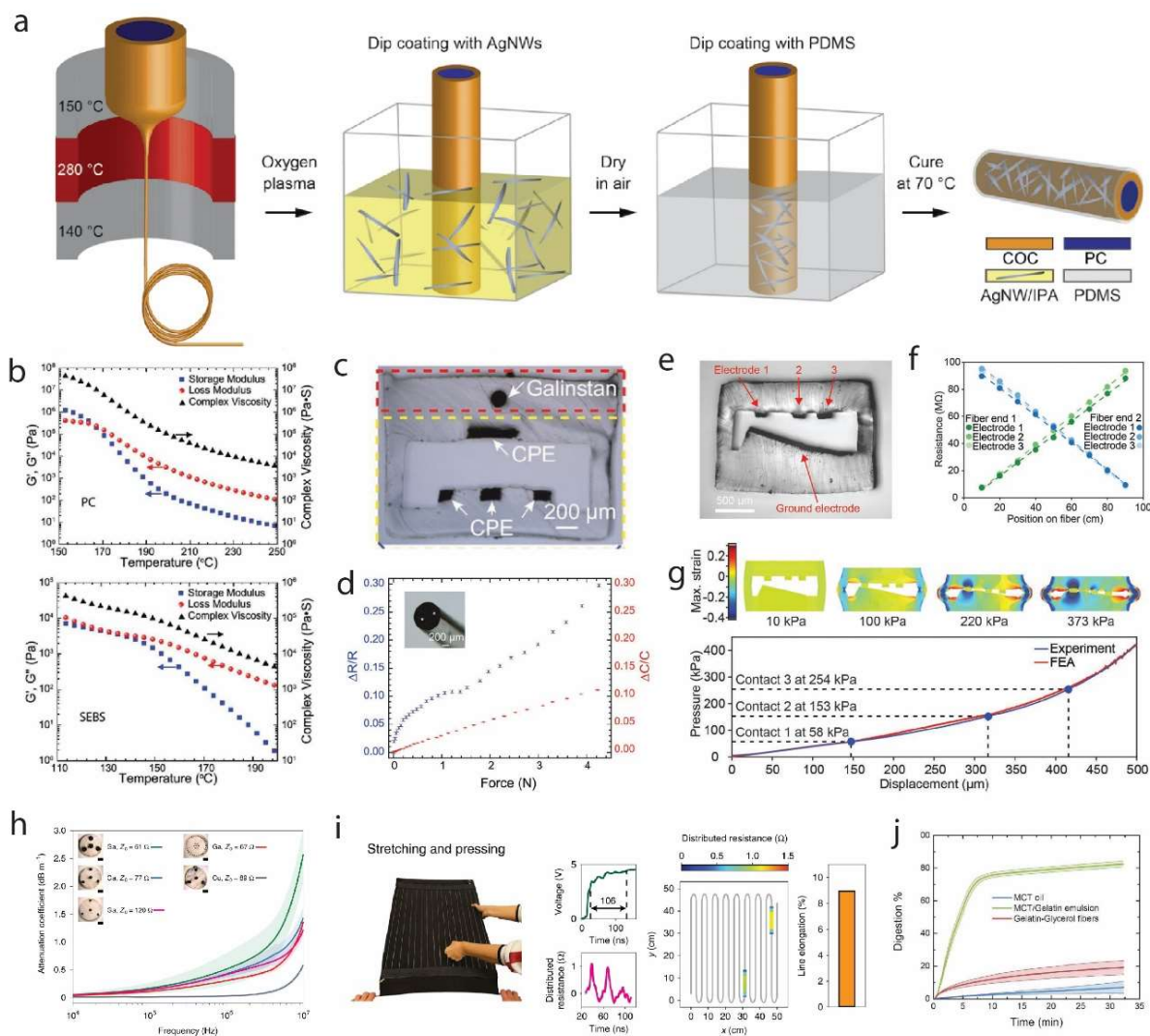


**Figure 1.5** (a) Schematic showing the fabrication of a flexible and soft fiber probe processed using a dip coating method after drawing.<sup>47</sup> (b) Rheological properties including storage moduli, loss moduli and complex viscosities of PC and SEBS.<sup>48</sup> (c) A deformable thermoplastic elastomer fiber with a liquid metal channel and four composite electrodes for the quantification and localization of pressures and the discrimination between compressive and shear loading.<sup>48</sup> (d) A stretchable fiber with two liquid metal channels for the sensing of large strains through changes in resistance or capacitance.<sup>48</sup> (e) A compressible fiber with three small conductive composite electrodes arranged opposite to another large inclined composite sheet in a SEBS support.<sup>49</sup> (f) Resistance of the three electrode pairs as a function of the position of the pressure on the fiber. The resistance measurement can be performed at either fiber end.<sup>49</sup> (g) Finite element analysis and experiments showing the fiber's capability to quantify the applied pressures. The increased level of pressure induces the progressive collapse of the fiber

structure, which is divided into distinct regimes separated by the consecutive contact events of the electrodes.<sup>49</sup> (h) Frequency-dependent attenuation coefficient of transmission lines with different conductor materials, structure type and characteristic impedance  $Z_0$ .<sup>50</sup> (i) A 10-m-long triangular liquid metal transmission line is integrated on a stretchable fabric for the simultaneous discrimination and quantification of two modes of deformation: stretching and pressing.<sup>50</sup> (j) Lipid release study of multi-material gelatin-glycerol fibers containing medium chain triglyceride oil.<sup>51</sup>

Throughout the development course of multi-material thermal drawing, we can conclude that the processing of soft and stretchable fibers remained a long-term challenge due to the poor understanding of fluid dynamics and rheological properties of materials at play during drawing. Nevertheless, Qu et al. recently performed rheological and microstructural analysis on common thermoplastic materials and some thermoplastic elastomers, with the aim of discovering super-elastic materials that are compatible with thermal drawing and thus fabricating highly stretchable functional fibers.<sup>48</sup> It was discovered that the thermal flow in the viscous regime at high viscosities of a drawing compatible material can be defined at a temperature window where the loss modulus decreases slowly with temperature, crossing over elastic modulus that rapidly decreases. Figure 1.5b shows the rheological properties of polycarbonate (PC) and poly(styrene-*b*-(ethylene-co-butylene)-*b*-styrene) (SEBS), both of which satisfy the above criterion and can be successfully drawn into fibers. This study allowed the identification of a more in-depth requirement for evaluating the suitability of potential materials for drawing.

The vast deformation that the SEBS elastomer can elastically undergo was exploited to develop fibers with fully enclosed composite electrodes, which enabled the discrimination of compressive and shear loading (Figure 1.5c). In this work, the integration of dynamically responsive liquid metal channels was also explored to extend the functionality of fiber-based devices, such as the quantification of transverse pressure magnitude as well as elongation strain (Figure 1.5d). Complex applications of these fibers in smart textiles and robotics were also demonstrated. Another interesting example exploiting this advance involves the arrangement of polymer composite electrodes in a novel asymmetric architecture within a SEBS cladding (Figure 1.5e).<sup>49</sup> With simple resistance measurement, kPa-scale pressures applied on the fibers can be reliably quantified and located (Figure 1.5f, g). This enabled the functionalization of large surface areas without the need of typically employed sensor arrays, thus drastically reducing the number of failure-susceptible electrical connections.



Moreover, electrical time-domain reflectometry can be adapted to the field of soft and stretchable electronics via the incorporation of thermoplastic elastomers and liquid metal conductors.<sup>50</sup> With the design of fiber architectures, the radio-frequency characteristics in these soft transmission lines, including impedance, shielding and losses can be well tuned (Figure 1.5h). We investigated both experimentally and theoretically the reflected waves in the time domain triggered by multimodal deformations of the dynamically responsive liquid metal conductors themselves, as opposed to only the dielectric between them. This mechanism enables multiplexed pressure measurements at a sensitivity that is improved by a factor of 200 when compared to thermally drawn transmission lines based on conventional hard metals. Using a 1-m-long line acting as a distributed probe, the authors demonstrated quantitative assessment of multiple pressure points with a force resolution of 0.2 N and a spatial resolution of <6 cm, as well as an elongation with a strain resolution of 0.25%. In addition, an electronic textile was built by integrating a soft transmission line in a large stretchable fabric (50 cm × 50 cm), as shown in Figure 1.5i, which exhibited higher functionality than existing systems that require hundreds of point sensors and electrical connections.

Guided by the abovementioned rheological criterion for the selection of thermal drawing compatible polymers, novel soft microstructured edible materials have also been successfully integrated into multi-material fibers. The material system consists of gelatin with plasticizers such as glycerol for the modulation of its rheological behaviors. This particular material was exploited to demonstrate the fabrication of edible fibers as encapsulating constructs for the controlled release of nutrients and digestion tailoring (Figure 1.5j).<sup>51</sup>

## 1.5 Objectives and outline of the thesis

The overall objective of this thesis is to propose innovative designs and novel functionalities for electronic multi-material fibers. More specifically, we have addressed three scientific and technological challenges:

- 1) Reconcile advanced microfluidics with the field of electronic fibers: for the first time, we designed, fabricated and characterized a capacitive device that can be used as an innovative microflow sensor.
- 2) Generating electric power from multi-material fibers. While many strategies have been investigated over the last decade or so, no thermally drawn fiber could demonstrate any power

generation. We designed, fabricated and demonstrated super-elastic liquid metal based triboelectric fibers and textiles with excellent performance both as sensors and energy harvesters, through the combination of surface microengineering and multielectrode design.

- 3) In the field of triboelectricity, a structure that can generate electricity upon stretching has rarely been demonstrated. In a third project, we designed and fabricated stretchable water-repellent multi-material triboelectric fibers that can not only generate electricity from different forms of mechanical stimulation, but also exhibit stable output performance under harsh conditions.

The outline of the thesis is described as follows:

Chapter 1: We first briefly introduce the research background of fiber electronics, followed by the discussion of their current fabrication strategies and the remaining challenges in this field. Afterwards, we summarize the advances, principle and distinctive features of the perform-based multi-material thermal drawing technique from the perspectives of materials, structures, manufacturing, functionalities and applications. Then, we present the recent scientific and technological breakthroughs in thermally drawn multi-material fiber electronics, especially their applications in the fields of neural science, microfluidics, sensing, smart textiles, energy harvesting and storage, as well as actuation. Depending on the main functional materials involved in the devices, we divide the content into three main sections: metals and polymer composites, semiconductors, and insulating materials. Finally, we describe in detail the recent exploration of integration of soft and stretchable materials to multi-material fibers: post-thermal drawing fabrication and direct multi-material drawing. In particular, we present the deeper understanding of rheological dynamics that govern viscosities, which expands both the choice and combination of materials that can be processed by drawing. In addition, several examples of soft and stretchable fiber electronic devices are demonstrated to give direct evidences showing the significant promise of this breakthrough.

Chapter 2: In this chapter, we demonstrate the design and thermal drawing fabrication of capillary-like microstructured multi-material fiber devices for microfluidic sensing. We do a short review of the use of fibers in microfluidics. Then we explain how we introduced a capacitive sensing system that consists of an encapsulated microchannel in a polymeric cladding, together with embedded electrodes within fiber configuration. We show the multifunctionalities of such fiber constructs towards the instant monitoring of the presence and amount of a fluid inside the channel, the precise sensing of the real-time flowrate over a very wide range, as well as the high accuracy detection of the static dielectric constant

of the fluid. As a capacitive device, the fiber exhibits a broad operative frequency range from 100 Hz up to 2 MHz, and is capable of sensing microflows with a wide flowrate range from 50 nL min<sup>-1</sup> to 10 mL min<sup>-1</sup>.

Chapter 3: In the last chapter, we demonstrated the promising application of capacitance on microfluidic sensing, we were further motivated to explore the role of capacitive behavior on energy harvesting. Fibers that harvest mechanical energy via the triboelectric effect are excellent candidates as power sources for wearable electronics and functional textiles. Thus far however, their fabrication remains complex, and exhibited performances are below the state-of-the-art of 2D planar configurations, making them impractical. In this chapter, we demonstrate the thermal drawing fabrication of a highly elastic microstructured triboelectric fibers with performance on par with state-of-the-art planar TENG devices. The fibers consist of a microstructured thermoplastic elastomeric cladding that surrounds one or several liquid metal electrodes. We show experimentally that such fibers are soft and exhibit high stretchability with a fracture strain as high as 560%. We also show that the fibers are robust and could maintain stable output performance even after 50,000 cyclic compression and long-term large deformation operations. The superior mechanical properties of such fibers enable their integration into large-area, elastic and high-performance machine-washable energy-harvesting textiles. In addition to highly efficient energy harvesting function, the microstructured surface and high deformability of the fibers also enable their self-powered sensitivity towards a variety of mechanical stimuli, such as finger bending or breathing.

Chapter 4: Different from the single-electrode triboelectric fibers shown in Chapter 3, in this part I discuss the fabrication and characterization of a newly designed soft and stretchable multi-material triboelectric fiber that functions in the contact-separation mode. The fiber features a large embedded gap between two tribosurfaces, with all the functional materials seamlessly encapsulated within a SEBS cladding. We show experimentally that SEBS is a typical hydrophobic material and its water vapor transmission rate is much lower than other common elastic materials such as PDMS, and is comparable with some common polymers for packaging. Such distinguished water repelling properties together with the superior elasticity enables the efficient and stable energy harvesting function of the final fiber device, even under large deformations and high humidity. A stretchable and conductive composite is meticulously selected as the main electrode material, which is intimately interfaced with an extra liquid metal channel to guarantee a good electrical conductivity along the fiber length. Electrical resistance

measurement together with SEM characterization and mechanical test of the composite concurrently suggest the relatively homogeneous distribution of the conductive filler – carbon nanotubes – in the polymeric matrix. In order to achieve optimal electrical performance, the triboelectric materials are carefully selected and micro-textures are patterned on their surface. Finally, with the objectives to find a sacrificial polymeric layer to reduce the thermal reflow during processing, surface/interfacial tensions of the targetted materials are evaluated by the combination of contact angle measurement and the OWRK model.

Chapter 5: Concentrating on the electrical and mechanical characterizations, here we investigate the potential of the produced self-encapsulated stretchable fibers as conductor-to-dielectric contact-mode TENG devices. We first combine FEA simulation and Gauss theorem analysis for an in-depth understanding of the working principal as well as a quantitative estimation of the effects of the fiber's dimensions on the output performance, which provide us a theoretical guidance on the structural design of the fibers. The electrical outputs of the resulting fibers are characterized and effects of the micro-textures on the triboelectric surfaces is confirmed. Thanks to the highly elastic and water-repellent SEBS cladding, the fibers exhibit high robustness and reliability toward long-term operations under repeated large deformations or several days' storage in water. In addition, the output current of the fibers is significantly dependent on the compressive pressure, which shows a linear increase at low pressures and reaches a saturation as the pressure is high enough to trigger the contact of two tribosurfaces. We then take advantage of FEA simulation to understand the kinetic deformations of the fiber system under compression and explore the effects of parametric modifications of the open channel's dimensions on the mechanical response of the fiber structures. It enables the precise prediction of the mechanical behavior of such fibers under compression and thus guides our customized designs for specific applications. Lastly, we will demonstrate the capability of the fiber for energy harvesting from its stretching deformation. The outcome of this work will extend the field of multi-material fibers to novel materials and complex architectures with innovative functionalities in energy harvesting and sensing.

Chapter 6: Conclusions

## Chapter 2 Microstructured multi-material fibers for microfluidic sensing

The majority of this chapter is adapted from a publication in *Advanced Materials Technology* that addresses the exploitation of fiber processing to the realm of microfluidics.<sup>52</sup> Integrated microfluidic systems are being increasingly exploited in a variety of fields such as the biochemical, clinical, and pharmaceutical sectors, due in large part to the recent advances of “Lab-on-chip” and other miniaturization strategies.<sup>53–56</sup> In particular, microflow sensors that are able to measure very low flowrates and perform quantitative analysis of fluids are becoming increasingly important components for precise process control and fluid monitoring. Applications include analytical chemistry, drug delivery, fuel meters, and blood flow monitoring.<sup>57–59</sup> To date, flow monitoring has relied on different operating principles including heat transfer, drag-force, or pressure-induced variations in electrical and optical parameters.<sup>55,60</sup> The most widely reported devices are thermal-based flow sensors, which rely on the heat transfer between a source and a detector separated by a moving fluid.<sup>61</sup> While these sensors can measure changing flowrates, they may suffer from various limitations such as the requirement of pure liquids as impurities can affect heat transfer and measurement accuracy,<sup>62</sup> or the need to heat the fluid, which is restricting for applications in biology and drug release. Micro thermal flow sensors are also vulnerable to thermal losses caused by other heat transfer pathways such as through substrates or electrical leads.<sup>61,63</sup> Moreover, as with other methods, it is quite challenging to detect very low flow rates, and devices are only good for the detection of flowrates within a narrow range.<sup>59</sup>

Capacitive-based sensors allow the circumvention of some of these limitations and constitute a powerful alternative flow-monitoring scheme for many applications.<sup>60</sup> Relying on the change of capacitance of a micro-channel as it is being filled by the sampled liquid, they allow for accurate measurements of a wide range of flow rates. They also enable the extraction of the dielectric constant of the fluid, which can provide information about its composition.<sup>64</sup> Thus far however, the fabrication of capacitive-based sensors has resulted in bulky systems, or has required complex lithography processes to integrate conducting electrodes alongside micro-channels.<sup>65,66</sup> Fiber processing techniques have recently emerged as an ideal platform to integrate a variety of materials alongside microstructured channels, for applications in neuroscience, optics or microfluidics. Capacitive-based microflow sensors that provide precise measurements with short response times and low power consumption entail similar

innovative fabrication strategies and designs to realize advanced sensing systems at high scalability, in compact forms, and low-cost disposability.

Herein, we demonstrate for the first time the fabrication of monolithic capacitive fiber-based devices for microflow sensing using the multi-material fiber drawing technology. The fiber device consists of an encapsulated micro-channel in a polymeric cladding, with embedded polymer composite electrodes that form a capacitive structure. The architectural design and scalable fabrication of the capacitive fiber will be firstly discussed, followed by the introduction of the proposed working principle as well as the characterization of the electrical impedance response of the fiber with respect to the applied frequency. Then we will present both the finite element analysis and experimental results showing the capability of the fiber for dynamic flowrate detection. Subsequently, we will discuss our exploration of another function of the fiber device – extraction of the dielectric constant of the flowing fluid. The capacitive responses toward the injection of different liquids will be also presented.

## 2.1 Fiber fabrication

Capacitive fibers are fabricated via a preform-to-fiber thermal drawing process, as shown schematically in Figure 2.1a-b. It begins with the construction of a multi-material macroscopic preform, via a series of simple machining techniques (Figure 2.1a). The fiber design consists of a hollow core surrounded by two integrated conducting polymer nano-composite electrodes and within a polymeric cladding. PC is selected as the encapsulating material, which enables the continuous deformation of the preform at a relatively high viscosity.<sup>48</sup> We chose CPE as the electrode because it is a material compatible with the thermal drawing process that can keep the desired shape to form the required semi-circular capacitor geometry.<sup>67</sup> A Bi<sub>58</sub>Sn<sub>42</sub> eutectic ( $T_m=139\text{ }^{\circ}\text{C}$ ) electrode is also added in contact to the CPE domain to enhance the conductivity along the fiber axis and thus improve the device response time. The CPE electrode is isolated from the channel by a PC layer to avoid deterioration, surface contact effects, and leakage currents. This PC layer is chosen to be thin enough to minimize the impact on the measurement as discussed below, while ensuring the integrity of the structure.

The assembly is subsequently fed into a draw tower and heated over its glass transition temperature. As the viscosity of the materials decreases by several orders of magnitude, the bottom region of the preform is then stretched (drawn) to yield a long, thin, and axially invariant fiber (Figure 2.1b-c). The fiber maintains the composition and cross-sectional architecture of the initial preform, but with reduced

transverse dimensions and an extended length. In Figure 2.1d we show an 80 m-long uniform fiber that was produced from a single draw, which corresponds to four thousand 2 cm-long functional capillaries. Note that industrial production results in tens-of-kilometers of fiber length, highlighting the scalability of this process. As a proof-of-concept, we characterize a fiber device with a diameter of the channel of around 400  $\mu\text{m}$ , which would fit syringe needles sizes and could be used as an integrated microflow meter for typical drug delivery monitoring systems.

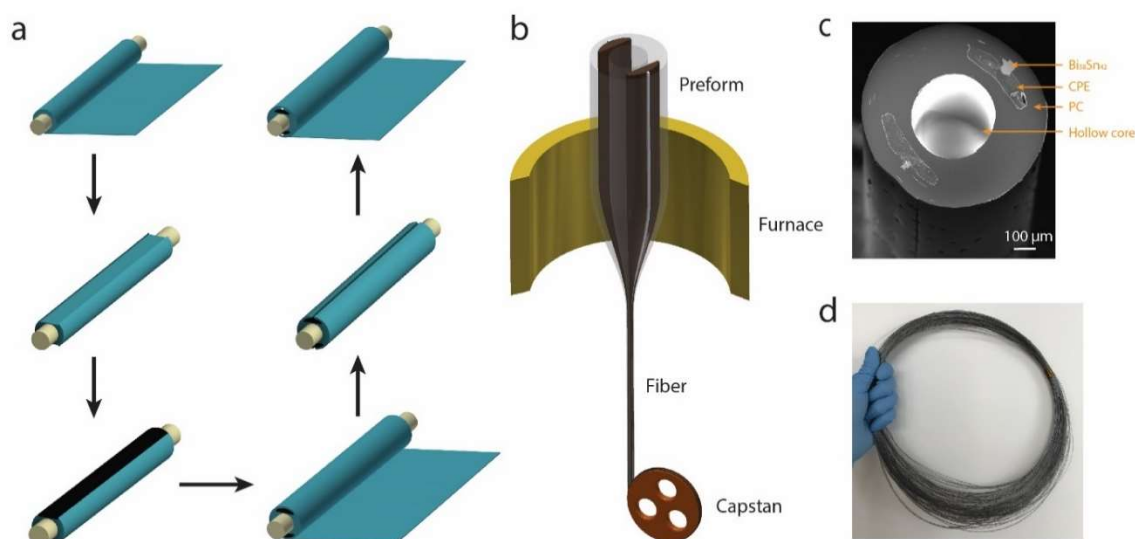


**Figure 2.1** Fabrication of capacitive fibers. (a-b) Schematic illustration of the preform fabrication process and the scalable thermal drawing technique. (c) SEM image showing the fiber cross-section. (d) Photograph of a continuously 80 m-long capacitive fiber, which was obtained from a single draw.

## 2.2 Capacitive behavior of the fiber device

The working principle of the fiber device is illustrated in Figure 2.2a. The hollow core acts as a microfluidic channel through which a liquid flows. The two electrodes along the channel, together with the in-between dielectric medium, form a capacitor. We can consider that the current leakage of the fiber capacitor is negligible, given the thickness of the PC layer. The equivalent circuit is then made of a resistance arising from the two electrodes and the involved electrical contacts, and three capacitance in series formed by the two PC layers between the two electrodes and the hollow channel, and the channel itself. As the fluid is flowing inside the channel, the dielectric constant changes, which results in a

measurable change of the equivalent capacitance, from which the dielectric constant and flow rate of the moving fluid can be extracted.

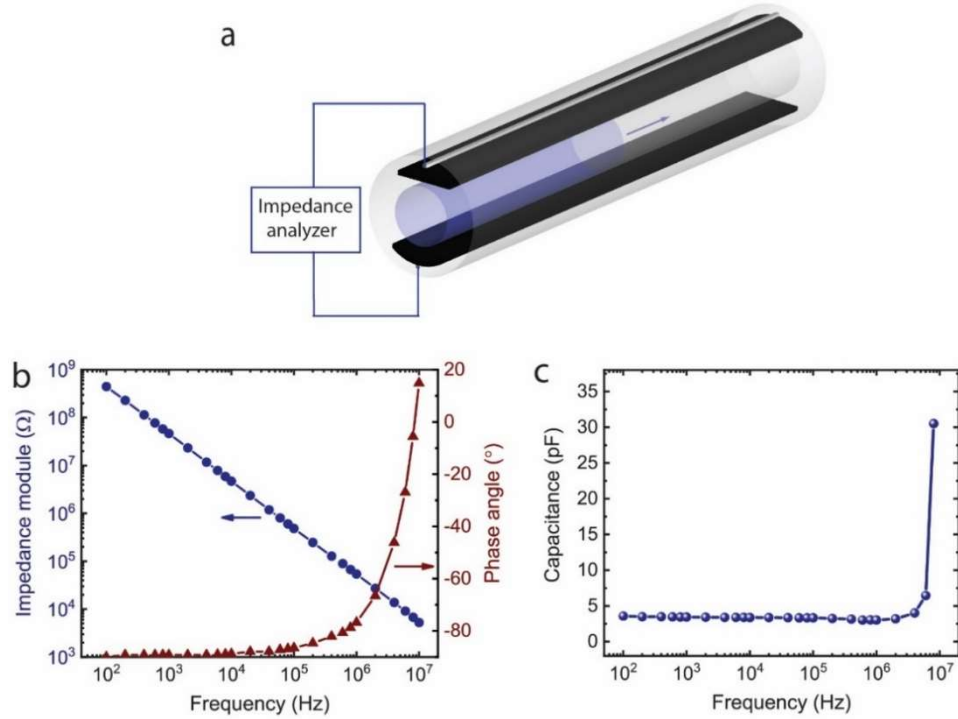


**Figure 2.2** Capacitive behavior of the fibers. (a) Schematic showing the hollow-core fiber in operation. The two metallic ribbons are connected to an impedance analyzer while a liquid (in light blue color) flows along the hollow micro-channel. (b) The inset shows its impedance module and phase spectra, exhibiting a definite capacitive behavior at a broad operative frequency range. (c) Calculated capacitance of the fiber under various frequencies, based upon an equivalent series circuit composed of ideal resistors and capacitors.

In order to gain more insight into the capacitive behavior of this fiber device, its electrical impedance response with respect to the frequency of the applied voltage was first characterized. Figure 2.2b presents the impedance module ( $|Z|$ ) and phase shift between voltage and current ( $\theta$ ) at various frequencies ( $f$ ) from 100 Hz to 10 MHz. It exhibits the expected behavior of an ideal capacitor up to around 2 MHz, beyond which the dissipation factor reaches 50% due to parasitic series resistance, inductive reactance, and current leakage. The series resistance extracted from this measurement is 6.7 k $\Omega$  and from the measured capacitance shown in Figure 2.2c, we can extract the resistor-capacitor (RC)



time constant of the circuit, which is 23 ns. The large range of operating frequencies enables the measurement of the capacitance of the fiber devices at a much higher bandwidth compared to typical time scales associated with microfluidics. In particular, it allows sampling of the fiber capacitance over time as the fluid is flowing, which in turn will inform on the flow rate, as we show below.

### 2.3 Discussion on the flowrate detection function

To understand and predict the change of capacitance of the fiber device as a liquid flows within its hollow channel, we modeled its behavior via finite element techniques using COMSOL. In particular, we modeled the electrical response of a 1 cm-long fiber as its hollow core was filled with water. The applied voltage between the two electrodes was 1 V. The obtained capacitance, and electric potential distributions were calculated using the electrostatics module, assuming no charge build-up at interfaces. As shown in Figure 2.3, the simulated capacitance exhibits a linear increase as the flow distance (the distance traveled by the fluid front) increases, which should enable the extraction of both the location of the fluid front and its dielectric constant.

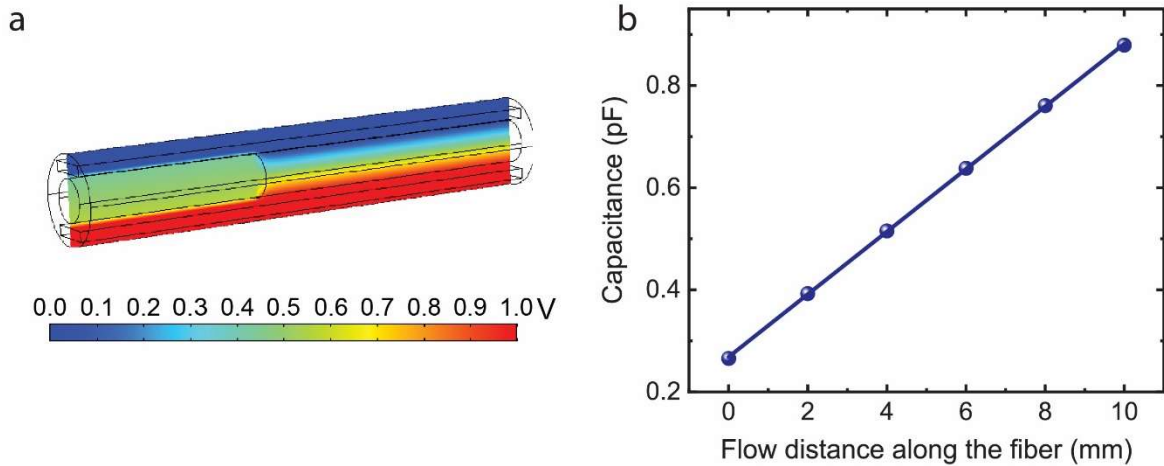


**Figure 2.3** Finite element analysis. (a) Simulation of the capacitive response of a 1 cm-long fiber to the flow of liquid in the channel. (b) Electric potential distribution of the fiber, where the green portion on the left indicates water filling the channel.

To confirm this analysis experimentally, we need to inject liquids into the fibers, which might cause short-circuit of the two electrodes and result in measurement errors once the liquids (especially the ones

with high electrical conductivities) reaches the fiber end and flow out. To avoid this, one method is to encapsulate the electrodes at the fiber end with epoxy resin while blowing air through the channel to prevent the blocking of the channel. Here we used another simpler strategy, which is to remove a small part of the two electrodes so that they cannot form an electrical circuit, as shown in Figure 2.4a. It is easier to operate and we just need to pay attention to the depth of milling to make sure that the PC wall of the channel still remains to some extent.

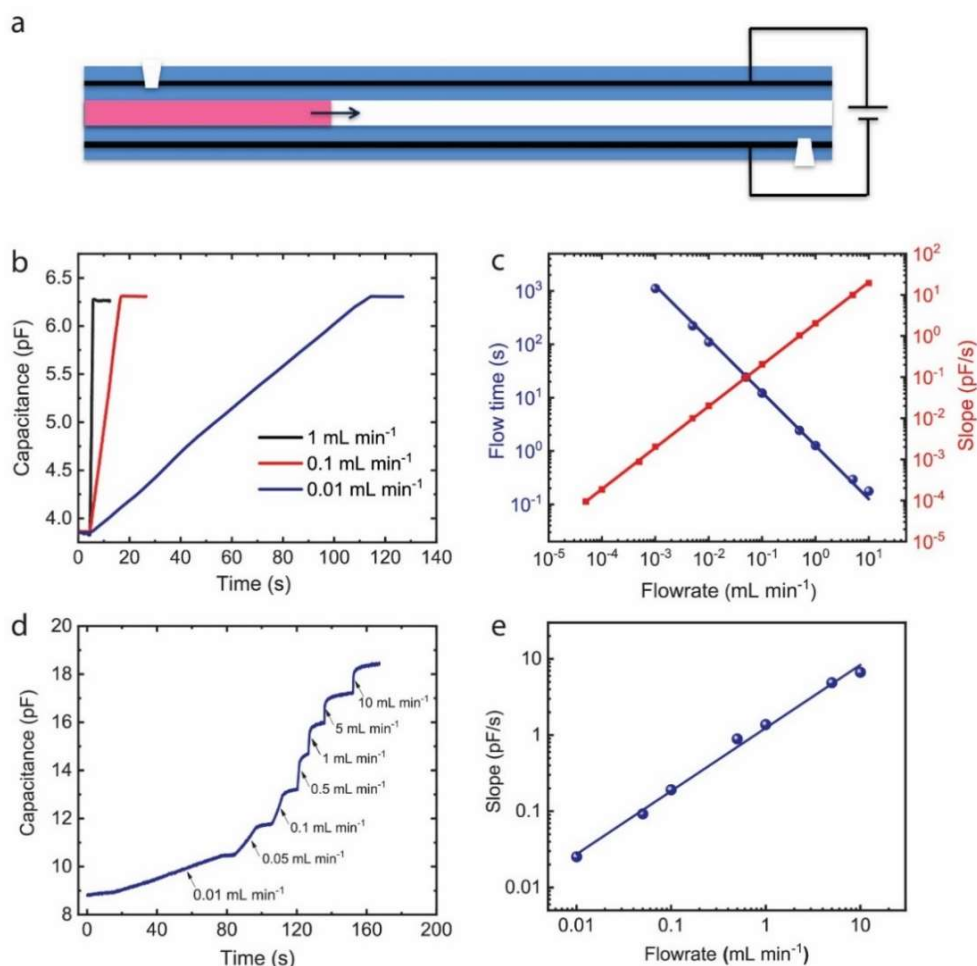


**Figure 2.4** Flowrate detection. (a) Two small parts of the fiber are removed to avoid potential short-circuit problem. (b) Experimental capacitive response of a  $\sim 4.5$  cm-long fiber to the injection of DI water with different flowrates of 0.01, 0.1, and 1  $\text{mL min}^{-1}$ . (c) Flowrate detection based upon the recording of flow time and the slope analysis of the capacitance vs. time curve. (d) Typical capacitive response of a fiber-integrated micro-flowmeter

to the flow with significantly varied flowrates ranging from 0.01 to 10 mL min<sup>-1</sup>. (e) The corresponding slope analysis.

Deionized water (DI water) was injected into a short fiber (4.5 cm in length) with different flowrates and its capacitance response was simultaneously recorded (Figure 2.4b). The initial capacitance of the fiber is stable at 3.9 pF, after which it increases linearly with the continuous injection of fluid. It stabilizes at 6.3 pF as the channel is fully filled with water. As the flowrate changes from 1 mL min<sup>-1</sup> to 0.1 mL min<sup>-1</sup> and further to 0.01 mL min<sup>-1</sup>, the capacitance response as a function of the flowing time varies accordingly. The final capacitance measured is however still the same as expected, from which the dielectric constant of the liquid can be extracted as we discuss below. The flowrate ( $v$ ) can also be deduced in real-time from the slope of capacitance change ( $k$ ) with time. The relationship between  $\log_{10}k$  and  $\log_{10}v$  in Figure 2.4c can be fitted with high accuracy:

$$\log_{10}k = 1.006\log_{10}v + 0.32, R^2 = 0.999 \quad (2.1)$$

which enables the precise extraction of the flow rate over an unusual wide range of rates from 50 nL min<sup>-1</sup> to 10 mL min<sup>-1</sup>, which is far beyond that of other reported micro-flowmeter devices.

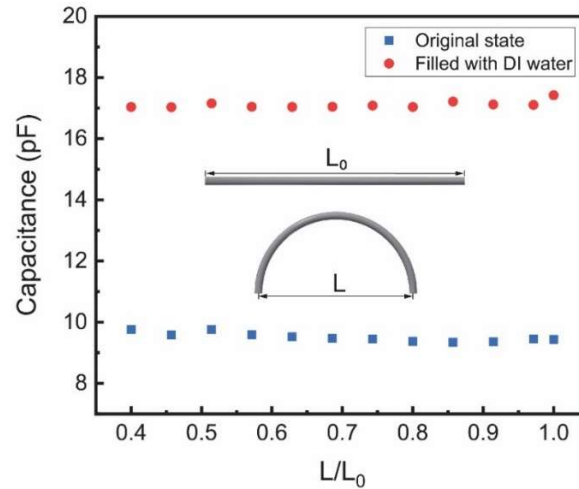


**Figure 2.5** Capacitance of a 17.5 cm long fiber under various bending conditions (different  $L/L_0$  values), where  $L_0$  is the length of the fiber, and  $L$  is the distance between its two ends under bending deformation (inset). The

blue squares indicate the capacitances when the micro-channel is empty, while the red circles represent the values as it is filled with DI water.

Figure 2.4d shows the capacitive response of a longer fiber with the successive flowrate change of DI water from  $10 \mu\text{L min}^{-1}$  to  $10 \text{ mL min}^{-1}$ . Upon each injection, the capacitance increases linearly with featured slopes and remains steady when the injection is suspended. The varied slope strongly depends on the applied flowrate with a well-defined proportional relationship, as revealed in Figure 2.4e. In addition, such fiber design shows high reliability on capacitive response, even under high bending deformations (Figure 2.5) in the case of long fiber designs. Note that the maximum flowrate could be further extended by increasing the accuracy and the data acquisition speed of the measurement system.

## 2.4 Discussion on the static dielectric constant detection function

The capacitive fiber-based capillary approach can also extract the dielectric constant of the flowing fluid. Dielectric constant is a physical property of a matter that indicates the coupling effect between a relatively weak electromagnetic field and the material itself. Since it is sensitive to interatomic and intermolecular attractions, the value of the dielectric constant of materials provides valuable information in areas such as drug and food safety analysis, diagnosis, material characterization, and medical instrumentation. For example, it is an important parameter for the evaluation of polarity characteristics of fluids, and a measurement of solvent's efficiency to separate the electrolytes into ions, especially with the established correlation between solubility and dielectric constant in pharmaceutical systems.<sup>68,69</sup> In particular, static permittivity, the permittivity measured in the low frequency range (normally 0.1-1.0 MHz), is a significant parameter in dielectric relaxation models (such as Debye relaxation) to study dielectric properties of materials with respect to frequency.

The fiber was characterized by recording its capacitance with the injection of different liquids (acetic acid, ethanol and DI water) at the same flowrate, as shown in Figure 2.6a. In order to avoid the influence of noise and electric double layers formed by the free ions in the liquids at lower frequencies,<sup>70</sup> and inductive reactance at higher frequencies, the characterization was done at 100 kHz. As expected, the three curves show distinct increasing trends and achieve different capacitance values when the channel of the fiber is fully filled, increasing their capacitance to 0.9, 1.9, and 2.4 pF for acetic acid, ethanol, and DI water, respectively. Intrinsically, the induced electric dipole moment in a dielectric creates an internal electric field that reduces the electric field within the dielectric itself. Therefore, as the static dielectric

constant of the material inside the channel varies from 1 to 80, the simulated electric field intensity of the channel reduces dramatically (Figure 2.6b).

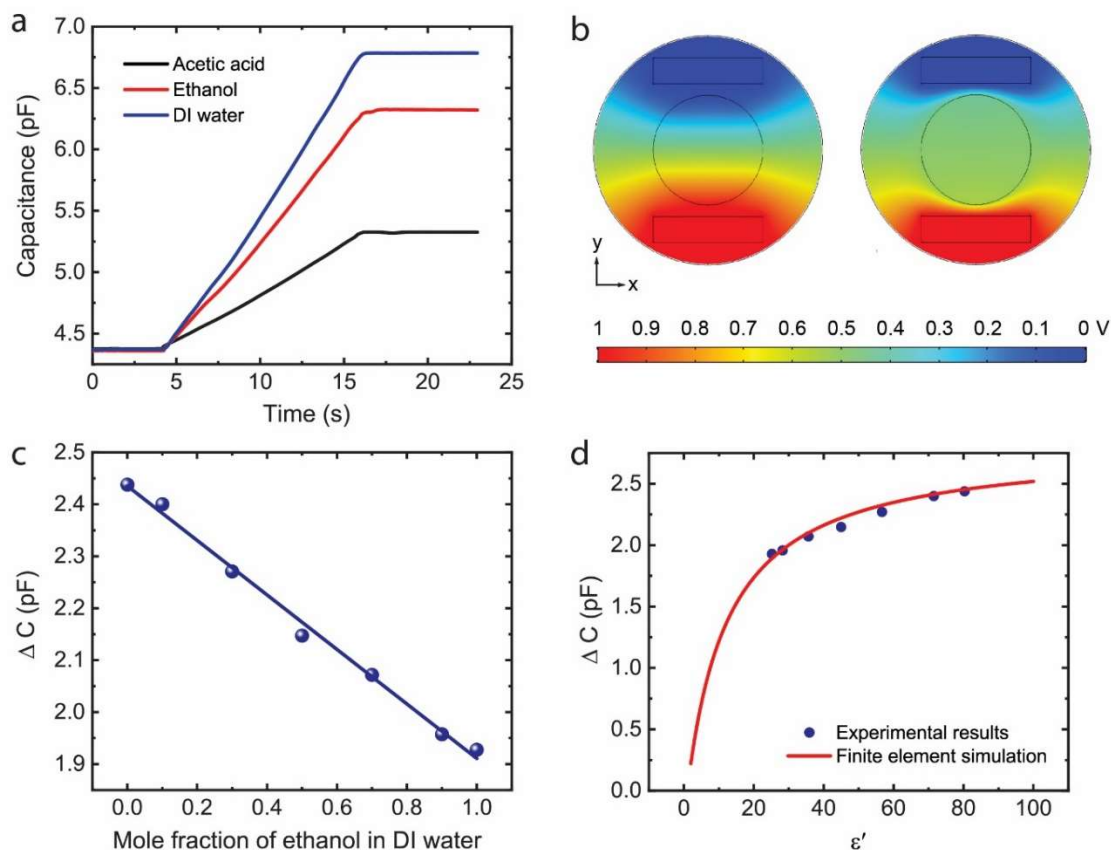


**Figure 2.6** Static dielectric constant detection. (a) Capacitive response of the fiber to the flow of different liquids (acetic acid, ethanol and DI water) with the same flowrate of  $0.1 \text{ mL min}^{-1}$ . (b) Finite element simulation of the electric potential distribution of the fiber. The material in the channel is assigned with different dielectric constants (left:  $\epsilon=1$ , right:  $\epsilon=80$ ). (c) Capacitance change of the fiber with varied mole fraction of ethanol in DI water. (d) Experimental and simulated capacitance change as a function of static dielectric constant.

To illustrate the ability of capacitive fibers to characterize flowing liquids, the fiber was characterized by recording its capacitive response with respect to ethanol/DI water mixture solutions with various concentrations. DI water has a high dielectric constant of 80.3 at this frequency and room temperature, whereas ethanol has a lower value of 25.2.<sup>71</sup> When mixed, the evaluation of the dielectric constant enables the determination of the mixing ratio of two liquids, which could be employed as a predictive

tool in a variety of fields including pharmaceutical and drug delivery. For example, the approximate dielectric constant is regarded as a basis for blending solvent mixtures for new drug formulations.<sup>69</sup> Taking advantage of the scalable fabrication technique together with the simple operation of the measurement, the capacitive fibers could be potentially used for the concentration detection of a mixed solution, or the monitoring of mixing process of two liquids.

Figure 2.6c shows that the capacitive response of the fiber decreases with the increasing mole fraction of ethanol in DI water. We assume a typical dielectric relationship given by:<sup>72</sup>

$$\ln \varepsilon_m = \varphi_1 \ln \varepsilon_1 + \varphi_2 \ln \varepsilon_2 \quad (2.2)$$

where  $\varepsilon_m$ ,  $\varepsilon_1$  and  $\varepsilon_2$  are the dielectric constants of the mixture, solvents 1 and 2 respectively, and  $\varphi_1$  and  $\varphi_2$  are the mole fractions of solvents 1 and 2. Combining this formula and the obtained experimental results, the relationship between the capacitive response of the fiber and the dielectric constant of the ethanol/DI water mixtures could be measured. The experimental results are shown in Figure 2.6d, together with the fitted curve realized by finite element simulation. The capacitive fiber can extract the mixture compositions of arbitrary liquids with high accuracy, regardless of the flow rate. While the polycarbonate layer used here can be well-adapted for most liquid sampling, it can be changed to another thermoplastic to avoid reaction with sampled liquid that could react with PC and impair the well functioning of the device. These results pave the way for a multi-functional capillary for flow rate and liquid analysis capabilities fabricated at the scale and cost traditionally associated with polymer fibers.

## 2.5 Methods

*Preform Fabrication and Fiber Thermal Drawing:* To fabricate the preform, a polycarbonate film (PC) (Goodfellow Cambridge Ltd) was first rolled around a Teflon film-wrapped ceramic rod (1 cm in diameter). After consolidation at 190 °C for 15 min, the obtained PC cylinder was milled to proper grooves for the introduction of two carbon-black-doped polyethylene (CPE) plates and Bi<sub>58</sub>Sn<sub>42</sub> ribbons (Indium Corporation of America) at prescribed positions. The CPE plates were fabricated by hot-pressing CPE films (Goodfellow Cambridge Ltd) at 120 °C for 15 min under a pressure of 0.5 bar using a Meyer Press (Maschinenfabrik Herbert Meyer GmbH APV-2525/16). Then another layer of PC was rolled outside the cylinder and consolidated, enabling the full encapsulation of the electrodes. The

ceramic rod was subsequently mechanically removed. The assembly was then thermally drawn in a typical three-zone draw tower, where the top, middle and bottom zones were heated to 120 °C, 265 °C, and 90 °C respectively. The preform was fed into the furnace at a speed of between 1 mm min<sup>-1</sup> and 1.5 mm min<sup>-1</sup>. The fiber drawing speed was varied between 0.1 m min<sup>-1</sup> and 2.4 m min<sup>-1</sup> to result in a controllable preform-to-fiber draw-down ratio from 10 to 40, and a 80 m-long fiber.

*Characterization:* The scanning electron microscope (SEM) image showing the cross-section of the fiber was taken with a Zeiss Merlin field emission SEM operating at 3.0 kV with a probe current of 120 pA. For the microfluidic characterization, the electrical contact of the fiber was realized by stripping away two small regions of PC cladding to expose the Bi<sub>58</sub>Sn<sub>42</sub> electrodes, and connecting to external copper wires with silver paint. Commercial syringe needles (400 µm in diameter) were inserted into the channel from two ends of the fiber, with epoxy resin for immobilization and sealing. The size of the fiber channel was designed to exactly match the outer diameter of the needles. This avoids the potential problem of the two electrodes being short-circuited by the injected conductive liquid (e.g. water). The injection of the targeted liquids was precisely controlled by a syringe pump (Cronus Sigma 1000). A HF2LI Lock-in Amplifier in connection with a HF2TA current amplifier (Zurich Instruments AG, Switzerland) was used for the impedance measurements. An AC voltage with the amplitude of 1 V was applied to the fiber for the test. The capacitances were calculated from the impedance results, based upon an equivalent series circuit composed of ideal resistors and capacitors. Note that the electrical measurements in this chapter were carried out on different fiber samples, and the results are very consistent, indicating the good repeatability and reproducibility.

## 2.6 Summary

In summary, we have demonstrated a simple and scalable platform for the fabrication of capillary-like multi-material fiber devices for microfluidic sensing using the preform-to-fiber technique. We introduced an encapsulated micro-channel in a polymeric cladding, together with embedded electrodes to form a monolithic capacitive system within the fiber configuration. We showed that the fiber construct is highly sensitive to the dielectric constant change of the micro-channel region, enabling not only the monitoring of the presence and travel distance of a fluid inside the channel, but also the measurement of the real-time flowrate and the static dielectric constant of the fluid. As a capacitive device, the fiber shows a broad operative frequency range from 100 Hz up to 2 MHz, and is capable of sensing liquids

with unusually wide flowrate range – from  $50 \text{ nL min}^{-1}$  to  $10 \text{ mL min}^{-1}$  – with high resolution. This measurement range can be tuned and extended in a straightforward manner by changing the geometric configuration of the preform to be drawn, and hence the resulting fiber. Note that the fabrication process is extremely simple and scalable, and can potentially yield tens-of-kilometers of functional fibers in a short time. For example, in the case of 1 cm-long fibers as plugs for syringes, this amounts to the fabrication of millions of such devices in a scalable, fast, low cost and continuous process. Such multi-functional fiber architecture is envisioned to have promising applications in the handling of complex microfluidics in a reliable, accurate, and cost-effective way. The miniature and flexible feature endows capacitive fibers with practical portability, and could contribute to the further development of “Lab-on-Fiber” devices.



## **Chapter 3 High-efficiency super-elastic liquid metal based triboelectric fibers and textiles**

The majority of this chapter is adapted from a publication in Nature Communications that addresses the difficult challenge of designing an efficient energy harvesting thermally drawn fiber.<sup>73</sup> Flexible electronics and particularly soft fibers and functional textiles are becoming an ideal platform in the areas of biomedical and health monitoring, implants and prosthesis, motion tracking, artificial intelligence and human-machine interaction.<sup>74–77</sup> A key challenge for their sustainable operation lies in the necessity of reliable and low-profile power systems. This is particularly important for implanted or textile-integrated systems, to untether them from current heavy and rigid batteries which require frequent charging or replacement.<sup>4,78,79</sup> One promising strategy to alleviate this challenge is the utilization of energy-harvesting technologies to sustainably generate electricity from surroundings. Examples include solar cells to capture energy from sunlight<sup>80</sup> and thermoelectric generators to produce electricity from temperature gradients.<sup>38,81</sup> Another promising strategy recently developed lies in triboelectric nanogenerators (TENGs) that combine contact-electrification and electrostatic induction effects to generate electricity from various mechanical stimuli, such as friction, vibration, rotation, and expanding/contracting motions.<sup>82–84</sup> Owing to a wide choice of materials and promising electrical outputs, various TENG configurations have been developed to adapt to different application scenarios.<sup>85,86</sup>

Thus far however, the performance and properties of TENG configurations within fibers and textiles remain limited and impractical. Fibers and fabrics obtained from coatings or printing remain complex to implement and exhibit performance that are well below state-of-the-art planar configurations.<sup>87,88</sup> Another strategy for smart textiles and wearable technologies involves integrating functionality directly at the fiber-level.<sup>31</sup> To be practical and efficient however, the fiber devices must host complex micrometre scale architectures, be soft and sustain various, sometimes large, deformation to generate a high voltage output over several cycles. The fibers must also be thin so they can deform under low forces, to ensure maximum energy harvesting output, as well as better sensing performance. Furthermore, the fabrication approach must be scalable and versatile enough to comply with different post-processing treatments including the integration into textiles.

To date, commonly-used materials such as polymer coatings<sup>89</sup> and metallic wires<sup>90</sup> are rigid and even when engineered in more deformable configurations such as wavy and coiled architectures,<sup>91</sup> the performance still remains limited. Other configurations such as thick, coaxial,<sup>92–94</sup> twisted,<sup>95</sup> and interlaced<sup>96</sup> cable-like TENGs that could incorporate multiple insulative and conductive materials have been proposed. To further enhance softness, liquid metal was also introduced within bulky silicon rubber constructs to make single-electrode TENGs.<sup>97</sup> While more stretchable, these devices remain of large feature size, and exhibit limited output performance, especially with respect to volume. Moreover, bulky systems are not well adapted for deformation sensing as they require higher forces to be activated. Their fabrication also involves several complicated steps that are typically restricted to laboratory scale, resulting in short length and large diameter cables that are not compatible with a variety of other applications such as implants, e-skin, textile weaving and knitting etc.<sup>90,93,97,98</sup> The production, at an industrially-relevant scalability, of thin and stretchable fiber- and textile-based TENGs with advanced architectures allowing for comparable performance with conventional planar devices, still presents great challenges from the perspectives of fiber materials, designs, and processing technologies.

Herein, we demonstrate the design and scalable fabrication of liquid-metal based microstructured stretchable TENG fibers and textiles with performance comparable to state-of-the-art planar configurations. First, we will discuss the identification of a thermoplastic elastomer that combines better triboelectric performance than commonly used materials, with rheological attributes compatible with the highly versatile fiber thermal drawing technique. Thanks to these findings, we then demonstrate the fabrication of potentially kilometer-long microstructured TENG fibers with advanced cross-sectional architectures integrating multiple liquid metal electrodes and a micrometer-scale surface texture. The important stress-strain curves of the resulting fibers will be presented to quantitatively evaluate their mechanical behaviours. The versatility of the thermal drawing process allows the exploration of complex fiber architectures for enhanced performance. A fiber design with engineered surface textures and multiple liquid metal electrodes will be presented. Then, the ability of such soft fibers to work as TENG devices will be evaluated through a series of electrical output characterizations triggered by periodic vertical compression. In particular, the endurance of the fiber devices toward repeated extreme deformations and extended environmental exposure will be characterized. Moreover, thermally drawn triboelectric fibers are thin and flexible enough to be seamlessly woven into an elastic energy-harvesting textiles. A 36 cm<sup>2</sup> textile will then be shown and its energy harvesting performance will be assessed and compared with the state-of-the-art 2D planar TENGs. Thanks to their specific design and high

deformability, these fibers can also form highly efficient and self-powered embedded deformation sensors capable of monitoring low-force stimuli. Applications including finger gesture sensing and breath monitoring will be shown and discussed.

### 3.1 Materials characterization and fiber fabrication

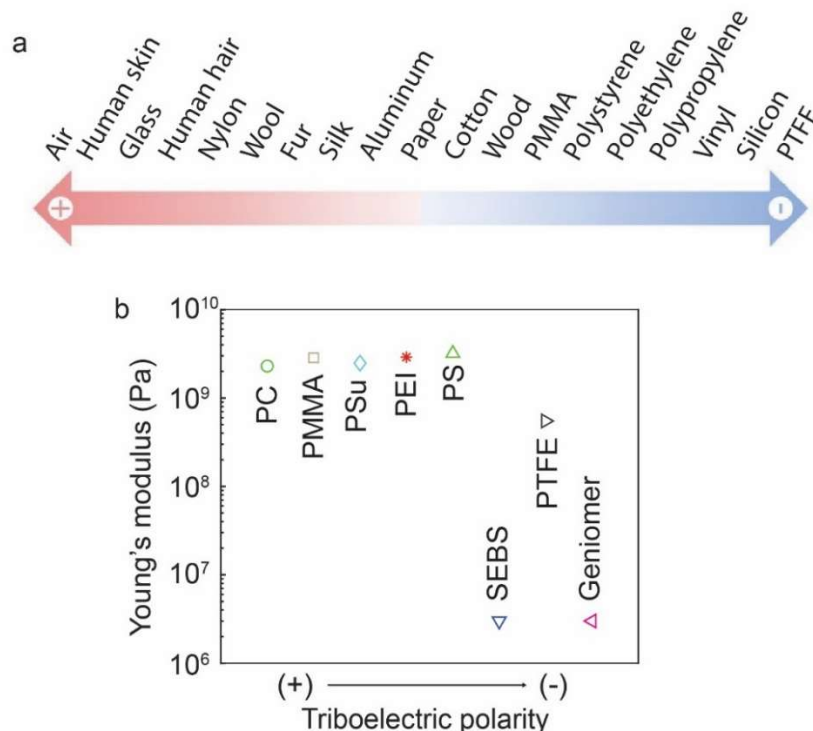


**Figure 3.1** (a) Triboelectric series of various materials. “+” / “-” indicate whether a material tends to be positively or negatively charged when triboelectrification occurs. (b) Comparison of Young’s modulus and relative triboelectric polarity of electrical insulating polymers that are compatible with the thermal drawing process. PTFE is also listed for a better comparison.

The working principle of a TENG system with a single electrode surrounded by an insulating cladding is based upon the combination of contact-electrification and electrostatic induction effects.<sup>99</sup> The triboelectric effect will occur between the microstructured fiber and surrounding materials. From a triboelectric potential table of various elements (Figure 3.1a),<sup>100,101</sup> we can observe that most commonly used materials in our everyday life tend to positively charge when contact-electrification takes place. To

ensure a high electrical output from soft fibers, we must select fiber materials that are compatible with the thermal drawing process, exhibit elastomer-like mechanical properties at room temperature, and possess a negative potential upon electrification.

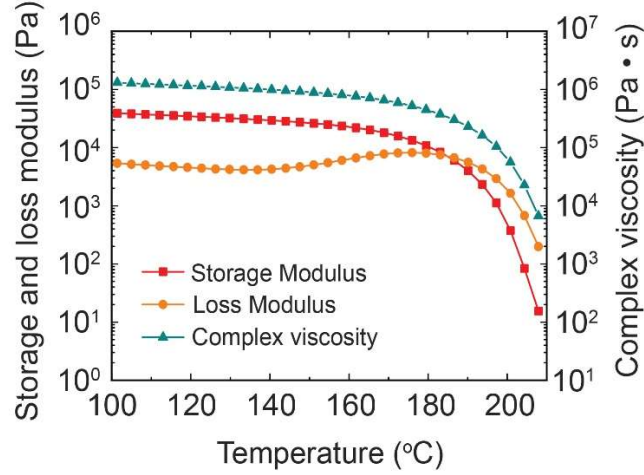


**Figure 3.2** Rheological properties of Geniomer: storage modulus  $G'$ , loss modulus  $G''$ , and complex viscosity.

In Figure 3.1b, we show the Young's modulus ( $E$ ) and relative triboelectric polarity of a few materials compatible with the thermal drawing process. We also show for reference the data for PTFE, a material with a strongly negative triboelectric polarity. Among these polymers, we selected Geniomer, a two-phase block copolymer made up of a soft polydimethylsiloxane phase and a hard aliphatic isocyanate phase. Geniomer is a thermoplastic elastomer with interesting mechanical deformation properties and especially a low Young's modulus ( $E = 3.4$  MPa), combined with a higher negative triboelectric polarity compared to PTFE. Under dynamic heating in the drawing process, the viscosity of the encapsulating material should be able to change slowly with temperature above its  $T_g$ , to ensure proper deformability at relatively high viscosity (typically between  $10^3$  and  $10^7$  Pa s). This condition allows the circumvention of thermal reflow and capillary breakup of involved materials, to produce microscopic fibers with well-preserved structures. In Figure 3.2 we show the complex shear viscosity together with the storage ( $G'$ ) and loss ( $G''$ ) moduli of Geniomer. It exhibits an elastic-solid-like behavior with a larger value of  $G''$  than  $G'$  and higher complex viscosity at lower temperature. On the contrary, it shows an absolutely fluid-like behavior at very high temperature, which normally results in polymer reflow and even structural collapse during drawing. According to the recent study by Qu et al.,<sup>48</sup> the optimal case of continuous

deformation at high viscosity lies in the transition from the elastic to viscous behavior scope, with the slowly changed  $G''$  intersecting the rapidly decreased  $G'$  (at around 185 °C here), suggesting the proper rheological properties of Geniomer to be compatible with the thermal drawing process.

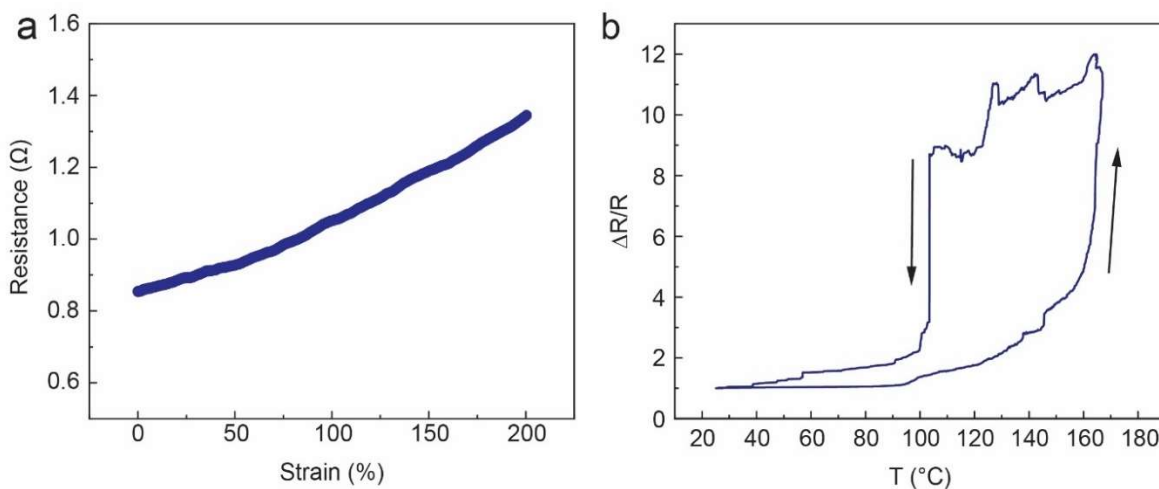


**Figure 3.3** (a) Resistance change versus strain of the liquid metal. (b) Resistance change of Galinstan as a function of temperature. The tested temperature ranges from 25 to 165 °C (the highest temperature that Geniomer experienced during drawing process is around 150 °C).

In addition to the cladding material, another key constituent for stretchable triboelectric fibers is a compatible electrode material with both high electrical conductivity and good stretchability. While conductive polymer composites formed by dispersing carbon fillers within a deformable polymer matrix can be a family of promising candidates, the interplay of thermal drawability, conductivity and stretchability of the composites brings a significant challenge. Thus, we oriented our choice towards a liquid metal alloy formed by gallium, indium, and tin (Ga62/In22/Sn16, named Galinstan), which exhibits not only high deformability but also a high electrical conductivity ( $3.46 \times 10^6 \text{ S m}^{-1}$ ) typical of metallic materials.<sup>102,103</sup> As shown in Figure 3.3a, the liquid metal can maintain its high electrical conductivity even under large strain.

After identifying the proper materials, in Figure 3.4a we schematically show the working principle of the thermal drawing process, which was initially developed to fabricate optical fibers. The process starts with the fabrication of a macroscopic version of the targeted fiber, termed preform, which is machined to the desired architecture (Figure 3.4b). Subsequently, the preform is locally heated above the glass

transition temperature of the cladding (here Geniomer) in a furnace and continuously pulled into a uniform and long fiber. The dimensions of the fibers, monitored in real-time by a laser system, are controllable by tuning the furnace temperature distribution, the preform feeding velocity, and the fiber drawing speed. With this approach, potentially hundreds of kilometers of fibers with the same structure as the preform can be reliably fabricated (Figure 3.4c).

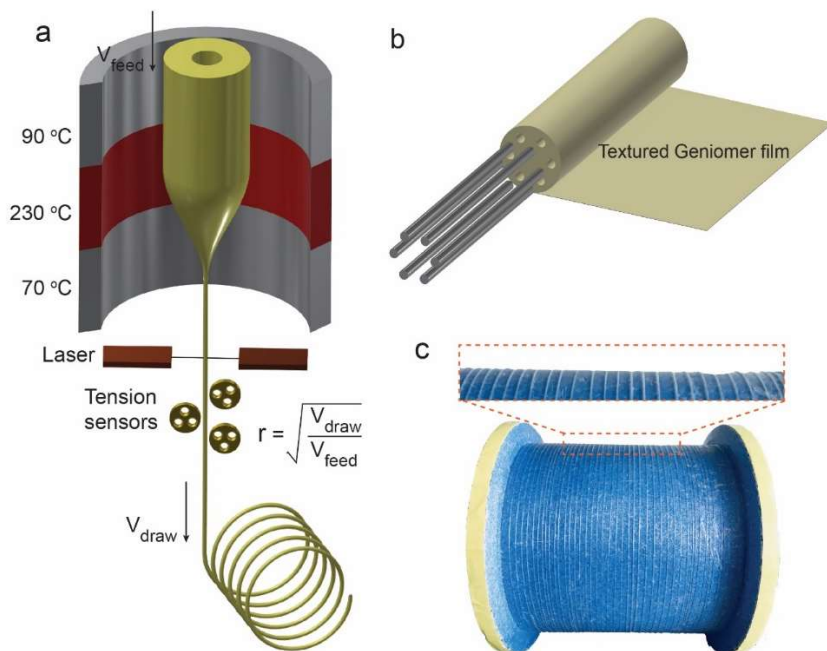


**Figure 3.4** (a) Schematic showing thermal drawing process for the production of long fibers. (b) Schematic of the preform fabrication. The preform integrates multiple channels and a microtextured surface. (c) A roll of 40 m of continuous fiber obtained from a single draw, demonstrating the scalability of drawing process.

Two strategies could be adopted for the integration of the liquid metal. For the sufficiently large channels and shorter fiber lengths (typically tens of meters), a straightforward strategy consists in infiltrating the metal post-drawing within the fiber microchannels. For small diameter channels, the liquid metal is integrated in the proper channels at the preform level, where it flows as a liquid within the polymer structure. Our experiments showed that the electrical resistance of the liquid metal increases with an elevated temperature (Figure 3.3b), but can recover to its original value after cooling down.

Figures 3.5a-b show the recorded stress-strain curves of a fiber without and with one liquid metal channel. The two fiber designs display almost identical elastomeric features with fracture strain reaching

up to  $599\pm73\%$  and  $557\pm54\%$ , and Young's modulus as low as  $3.4\pm0.6$  MPa and  $3.8\pm0.3$  MPa, respectively. A photograph showing a triboelectric fiber under high deformation is presented in Figure 3.5c. We also show that the triboelectric fibers are capable of tolerating other types of sophisticated deformations such as tight knots.

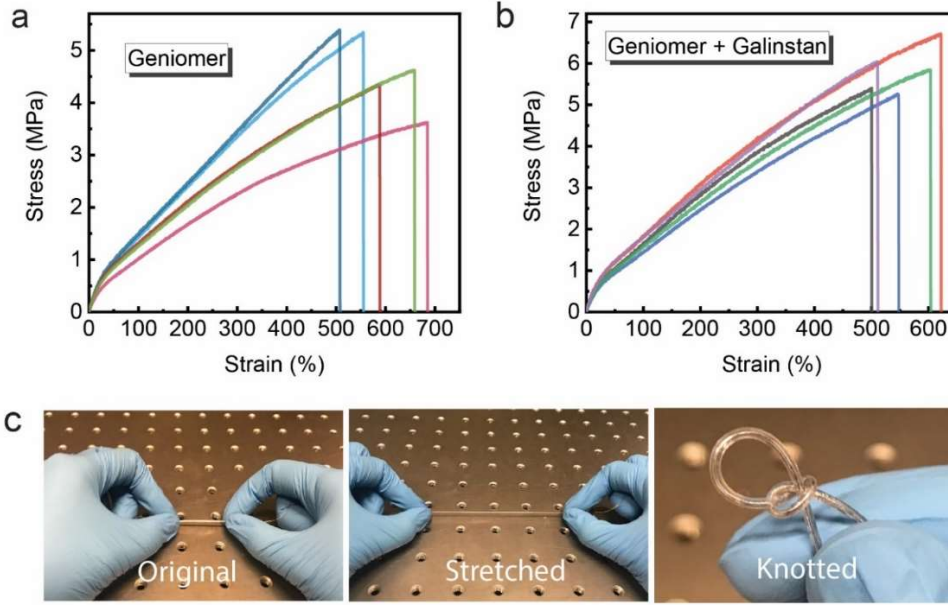


**Figure 3.5** (a, b) Stress-strain curves of fibers without (a) and with (b) integrated liquid metal electrodes. (c) Photographs showing flexibility and stretchability of triboelectric fibers.

In Figure 3.6a, we show the cross-sectional structure of a fiber with one integrated liquid metal electrode. Notably, even the sample is only millimeter long, it can still be easily bent by a tweezer, demonstrating the high flexibility and softness of the fiber assembly. The versatility of the thermal drawing process can be further exploited to realize more complex fiber architectures with enhanced performance. It has been demonstrated in particular that TENGs systems with rough surfaces can exhibit enhanced output.<sup>104</sup> In Figure 3.6c-d we show the cross-section of a fiber with a textured surface that exhibit enhanced performance compared to smooth fibers, as we show below. The design of the periodic square-shaped patterns on the preform was chosen because of the ease of fabrication and the ability of such structures to be maintained and avoid excessive reflow during thermal drawing.<sup>20,105</sup> In Figure 3.6b, we also demonstrate a fiber with four integrated liquid metal-based electrodes that can also exhibit enhanced performance, as we analyse below.

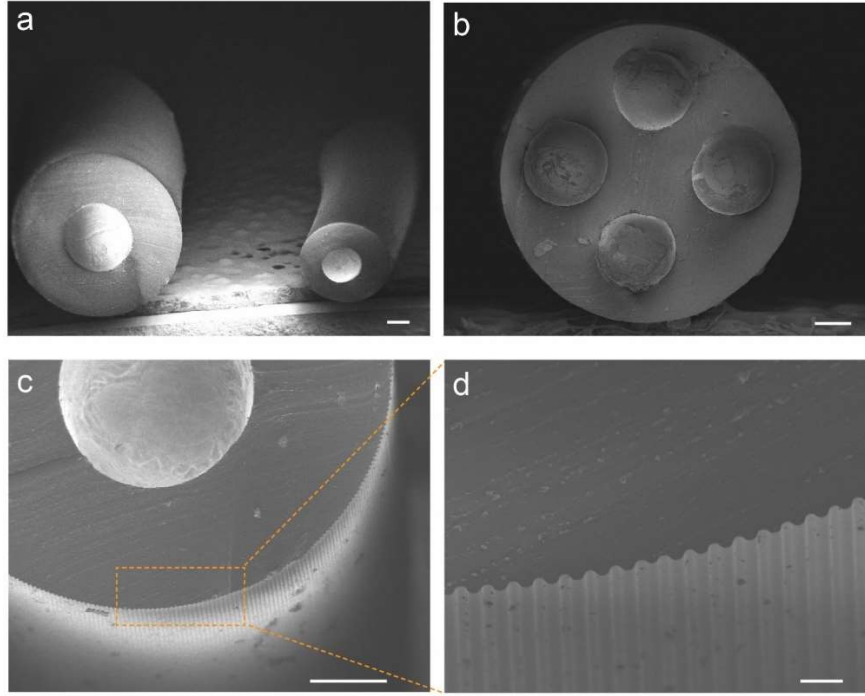


**Figure 3.6** (a) SEM image of a fiber with a single liquid metal electrode. Scale bar: 200  $\mu\text{m}$ . (b) SEM image showing a fiber with four liquid metal electrodes. Scale bar: 200  $\mu\text{m}$ . (c-d) SEM image of a fiber with micro-textured surface. Scale bar: 200  $\mu\text{m}$  (c) and 20  $\mu\text{m}$  (d).

### 3.2 Working mechanism

We next turn to investigate the ability of soft thermally drawn fibers to work as TENG devices. We start by characterizing a simple fiber configuration with one liquid metal within a Geniomer cladding, and will demonstrate the effect of adding more complex features such as a textured surface or multiple channels towards the end of the manuscript. In Figure 3.7, we schematically show the working principle of soft fibers triggered by repeated contact-separation movements with a PMMA sheet. It is assumed that, in the original state (before mechanical excitation), there is no electric charges on the fiber and PMMA surfaces, and the liquid metal electrode is connected to the ground. As an external force is applied to the PMMA sheet, it is brought into contact with the fiber surface, resulting in positive charges on the surface of the PMMA sheet and negative charges on the fiber surface respectively. As the PMMA sheet moves back away from the fiber, positive charges are removed from the surrounding of the metallic electrode which is felt as a change in the electrostatic field. Similarly, when the charged PMMA sheet



comes back into contact, an inverse field change is induced. An alternating current flowing from the liquid metal into the ground is hence generated at each cycle. Within a certain range, the amount of transferred charge increases with the increasing distance between the PMMA and the Geniomer ( $d_0$ ). When this distance remains the same, increasing the deformation of the fiber ( $d_1$ ) also results in increased amount of transferred charge. This is because the increased deformation can lead to an increased contact area between the fiber and PMMA, and thus a higher output. Therefore, soft materials are expected to generate higher electrical outputs than hard materials for our design. Similarly, taking into account the mechanical deformation of the fiber, the same process also takes place at the interface between the fiber and the bottom PMMA, although with less inductive electrons flow.

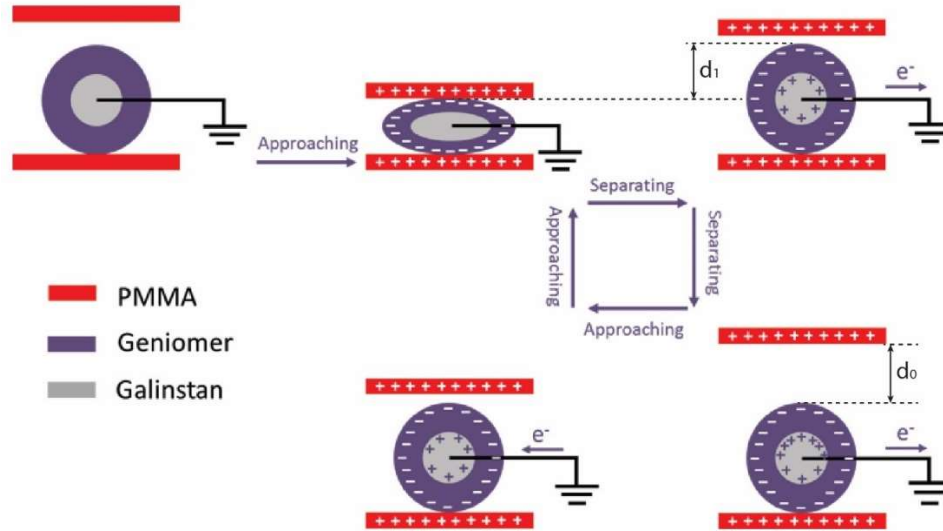


**Figure 3.7** Charge distribution of a TENG fiber under short-circuit conditions.

To understand the electricity generating process more quantitatively, the electric potential distribution of the system was simulated via finite element analysis using COMSOL. The 3D model was established based upon the real structure and dimensions of the fiber, while material properties were assigned in the software. We assumed that the whole fiber structure was exposed to air, and the potential at infinity was set to zero. We also assumed that the generated triboelectric charges are uniformly distributed on the PMMA and Geniomer surfaces, and the decay of triboelectric charges was neglected due to the fact that insulators can maintain the charges for a long time. The two tribo-charged surfaces are assigned with charge density of  $\pm 10 \mu\text{C m}^{-2}$ , respectively. The electric potential was calculated using the electrostatics

module, assuming that the surface charges can be kept on the surfaces for an extended time due to their insulative nature. Note that the assigned amount of charge density here only influences the absolute value of the calculated electrical potential, while the changing trend of the calculated results remain the same. Figure 3.8 shows the cross-sectional view of the model with simulated electrical potential distribution when the PMMA sheet is released and moving further away with varied distance. It is observed that with the movement of the PMMA sheet, the tribo-charges are separated and induce a significant change to the electrostatic field, consistent with the proposed mechanism in Figure 3.7.

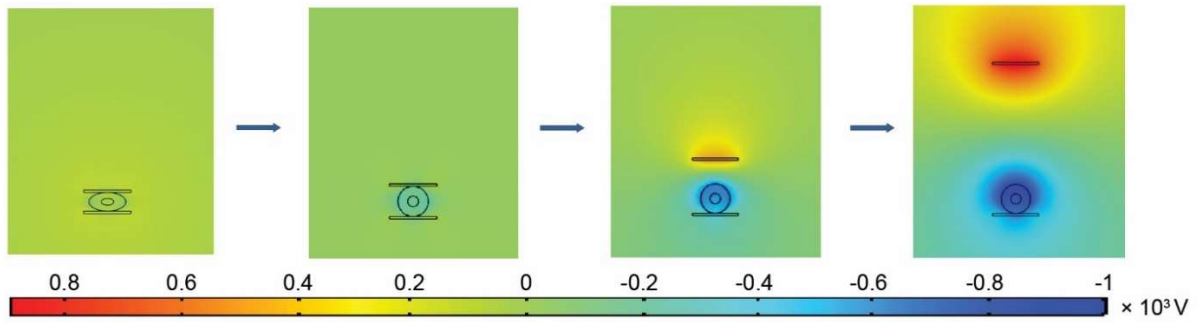


**Figure 3.8** Finite element simulation of the potential distribution of a fiber with a single liquid metal electrode under open-circuit condition.

### 3.3 Electrical output performance of triboelectric fibers

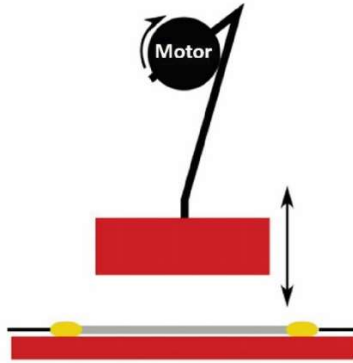


**Figure 3.9** Schematic showing the custom fiber compression setup. The length and width of upper PMMA sheet are 30 mm and 14 mm respectively, while the length and diameter of the tested fiber are 40 mm and 0.93 mm respectively. The maximum displacement distance of the PMMA sheet is 16 mm.

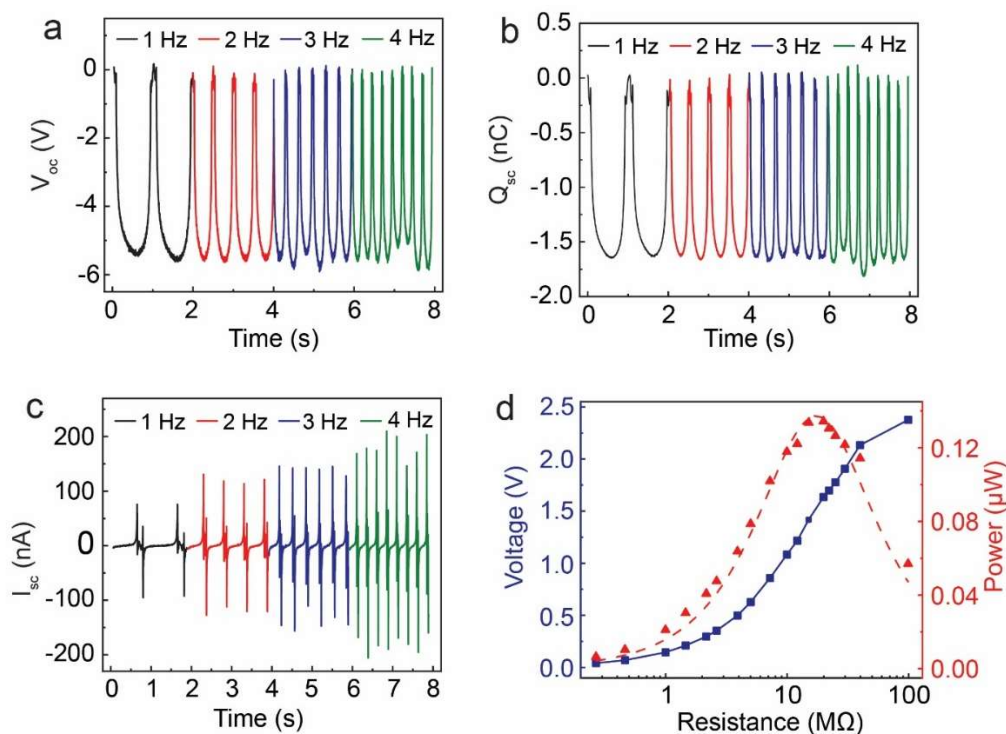


**Figure 3.10** Typical electrical output signals by tapping a short fiber. (a)  $V_{oc}$  (b)  $Q_{sc}$  (c)  $I_{sc}$  at various frequencies (effective contact length: 3 cm). (d) Dependence of the output voltage and peak instantaneous power on the loaded resistors.

To quantitatively assess the fibers' energy harvesting performance, we characterized their electrical outputs triggered by periodic vertical compression of a PMMA sheet, driven by a DC motor shown in Figure 3.9. In Figures 3.10a-c, we show typical outputs of a short fiber (contact length: 3 cm) under various frequencies. While there is no obvious change for  $V_{oc}$  ( $\sim 5.5$  V,  $269.9$  V/cm<sup>3</sup>) and  $Q_{sc}$  ( $\sim 1.6$  nC,  $78.5$  nC/cm<sup>3</sup>), the peak value of short-circuit current ( $I_{sc}$ ) reveals an increasing trend with the frequency, from  $\sim 90$  nA ( $4.4$   $\mu$ A/cm<sup>3</sup>) at 1 Hz to  $\sim 180$  nA ( $8.8$   $\mu$ A/cm<sup>3</sup>) at 4 Hz. This is ascribed to the enhanced flow rate of charges induced by higher deformation rates of the fiber at higher frequencies.<sup>106</sup> Compared with other previously reported triboelectric fiber constructs (Table 3.1), thermally drawn fibers with advanced cross-sectional architectures represent a significant improvement in terms not only of fabrication process and textile integration, but also in terms of output performance.

**Table 3.1** Comparison of the electrical output performance of the triboelectric fiber with other reported fibers.

Fiber length, diameter	Electrode materials	Triboelectric surfaces	Electrical output	Electrical output per volume	Trigger conditions	Stretchability	Reference
3 cm, 0.93 mm	Liquid metal	Geniomer//PMM A	5.5 V 180 nA (4 Hz) 1.6 nC	269.9 V/cm <sup>3</sup> 8.8 $\mu$ A/cm <sup>3</sup> 78.5 nC/cm <sup>3</sup>	Compression 2 N, 1.6 cm	557%	This work
1.5 cm, 1.8 mm	Stainless steel	PDMS//unknown external substrate	4 V 0.7 $\mu$ A (2 Hz) 1.25 nC	104.8 V/cm <sup>3</sup> 18.3 $\mu$ A/cm <sup>3</sup> 32.7 nC/cm <sup>3</sup>	Compression 2.5 cm	« not given »	Advanced Materials 29, 1702648 (2017) <sup>90</sup>
2 cm, 6 mm	Stainless steel	Silicone//acrylic	18 V 0.3 $\mu$ A (3 Hz) 6 nC	31.8 V/cm <sup>3</sup> 0.5 $\mu$ A/cm <sup>3</sup> 10.6 nC/cm <sup>3</sup>	Compression 4 cm	« not given »	ACS Nano 11, 9490–9499 (2017) <sup>93</sup>
10 cm, 2 mm	Carbon fiber	Silicone//skin	42.9 V 0.51 $\mu$ A (2.5 Hz)	136.6 V/cm <sup>3</sup> 1.6 $\mu$ A/cm <sup>3</sup>	« not given »	« not given »	ACS Applied Materials and Interfaces 10, 42356–42362 (2018) <sup>107</sup>
11 cm, 2.8 mm	Metal wire, Ag NW	Nylon/silicone	4.16 V	6.1 V/cm <sup>3</sup>	Stretch 68%	300%	Nano Energy 39, 673–683 (2017) <sup>108</sup>
30 cm, 1.8 mm	Helical stainless steel	Silicone//stainless steel	4.2 V	5.5 V/cm <sup>3</sup>	Stretch 100%	200%	Nature Communications 10, 868 (2019) <sup>109</sup>
5 cm, ~2.5 mm	Ag-coated nylon fiber, CNT sheets	Ag-coated Nylon yarn//PVDF-TrFE	24 mV 8 nA (10 Hz) 10 pC	0.098 V/cm <sup>3</sup> 0.03 $\mu$ A/cm <sup>3</sup> 0.04 nC/cm <sup>3</sup>	Stretch 50%	50%	Scientific Reports 6, 35153 (2016) <sup>110</sup>
4 cm, 1.6 mm	Ag NW	PTFE//PDMS-Ag NW	10 nA (2 Hz)	0.12 $\mu$ A/cm <sup>3</sup>	Compression 0.16 N	50%	Nano Energy 41, 511–518 (2017) <sup>111</sup>
10 cm, 4 mm	CNT, coiled Cu wire	Silicone//Cu	140 V 75 nA/cm (2 Hz) 5 nC/cm	111.4 V/cm <sup>3</sup> 0.6 $\mu$ A/cm <sup>3</sup> 39.8 nC/cm <sup>3</sup>	Stretch 50%	100%	Advanced Functional Materials 27, 1604378 (2017) <sup>91</sup>
2.5 cm, ~1 mm	CNT	PMMA//PDMS	1 V 150 nA (1 Hz)	50.9 V/cm <sup>3</sup> 7.6 $\mu$ A/cm <sup>3</sup>	Compression 10 N	stretchable	Journal of Materials Chemistry A 5, 6032–6037 (2017) <sup>89</sup>

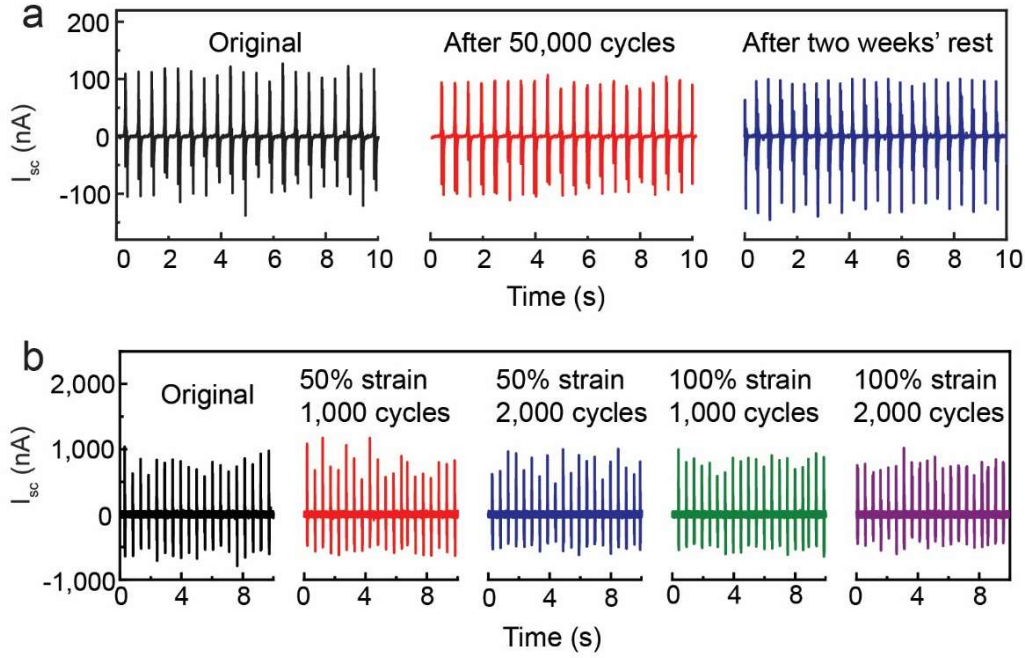


**Figure 3.11** (a) Long-term output stability tests under continuous pressing for 50 000 cycles, together with the outputs after being stored in ambient atmosphere for two weeks (contact length: 3 cm). (b) Variation of  $I_{sc}$  after fatigue stretching cycles under 50 % and 100 % strain for 2 000 cycles, respectively. A longer fiber with the contact length of 10 cm and a slightly larger pressure were used.

The output power of the fiber was investigated by externally connecting various resistors from 0.3 M $\Omega$  to 100 M $\Omega$  in series, and calculated as  $\frac{V^2}{R}$ , where  $R$  is the load resistance and  $V$  is the voltage across it. As shown in Figure 3.10d, the peak values of output voltage and calculated current on the resistors follow opposite trends as a function of the external resistance due to the Ohm's law. As the resistance increases from 0.3 M $\Omega$  to 99 M $\Omega$ , the voltage increases from 0.04 V to 2.38 V, while current decreases from 155.4 nA to 23.97 nA. The instantaneous output power achieves a peak value at a moderate  $R$  value. Since the principle of TENGs is based on electrostatic induction and has inherent capacitive behaviour, the output power  $P$  could also be expressed as:

$$P = \frac{V_{oc}^2 R}{|Z_c|^2 + R^2} \quad (3.1)$$

where  $V_{oc}$  is the open-circuit voltage of the fiber nanogenerator,  $|Z_c|$  is the magnitude of its internal impedance.<sup>112</sup> By fitting the output power values with this formula (indicated by a dash line in Figure 3.10d), we can find that the maximum output power is located at the load resistance of 17.4 M $\Omega$ . Thus, according to the load-match condition for maximizing the output power on the load, the magnitude of the fiber's internal impedance is estimated to be 17.4 M $\Omega$ .

To quantify the impact of repetitive deformation on the fiber's energy harvesting performance, we repeatedly compressed and relaxed the fiber at 2 Hz, while simultaneously monitoring the short-circuit current waveforms (Figure 3.11a). The magnitude of the current after 50 000 cycles remains 96% of its initial value. In addition, the reproducible output results after two weeks' rest further confirm its high reliability. The fibers were then subjected to repeated large elongation deformation. As shown in Figure 3.11b, the current from the fiber remains stable after being stretched to 50% and 100% strain values for 2 000 cycles. Therefore, we confirm that the fiber is capable of withstanding cyclic external compression and tensile forces while maintaining excellent energy harvesting performance for a long period of time. This can be attributed to the resilient mechanical properties of the elastomer and excellent electrical conductivities of the liquid metal under large deformation.

### 3.4 Woven triboelectric textiles for energy harvesting

Having characterized the fibers' mechanical and electrical output performance, we now turn to study its potential to be integrated into two-dimensional textiles for sustainable and self-powered applications. A conformal and stretchable textile (6 cm x 6 cm) was obtained by simply weaving a single continuous 4 m-long and 1.1 mm-thick triboelectric fiber, as shown in Figure 3.12a. The effective output parameters of the textile on various resistive loads show the same trends as with the short fiber, while the instantaneous power achieves its peak value at a lower resistance of about 8.2 M $\Omega$  (Figure 3.12b-c). To demonstrate the textile's ability to take advantage of human motions for energy harvesting, we monitored its short-circuit current waveforms while being mechanically stimulated. For instance, hand grasping of the textile can generate high values of  $V_{oc}$ ,  $I_{sc}$  and  $Q_{sc}$ , up to  $\sim 260$  V, 2.5  $\mu$ A and 85 nC respectively (Figures 3.12d-f). If a stronger stimulation like hand tapping is applied, the corresponding parameters can achieve as high as  $\sim 317$  V, 26  $\mu$ A and 130 nC respectively (Figures 3.12g-i). Such level of outputs are sufficient to power 100 light emitting diodes (LEDs) that are connected in reversed direction (Figures 3.13a-c).

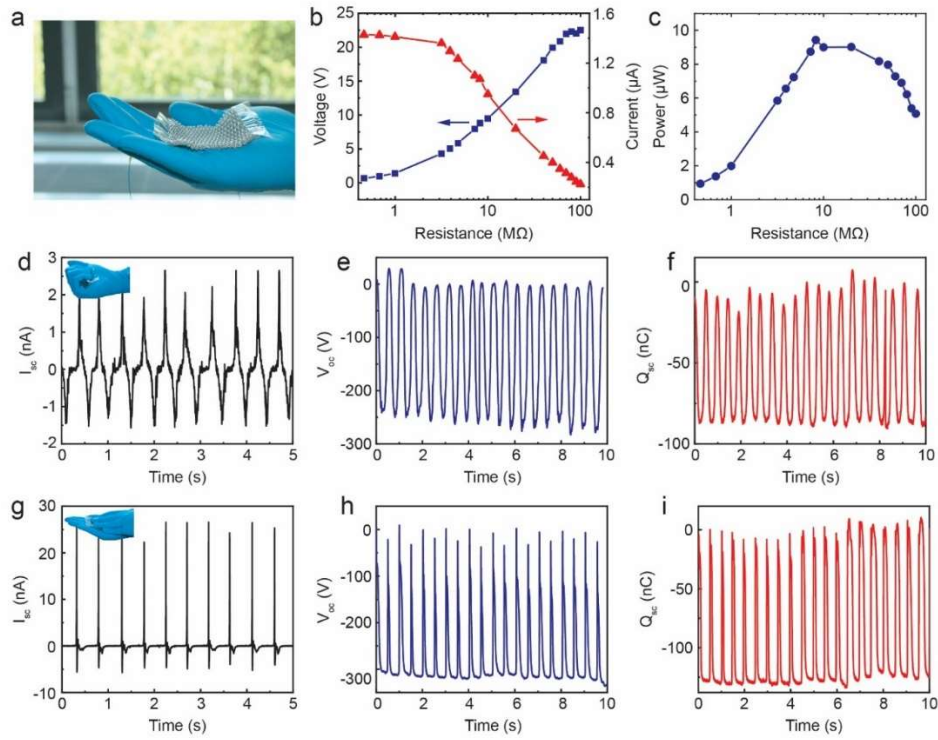


**Figure 3.12** (a) Photograph showing a continuous and long triboelectric fiber was woven to a textile. (b-c) Dependence of the output signals on the resistance of external loads. (d-i) Recorded output waveforms of the textile triggered by mechanical stimuli: hand grasping (d-f) and hand tapping (g-i).

Since TENGs produce pulsed and alternating output that cannot be exploited by most electronic devices, a rectifier circuit is necessary. Figure 3.13d shows the circuit diagram of a bridge rectifier to modulate outputs of the textile to charge a capacitor. As shown in Figure 3.13e, the alternating current can be effectively converted to positive or negative pulsating current as desired. Figure 3.13f shows the voltage versus time curves of two different commercial capacitors (10  $\mu\text{F}$  and 100  $\mu\text{F}$ ) that are charged by the rectified current generated by hand-tapping a functional textile. The electric energy stored in the capacitors could be further employed to continuously drive a LED (inset in Figure 3.13f), which confirms the capability of the textile to harvest sufficient mechanical energy from human daily motion to drive some portable electronic devices without any external power sources.

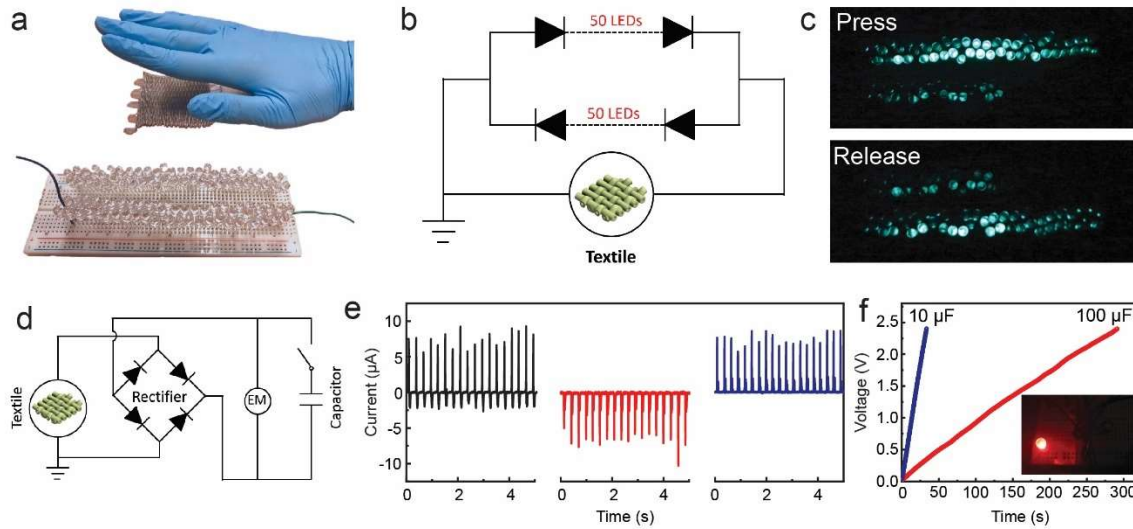


**Figure 3.13** (a-c) Demonstration of 100 LEDs lighted up by the textile under tapping. (d) Electrical circuit diagram of the textile connected with a bridge rectifier to charge a capacitor. (e) The output current of the textile before and after being rectified by a bridge rectifier. (f) Charging curves of two different capacitors connected to the textile. The inset shows a red LED can be continuously lighted up by a charged capacitor.

The flexibility associated with thermal drawing can be further exploited to fabricate triboelectric fibers with complex architectures for enhanced efficiencies. We demonstrate in particular fibers with multiple liquid metal-based electrodes or micro-textured surfaces shown in Figure 3.6b-d, both of which show enhanced output performance, as shown in Figure 3.14. To demonstrate the impact of such advanced micro-structuring, the electric output of a triboelectric textile (6 cm x 6 cm) formed by a micro-textured fiber was characterized, as shown in Figure 3.15. The peak values of  $V_{oc}$  and  $Q_{sc}$  triggered by hand tapping are as high as  $\sim 490$  V ( $13.6$  V/cm<sup>2</sup>) and  $\sim 175$  nC ( $4.86$  nC/cm<sup>2</sup>), which are estimated to be 55 % and 42% higher than the texture-free counterpart, respectively.



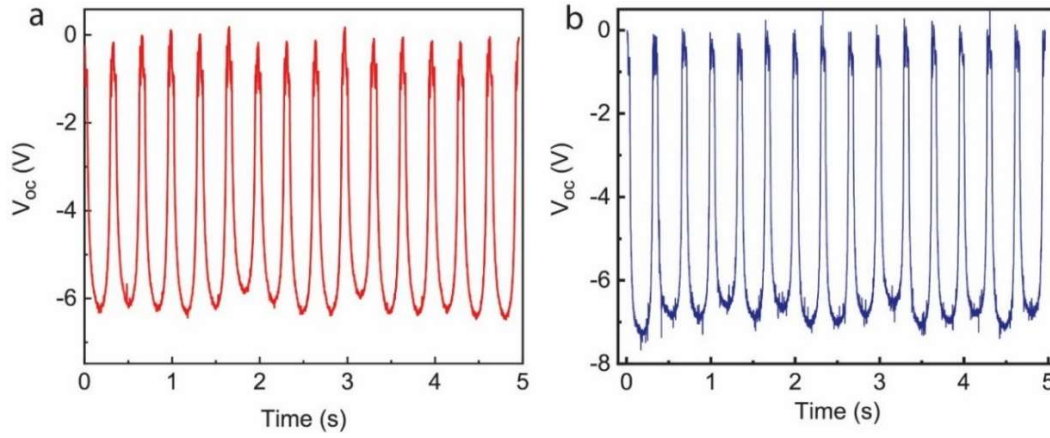


**Figure 3.14**  $V_{oc}$  of complex fiber structures with multiple electrodes (a) and micro-texture on surface (b). The effective contact length is 3 cm.

Here we evaluate the surface area enhancement of micro-textured fibers compared with the flat fibers without surface texture. Figure 3.16a-b show the original shape of the texture that we created at the preform level, which was well maintained on the fiber, despite slight structural smoothing. Based on the cross-section of the fiber, it is reasonable to approximate that the texture can be expressed by a sinusoidal function  $y(x) = h \sin(\frac{2\pi}{\lambda}x)$ , where  $h$  and  $\lambda$  are the amplitude and period of the perturbation respectively (Figure 3.16c). According to the original dimensional design in the preform,  $h$  is estimated to be  $\frac{\lambda}{4}$ . We compare the surface area of a sinusoidal patterned fiber with a smooth surface fiber in the range of one period, under the assumption that they have the same fiber length and cross-sectional diameter. We assume that the surface area enhancement is represented by  $\frac{s-\lambda}{\lambda}$ , where  $s$  is the arc length of the sine function over one period  $\lambda$ , which equals to  $\int_0^\lambda \sqrt{1 + y'^2(x)} dx$ . The calculated surface area enhancement is 46%, which can indeed host higher triboelectric charges. This result is consistent with the output increase of the textured fibers.

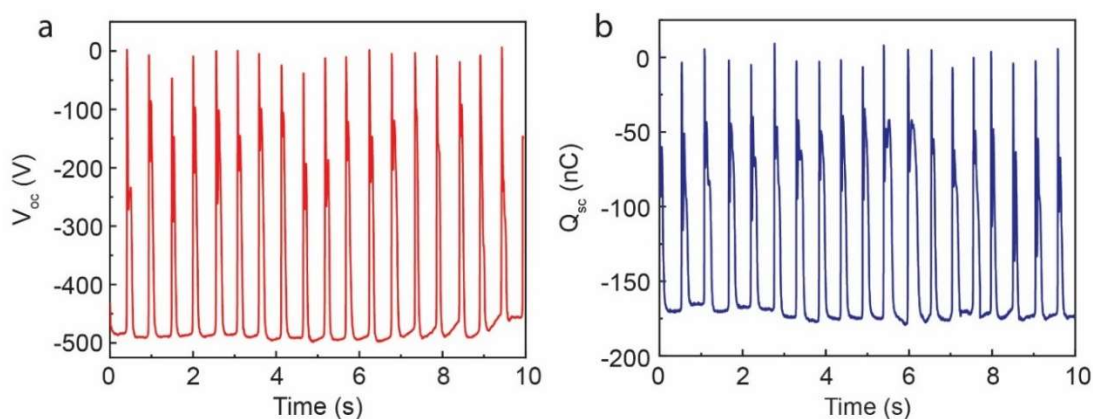


**Figure 3.15** The recorded  $V_{oc}$  and  $Q_{sc}$  of a 6 cm x 6 cm textile made up of a long micro-textured fiber, under the applied force of 25.5 N (7.1 kPa).

In Table 3.2, we summarized the used materials, dimensions, electrical outputs, and calculated electrical output densities (calibrated into unit area) of various textiles reported in recent years. From such a list, we conclude that the performance of our textile surpasses reported TENG textiles, and is comparable with, or even superior to, most 2D planar TENG configurations reported thus far.

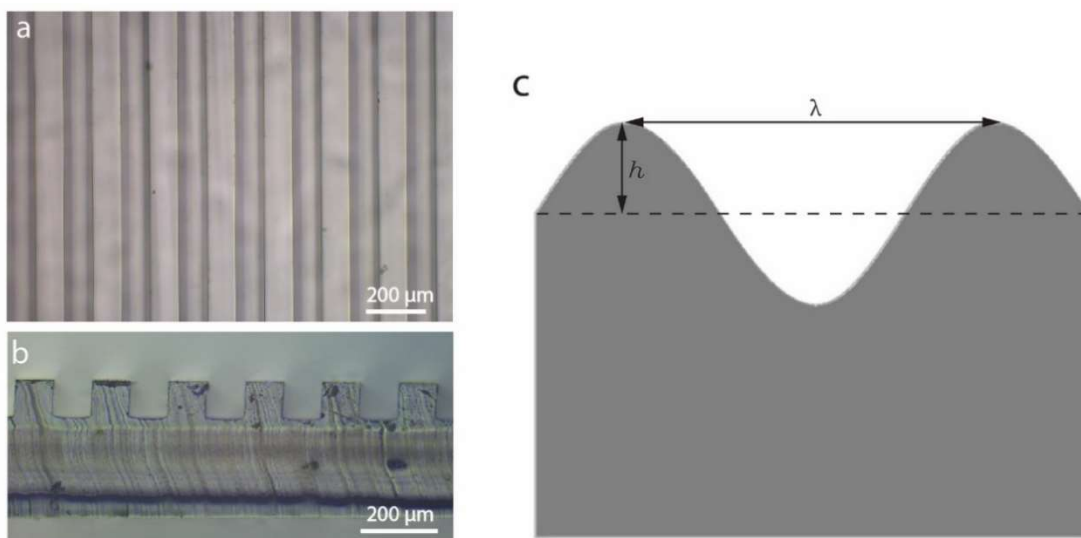


**Figure 3.16** (a, b) Textured Geniomer film for the fabrication of textured preforms. (c) Schematic of a sinusoidal surface on a textured fiber with relevant parameters.

**Table 3.2** Summary of the electrical output performance of the triboelectric textile in this work and other previously reported textiles.

Textile dimension (cm*cm)	Contact area (cm*cm)	Applied force/pressure	Electrode materials	Triboelectric materials	Electrical output	Electrical output per area	References
6*6	6*6	25.5 N 7.1 kPa	Liquid metal	Geniomer//Nitrile	490 V 175 nC	13.6 V/cm <sup>2</sup> 4.86 nC/cm <sup>2</sup>	This work
10*10	« not given »	« not given »	Ag	Ag//PTFE	23.5 V 1.05 $\mu$ A	0.2 V/cm <sup>2</sup> 0.01 $\mu$ A/cm <sup>2</sup>	ACS Nano 11, 10733–10741 (2017) <sup>113</sup>
16.5*11.4	« not given »	« not given »	Stainless steel thread	Silicone//skin	200 V 200 $\mu$ A	1.06 V/cm <sup>2</sup> 1.06 $\mu$ A/cm <sup>2</sup>	Advanced Functional Materials 27, 1604462 (2017) <sup>98</sup>
5*10	5*10	« not given »	Ag fiber fabric	Nylon//polyester	90 V 1 $\mu$ A	1.8 V/cm <sup>2</sup> 0.02 $\mu$ A/cm <sup>2</sup>	ACS Applied Materials and Interfaces 6, 14695–14701 (2014) <sup>114</sup>
4*4	4*4	11 N 6.9 kPa	Stainless steel	Silicone//acrylic	150V 2.9 $\mu$ A (5Hz) 52 nC	9.4 V/cm <sup>2</sup> 0.18 $\mu$ A/cm <sup>2</sup> 3.25 nC/cm <sup>2</sup>	ACS Nano 11, 9490–9499 (2017) <sup>93</sup>
4.5*8	4.5*8	« not given »	Stainless steel	Polyurethane//polyester	75 V 1.2 $\mu$ A(1Hz)	2.1 V/cm <sup>2</sup> 0.03 $\mu$ A/cm <sup>2</sup>	ACS Nano 11, 12764–12771 (2017) <sup>115</sup>
4.0*4.5	1.5*1.5	« not given »	Stainless steel	PDMS//unknown external substrate	20 V 0.1 $\mu$ A (5Hz) 7 nC (data of one-dielectric-layer)	8.9 V/cm <sup>2</sup> 0.04 $\mu$ A/cm <sup>2</sup> 3.1 nC/cm <sup>2</sup>	Advanced Materials 29, 1702648 (2017) <sup>90</sup>
10*10	10*10	« not given »	Ni	Parylene//cotton	40 V 5 $\mu$ A (5Hz)	0.4 V/cm <sup>2</sup> 0.05 $\mu$ A/cm <sup>2</sup>	Advanced Materials 28, 98–105 (2016) <sup>116</sup>
5*6	5*6	« not given »	Helical structure stainless steel	Silicone//stainless steel	31.8 V	1.06 V/cm <sup>2</sup>	Nature Communications 10, 868 (2019) <sup>109</sup>
1*1	1*1	9.8 N 98 kPa	Al, conductive fabric	Nylon//PVDF	2 V 0.2 $\mu$ A	2 V/cm <sup>2</sup> 0.2 $\mu$ A/cm <sup>2</sup>	Journal of Materials Chemistry A 6, 22879–22888 (2018) <sup>117</sup>
6*6 (circle)	6*6 (circle)	10 to 20 N 3.5 to 7 kPa	Al foil	PVA/Mxene//silic fibroin	118.4 V (10 Hz)	4.2 V/cm <sup>2</sup>	Nano Energy 59, 268–276 (2019) <sup>118</sup>
4*4	« not given »	« not given »	Cu	PTFE//Cu	70 V 50 $\mu$ A	4.4 V/cm <sup>2</sup> 3.12 $\mu$ A/cm <sup>2</sup>	Nature Energy 1, 16138 (2016) <sup>119</sup>

5*5	5*5	10 N 4 kPa	PEDOT: PSS coated textile, Al	PEDOT:PSS coated textile/PTFE	49.7 V 0.787 $\mu$ A	2 V/cm <sup>2</sup> 0.03 $\mu$ A/cm <sup>2</sup>	Nano Energy 57, 338– 352 (2019) <sup>120</sup>
4*4	4*4	10 N 6.25 kPa	Conducti ve fabric	PVDF/PTFE//s kin	112.7 V 1.98 $\mu$ A	7 V/cm <sup>2</sup> 0.12 $\mu$ A/cm <sup>2</sup>	Nano Energy 58, 750– 758 (2019) <sup>121</sup>
6*4	6*4	« not given »	Cu	Cu//polyimide	4.98 V 15.5 mA/m <sup>2</sup>	0.2 V/cm <sup>2</sup> 1.55 $\mu$ A/cm <sup>2</sup>	Advanced Materials 28, 10267–10274 (2016) <sup>96</sup>
5*5	5*5	« not given »	Ni cloth	Parylene//Ni	50 V 4 $\mu$ A	2 V/cm <sup>2</sup> 0.16 $\mu$ A/cm <sup>2</sup>	Advanced Materials 27, 2472–2478 (2015) <sup>122</sup>
10*10	10*10	1400 N 140 kPa	Cu sheet	Cu//PDMS	~195 V	1.95 V/cm <sup>2</sup>	Nano Energy 58, 365– 374 (2019) <sup>123</sup>
5.3*2.9	5.3*2.9	« not given »	Liquid metal	Silicone	~120 V	7.8 V/cm <sup>2</sup>	ACS nano 12, 2027– 2034 (2018) <sup>97</sup>
5*5	5*5	300 N 120 kPa	Ni	Silicon rubber, Ni//skin	300 V 30 $\mu$ A	12 V/cm <sup>2</sup> 1.2 $\mu$ A/cm <sup>2</sup>	Nano Energy 39, 562– 570 (2017) <sup>124</sup>
3*3	1.5*1.5	« not given »	Au	Water//HCOEN P	15 V 4 $\mu$ A	6.7 V/cm <sup>2</sup> 1.8 $\mu$ A/cm <sup>2</sup>	Advanced Energy Materials 7, 1701243 (2017) <sup>125</sup>
6*5	6*5	« not given »	Carbon wire	PTFE//carbon wire	~175 V 8 $\mu$ A	5.8 V/cm <sup>2</sup> 0.27 $\mu$ A/cm <sup>2</sup>	Nano Energy 50, 536– 543 (2018) <sup>126</sup>
5*5	5*5	1 N 0.4 kPa	Ag	PET//silicone	45 V	1.8 V/cm <sup>2</sup>	Materials Today 32, 84–93 (2019) <sup>127</sup>
7*7	7*7	5 N 1 kPa	Ag flake/ PDMS	Skin//HCOENP s/BP/PET	350 V	7.1 V/cm <sup>2</sup> 0.65 $\mu$ A/cm <sup>2</sup> (2 Hz)	Nature Communications 9, 4280 (2018) <sup>128</sup>
9*10	9*10	« not given »	Ag- coated fabric	PTFE//cotton yam/Ag (free- standing mode)	900 V 19 $\mu$ A	10 V/cm <sup>2</sup> 0.21 $\mu$ A/cm <sup>2</sup>	Nano Energy 58, 375– 383 (2019) <sup>129</sup>

Note: The calculation of electrical contact per area is calculated based on the contact area provided it is known. As for the devices with unknown contact area, the calculation is based on the textile dimension.

### 3.5 Demonstration of wearable applications of triboelectric fibers and textiles

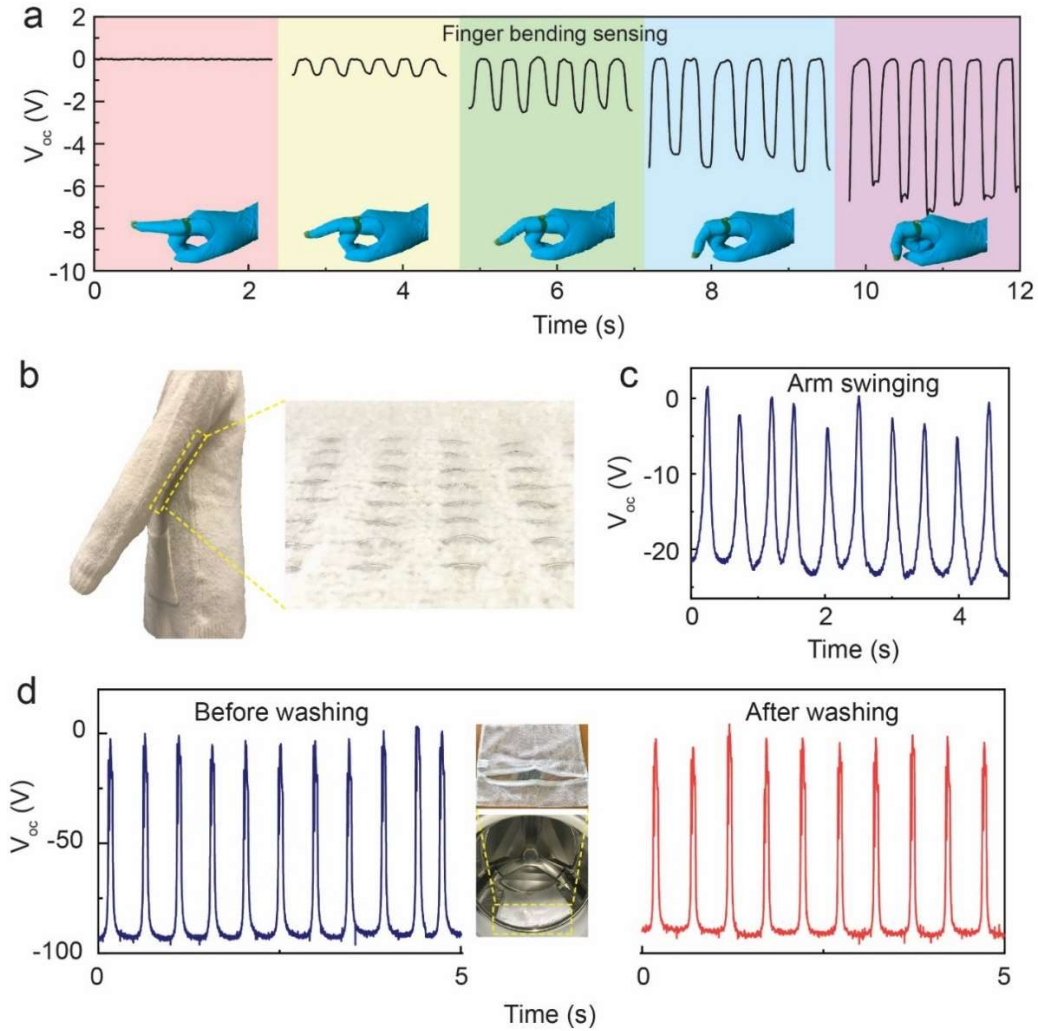


**Figure 3.17** (a) Demonstration of the fibers as self-powered sensors to monitor finger bending conditions. (b, c) Photographs and corresponding  $V_{oc}$  of a triboelectric fiber-integrated sweater to extract energy from human arm swing. (d) Comparison of the voltage output of the textile before and after being washed in a laundry machine. The inset image shows a water-permeable protective sack with the textile placed in a household laundry machine.

As we have shown, triboelectric fibers can generate electrical signals when triggered by an external force. The collected signals can be utilized to extract characteristics of the mechanical stimuli, assigning the fiber a second function – self-powered sensor.<sup>110,130</sup> Here, a finger gesture sensor was built by simply attaching the triboelectric fiber onto a glove, and was characterized by recording its output when the

index finger is bent. As shown in Figure 3.17a, the amplitude of the  $V_{oc}$  waveforms increases gradually with the increasing bending angle, indicating an opportunity of the soft fiber as a wearable self-powered mechanical sensor. In particular, this fiber design shows interesting advantages, compared to many other fiber-shaped mechanical sensors that suffer from the problems of low sensitivity, limited sensing range, or structural and functional damage when exposed to large deformation.<sup>131</sup>

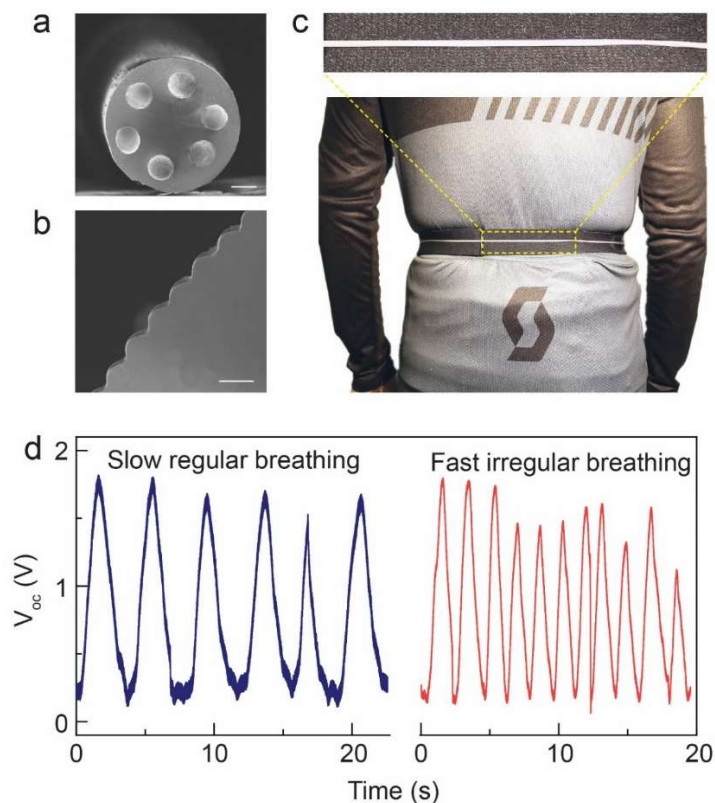


**Figure 3.18** Breathing monitoring with self-powered triboelectric wearable sensor. The fiber features six embedded electrodes (a) and a microtextured surface (b) for improved performance. The fiber is fixed on a stretchable belt, which is worn around the torso (c). (d) The generated waveforms allow the quantitative assessment of breathing patterns. Scale bars: (a) 200  $\mu\text{m}$ , (b) 10  $\mu\text{m}$ .

A peculiarity of the thin and soft fibers lies in their possibility to be integrated within textiles using a variety of well-established techniques such as knitting and weaving. As shown in Figure 3.17b, we integrated soft triboelectric fibers into commercial clothes for the construction of functional clothing. Driven by the friction from a swinging arm between the fiber and the sweater, an output voltage of  $\sim 22$  V was produced (Figure 3.17c). For wearable electronic products, the endurance to day-to-day handling,

like machine washing, is also one of the most critical factors determining their viability in practical settings. The electrical outputs of the textile before and after washing in a laundry machine for 40 min are almost identical (Figure 3.17d), indicating its good tolerance to harsh conditions such as water infiltration and the impact force induced by the machine. Such performance can be attributed to the high deformability of the fiber together with the thick elastomeric cladding that protects the fiber inner structure.

Finally, as shown in Figure 3.18a-b, we propose a novel fiber design with a surface texture and up to six liquid metal electrodes, to realize a highly sensitive self-powered deformation sensor to monitor breathing. To demonstrate the potential application of such a fiber, we built a breathing monitoring belt by fixing the fiber extremities to the two ends of a longer stretchable belt. Tightly worn around the torso as shown in Figure 3.18c, the outward and inward movements of upper chest and abdomen result in the elongation /release of both the belt and the fiber, inducing friction between the two due to their different intrinsic deformation behaviour. This slight relative movement generates an electrical signal that can be detected, enabling the monitoring of breathing patterns as shown in Figure 3.18d.

### 3.6 Methods

*Polymer comparison:* The commonly used insulative thermoplastic polymers for thermal drawing were compared using the metrics of Young's modulus and relative triboelectric polarity. The value of Young's modulus for Geniomer was experimentally determined from mechanical tensile tests, while the other polymers were directly taken from corresponding data sheets or from literature.<sup>48</sup> The triboelectric polarity of the materials was determined from the electrical outputs of a series of self-constructed contact-mode 2D TENG devices with the selected polymer films as the dielectric surfaces (Figure 3.19).

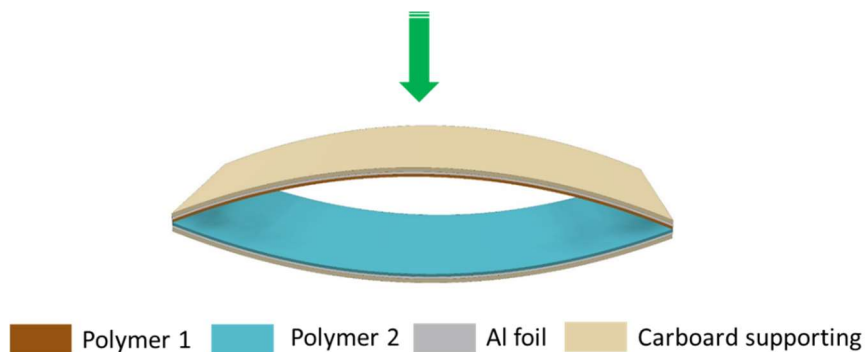


**Figure 3.19** Schematic showing 2D planar TENG devices (contact-mode). Such devices are used to determine relative triboelectric polarity of the tested polymers in this work.

*Fabrication of triboelectric fibers:* The hollow-core cylindrical preforms were fabricated by consolidating Geniomer granules (140, Wacker Chemie AG) within molds at 175 °C in a vacuum consolidation oven. The length and diameter of the preform are 120 mm and 29 mm respectively. The micro-textured Geniomer preforms were created by rolling a thin layer of Geniomer film with predefined texture onto the abovementioned cylindrical preforms, followed by consolidation at 170 °C for 15 min under vacuum. The fabrication of the micro-textured Geniomer film is as follows. Micro-patterns with the defined period of 100  $\mu\text{m}$  were created on silicon masks via photolithography process at the Centre for Micro-Nanofabrication (CMi) at EPFL. The patterns were made by a Heidelberg DWL200 laser writer on Cr-blank masks, then transferred to silicon masks by a Suss MA6 mask aligner. Afterwards, the as-developed silicon masks were etched by a plasma etcher (Alcatel AMS 200 SE) to obtain the expected depth of 100  $\mu\text{m}$ , which was designed to be the same as the width of the patterns, to get square shaped patterns. The patterns were subsequently transferred to PDMS substrates by molding the silicon masks onto PDMS solution via casting (Sylgard 184 Dow-Coring) and curing at 80 °C. Geniomer thin films were prepared by hot pressing polymer granules under vacuum at 175 °C using a custom-built hot-press (Laboratoire Presse, LAUFFER GmbH & Co. KG). Then the films were patterned by pressing on the patterned PDMS molds under vacuum at 170 °C.

Finally, the preforms were drawn into long fibers with a custom-built draw tower. The setting temperature for top, middle and bottom zones were 90 °C, 230 °C and 70 °C, respectively. The preform was fed into the furnace at a speed of 1 mm/min, while the drawing speed was tuned with a wide range of 0.05-0.6 m/min to obtain fibers with controllable draw-down ratio.

*Characterizations:* Scanning electron microscopy (SEM) was conducted on a Zeiss Merlin field emission SEM with an acceleration voltage of 3 kV using the In-Lens detector and Analytic Column Mode. The fiber samples for SEM characterizations were prepared by immersing them into liquid nitrogen for several minutes followed by an immediate cutting at room temperature. All the samples were coated with a 10 nm Au film before characterization.

The rheological characterization of Geniomer was carried out on a TA Instruments AR 2000 Rheometer. The polymer plates (1500  $\mu\text{m}$  thick) were cooled at 1 °C/min, and the angular frequency



was 0.03 rad/s. The mechanical tensile tests of the fibers were conducted on a universal testing machine (UTS) Series LFM-125 kN (*Walter+Bai AG*) with the tensile mode (1 kN load cell, 2 mm/s). Five samples were characterized for each fiber type. The calculation of Young's modulus from the stress-strain curves is limited to the low strain region of less than 10% strain. The washing ability of the textile was characterized by putting the textile into a water-permeable protective sack and the whole sack was put into a household laundry machine. The washing process lasted for about 40 min, after which the textile was dried in ambient condition.

*Electrical measurements:* The electrical connection for the fibers was realized by contacting metallic wires to liquid metal electrodes followed by sealing with epoxy. The resistance of liquid metal electrodes was measured by an electrical testing instrument (Keithley 2450 Sourcemeter). A programmable electrometer (Keithley, model 6517) was utilized to measure the output signals of the triboelectric fibers and textiles. The data were collected and recorded by a Digilent Analog Discovery and computer-controlled software written in Labview. Custom setup composed of DC motors were used to apply cyclic pressing and stretching force to the tested fibers.

### 3.7 Summary

In this chapter, we demonstrated a simple and scalable fabrication approach of microstructured highly stretchable TENG fibers with architectures of unprecedented complexity and performance on par with state-of-the art TENG devices. The fibers consist of a thermoplastic elastomeric cladding that surrounds one or multiple liquid metal electrodes, co-processed via the multi-material thermal drawing technique. The produced fibers exhibit high stretchability with a fracture strain as high as 560 %. We showed that the fibers could maintain stable performance even after 50 000 cyclic compression and long-term large deformation operations. We further optimized the energy harvesting performance by integrating multiple electrodes and introducing textured pattern to the elastomer surface, resulting in a triboelectric textile with  $V_{oc}$  and  $Q_{sc}$  reaching as high as 490 V and 175 nC respectively. The fabrication process we developed is scalable and enables kilometers long fibers to be yielded from a single preform, leading to promising possibilities for large area, flexible and soft sensing and energy harvesting systems. For example, preforms in the optical fiber industry can produce  $10^3$  km of 0.5 mm thick TENG fibers in a single draw. Integrated via various textile-based technologies, a 500 m<sup>2</sup> fabric could be fabricated, that could generate a current as high as 3.5 A, enough to work as reliable power sources for smartphone

batteries. Another advantage of our strategy is the high flexibility of the design of complex fibers at the preform level such as textured surfaces or multiple electrodes. The compatibility with textile integration techniques also opens novel avenues for advanced designs and self-powered functionalities within implants, wearable systems and smart textiles. The self-powered and highly sensitive breathing monitoring application we demonstrated is being developed for the detection of early signs of breathing difficulties relevant for a variety of medical condition in sleep pathologies or severe viral symptoms. We envision that this work not only has a significant impact in the fields of energy harvesting and functional fiber processing, but also provides opportunities for the advancement of other functional fiber and textile-based electronics.

## Chapter 4 Design and fabrication of self-encapsulated and stretchable multi-material triboelectric fibers

Soft and intelligent artificial skins and textiles are envisioned to be versatile platforms for applications in health monitoring, soft robotics, and human-machine interfaces.<sup>22</sup> Their advantages over conventional portable and wearable devices consist in the ability to establish comfortable and conformal interfaces with the skin or other body parts. With few exceptions, all of these flexible and often soft/stretchable devices require reliable electrical power sources to support their long-term and self-sustainable operations for sensing, wireless communication or signal processing.<sup>123</sup> Conventional batteries remain the most widely used options, however, their stiffness, weight, dimensions and the use of hazardous chemicals heavily restrict the designs for skin interfacing applications. This challenge has driven numerous research in advanced energy harvesting technologies that can generate electricity using ambient power sources such as solar, body motion, sweat, or heat flux. Nonetheless, the simultaneous realization of stable electrical output performance and skin-compatible mechanical attributes on these power suppliers still remains a significant challenge. Current strategies often involve the stacking of multiple flexible and soft functional materials into 2D planar structures, yet the resulting devices are bulky, and the deformability is still limited. In contrast to standard 2D devices, networks of functional fibers, yarns or textiles represent outstanding alternatives toward large-area and conformal energy harvesting to power microdevices, while being fully unobtrusive.<sup>17</sup> In addition to the secondary advantages such as low cost, breathability, robust, and washability, the unrivalled flexibility of these discrete fiber assemblies, in particular, allows the simultaneous deformations of large extension, double-curvature bending and in-plane shear.<sup>2</sup>

In recent efforts, advanced micro/nanofabrication has made it feasible to impart TENG functions to flexible or stretchable fibers for mechanical sensing or energy harvesting from mechanical deformations.<sup>130</sup> These fiber devices often operate in the single-electrode or contact-separation mode.<sup>132</sup> The former working mode devices are easy to fabricate and convenient to use, yet the outputs are unstable and largely depend on the contact material and ambient environment.<sup>98</sup> The latter choice often involves the construction of a cylindrical core-sheath structure with a gap existing between the inner core column and the outer sheath tube.<sup>111</sup> The sheath works as a barrier to prevent the direct interface between the inner triboelectric surfaces and ambient environment. Although a multitude of contact-

separation mode fiber constructs have been demonstrated by exploiting diverse materials and processing strategies that center in coating, wrapping, and molding, they essentially share the same structural design philosophy as explained above.<sup>89,91</sup> More importantly, the short lengths – generally at the scales of several to tens of centimeters, and the multistep processing approaches that are exclusive to the laboratory scale, drastically preclude their mass production and application. Another strategy comprises the direct utilization of existing scalable fiber processing techniques such as extruding, thermal drawing or spinning. Among them, thermal drawing is particularly applicable because this technique allows the co-processing of conductive and insulative materials into functional fibers with extremely long length, complex and thin architecture, as well as intricate functions. In addition to the fibers we developed in the last chapter, different thermally drawn TENG fibers have also been demonstrated by other groups.<sup>133,134</sup> Nevertheless, triboelectric fibers work in the contact-separation mode, especially with desired mechanical deformability and resilience against water in-take or other harsh environment conditions, have not been demonstrated to date. Moreover, the in-depth understanding and modeling of mechanical deformations of soft TENGs, which dominate the sensing and energy harvesting functions, remain to be explored.

In the following two chapters, we will discuss the design, fabrication and characterization of a soft and stretchable contact-separation mode triboelectric fiber. With a unique rectangular geometry in cross-section, it is composed of two triboelectric parts that are separated by a large air gap. The whole structure is encapsulated by a water-resistant elastomeric cladding – SEBS. A stretchable and conductive composite forms the main electrode material, and an extra liquid metal channel is added to interface the composite, for the purpose of increasing the overall electrical conductivity of the electrodes along the fiber axis and thus reducing energy loss. In this chapter, we will first explain the reasons why SEBS is identified as the encapsulating material, through the characterizations of water droplet contact angle and water vapor transmission rate. Then we will discuss the fabrication and microstructural, electrical and mechanical characterizations for the stretchable and conductive composite material. In addition, in order to enhance the electrical performance of the fiber device, we took another challenge in the structural design – adding micro-textures on the inner surfaces of the structure. The use of a suitable sacrificial layer to reduce the thermal reflow during fiber processing will be discussed with the emphasis on the studies of surface/interfacial tension of the involved materials.

## 4.1 Identification and characterization of the encapsulating material

Previous studies suggest that moisture can significantly eliminate the triboelectric charges on the dielectric surfaces and largely impair the output performance. The output signal can degrade to almost zero at high relative humidity (RH) of 90%.<sup>135</sup> Thus, it is necessary to build an embeddable and fully encapsulated design of TENGs in order to sustainably generate electricity even in harsh environment. To achieve this function, we propose to design and fabricate a vertical contact-separation mode-based triboelectric fiber, given the compatible structural design and achievable trigger force for this working mode in the fiber level. As shown in Figure 4.1, the fiber consists of two triboelectric parts that are separated by a large air gap within a highly elastic cladding. In addition to the proper structure, the interaction of the encapsulating material with water molecules, which plays a key role in determining the RH that the triboelectric layers can be exposed to, should be also considered.

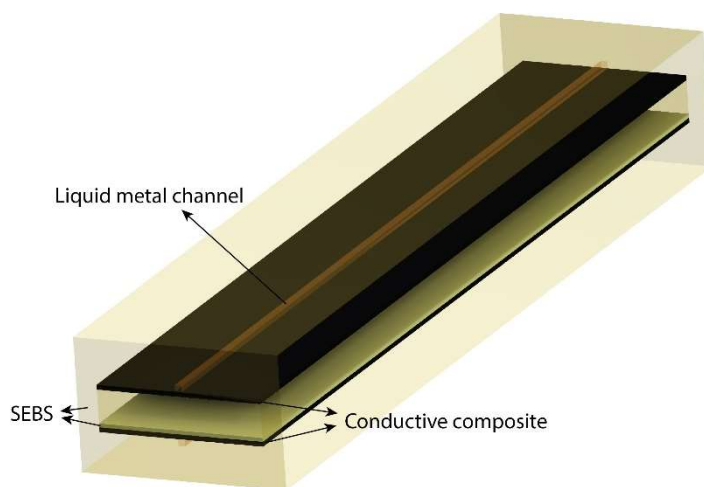


**Figure 4.1** Schematic showing the structure of a vertical contact-separation mode based triboelectric fiber.

First, we need to identify a series of compatible materials for our design. SEBS is considered as a suitable candidate material for the encapsulating layer because of its high deformability, proper rheological behaviors that are compatible with thermal drawing,<sup>48</sup> as well as good adhesion with other processable materials. Since SEBS only contains carbon hydrogen bonds that do not possess regions of positive and negative charges, it is nonpolar and should exhibit a hydrophobic behavior.<sup>136</sup> To confirm

this property, we measured the sessile drop contact angle of a DI water drop on a clean SEBS film. As shown in Figure 4.2, the resultant angle is around  $104.4^\circ$ , demonstrating the hydrophobicity of SEBS.

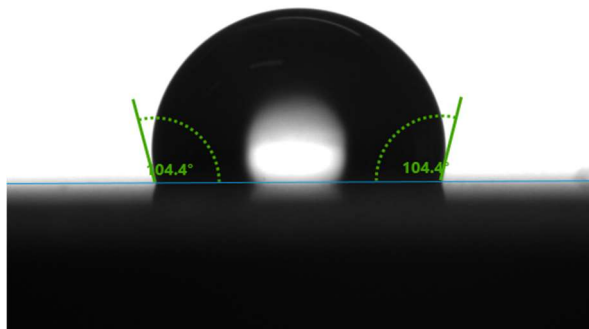


**Figure 4.2** A water drop on a SEBS film showing the contact angle of approximately  $104.4^\circ$ .

In addition to the tendency to repel liquid water, the ability to resist the diffusion of water vapor molecules is also critical for the proper function of a cladding material. In general, inorganic materials such as silicon dioxides and silicon nitrides show very low water permeabilities and are used as sealing materials for electronic devices. Although the inorganic coating can be very thin, they are still hard and brittle, making them unsuitable as packaging materials for stretchable devices. A good compromise between water permeation property and mechanical stiffness, plastics are widely used as packaging materials for food and drug, but they suffer from the insufficient deformability for stretchable devices. While elastomers are stretchable, due to the high mobility of their long chains, they generally have a high internal energy that is sufficient to create the excess free volume for the rapid diffusion of small molecules. This effect reduces the activation energy of diffusion and thus leads to a higher diffusion coefficient and a high permeability coefficient.<sup>137,138</sup> For example, it was reported that water vapor transmission rate (WVTR) of cured widely used 10:1 Sylgard 184 PDMS is  $708.1 \text{ g m}^{-2} \text{ day}^{-1}$  for a  $92 \text{ }\mu\text{m}$  thick film, which is  $65.1 \text{ g mm m}^{-2} \text{ day}^{-1}$  after thickness calibration.<sup>139</sup> This value is significantly higher than the values of silicon nitrides ( $\sim 10^{-6} \text{ g mm m}^{-2} \text{ day}^{-1}$ )<sup>140,141</sup> and even common polymers (several to tens of  $\text{g mm m}^{-2} \text{ day}^{-1}$ )<sup>142</sup>.

In this work, we measured the WVTR of  $\sim 200 \text{ }\mu\text{m}$  thick SEBS films through a water vapor transmission tester. The average WVTR at the temperatures of 15, 25, 35, and  $45^\circ\text{C}$  are 0.23, 0.555, 1.055, and  $2.315 \text{ g m}^{-2} \text{ day}^{-1}$  respectively. Normalizing with the sample thickness yields the WVTR

values of 0.046, 0.111, 0.211, and 0.463 g mm m<sup>-2</sup> day<sup>-1</sup> respectively. These values are similar to the previously reported WVTR for Kraton G1643 (with a polystyrene content of 20%) and G1645 (with a polystyrene content of 11.5-13.5%).<sup>143</sup> We roughly compare the measured WVTRs of SEBS with other various polymeric materials in Figure 4.3a. We can find that the values of SEBS are lower than most of the listed polymers, and in particular are 100 times lower than the commonly used PDMS. This can be ascribed to the contribution of the hard styrene segment in SEBS. Previous studies on block copolymers, such as polyurethane, showed that gas permeability increases with the decreased content of the hard segment.<sup>138,144</sup>

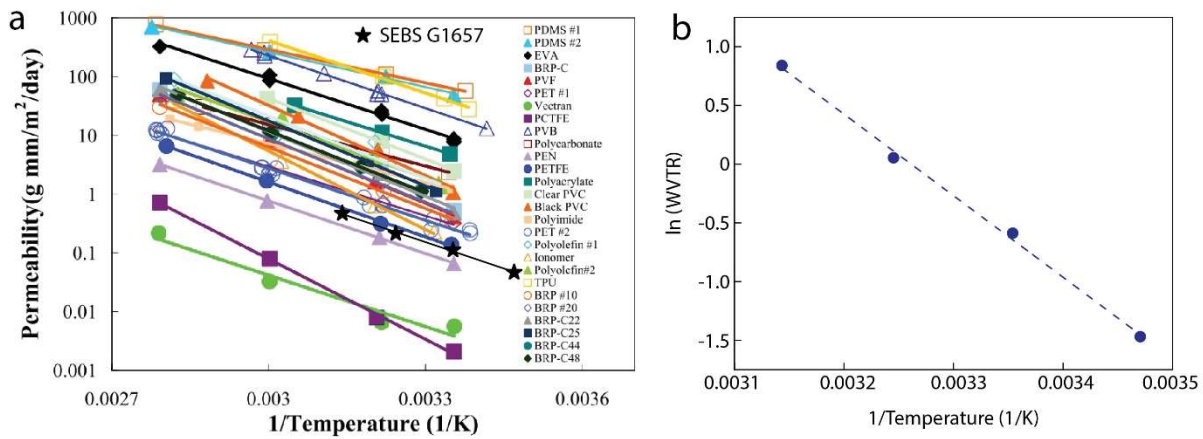


**Figure 4.3** (a) Water vapor permeability at various temperature conditions for SEBS G1657 and other various polymeric materials. The figure is adapted from a literature.<sup>142</sup> Polydimethylsiloxane (PDMS), Ethylene Vinyl Acetate (EVA), experimental film from Buckeye Rubber Products (BRP), Polyvinylfluoride (PVF), Polyethylene Terephthalate (PET), Poly chloro trifluoro ethylene (PCTFE), Poly vinyl butral (PVB), Poly Ethylene Napthalate (PEN), Polyvinylchloride (PVC), and Thermoplastic Polyurethane (TPU). (b) The logarithm of WVTR values of SEBS as a function of 1/T for the extraction of its permeation activation energy.

In addition, the experimental WVTR data for SEBS suggests that the permeability is enhanced with the increased temperature. According to Bertuzzi et al., this is due to the enhanced motion of the polymer segments as well as the increased energy of the water molecules, which contribute to the accelerated diffusion of water vapor through the sample.<sup>145</sup> Such a temperature dependency of WVTR was evaluated using an Arrhenius relationship described by Bertuzzi et al.:

$$\text{WVTR} = \text{WVTR}_0 \exp(-E_p/RT) \quad (4.1)$$

where  $WVTR_0$  is a pre-exponential factor,  $E_p$  is the activation energy of permeation that defines the energy barrier to be overcome for water vapor to permeate through the sample,  $R$  is the universal gas constant, and  $T$  is the absolute temperature. By plotting the logarithm of  $WVTR$  versus  $1/T$ ,  $E_p$  can be determined from the slope of the linear fitting, as shown in Figure 4.3b. The resultant value of  $E_p$  is 57.7 kJ/mol, which is even higher than some common polymers including LDPE (low density polyethylene, 33.5 kJ/mol), PP (polypropylene, 42.3 kJ/mol), PVC (polyvinyl chloride, 22.9 kJ/mol).<sup>145</sup> The above analysis confirms that the SEBS can be a good encapsulating material for stretchable devices.

## 4.2 Fabrication and characterization of stretchable and conductive electrodes

For the purpose of developing stretchable fiber-based TENG devices, it is particularly important to find a suitable electrode material that gathers features of high elasticity, good electrical conductivity, as well as thermal drawing compatible rheological properties. For contact-induced triboelectricity, we need electrodes with a large surface area that come into contact. This precludes the use of liquid metal as done in the previous chapter, since the low viscosity and high surface tension of liquid metal during drawing would always drive the electrode to break-up into filaments. One strategy, based on previous experiences drawing thermoplastic nanocomposites,<sup>25,28</sup> is to use elastomer composites filled with conducting nano-objects. Among the various fillers, carbon nanotubes (CNTs) possess unique properties such as large aspect ratio and great conductivity, making it a good filler in elastomeric matrix to achieve high electrical conductivities. The conductivity of a junction between two CNTs depends on the distance between them. Even if not overlapping, a short CNT inter-distance can result in finite electron conduction of the junction via the tunneling effect. The formation of a conductive percolation network of CNTs depends on their concentration, alignment and dispersion within the matrix. CNTs are insulated when the concentration is too low. After a certain critical content (percolation threshold), continuous CNT junctions throughout the composite are formed and thus the conductivity increases sharply before reaching a constant value. At higher concentrations, the distribution of CNTs is difficult and large amount of aggregates are formed, meanwhile the processing becomes difficult because the viscosity of the composite increases drastically with the CNT content.



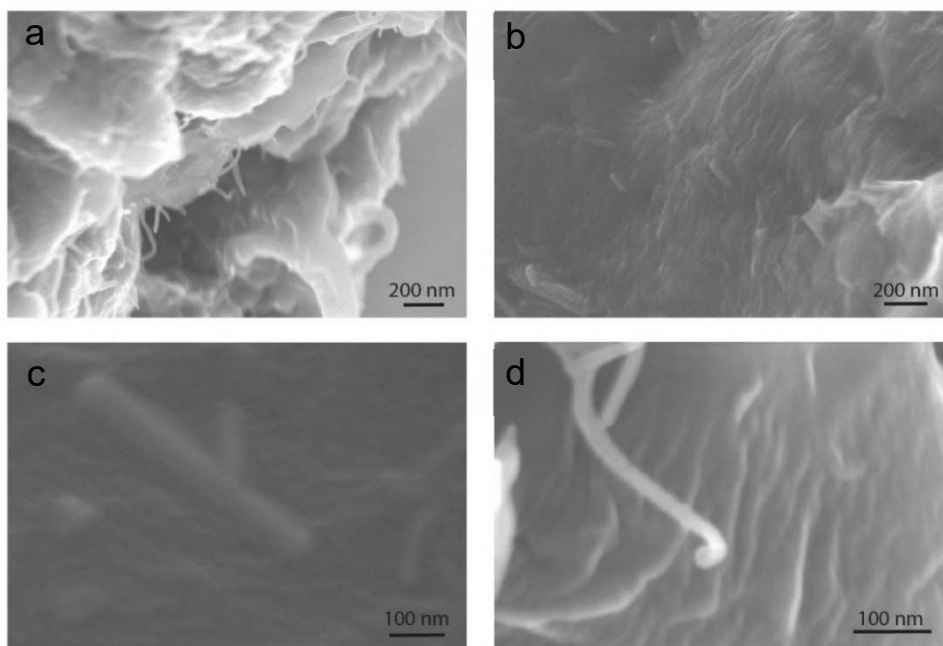


**Figure 4.4** SEM images of a CNT / HDPE / SEBS composite film before thermal drawing.

Colleagues of mine at FIMAP have been working on the fabrication of conductive composites by dispersing CNTs in SEBS and high-density polyethylene (HDPE). HDPE is a semicrystalline polymer that melts at around 115-135 °C. The addition of HDPE can lower the viscosity of the composite at high temperature and thus ease the drawing process. The concentrations of the three components play a vital role in the final properties including conductivity, stretchability and drawability. After a series of experimental study, a material combination of 6% CNT, 34% HDPE and 60% SEBS was selected.

The SEM images of the composite before and after drawing are shown in Figures 4.4 and 4.5 respectively. The diameter of the CNTs ranges from 25 nm to 55 nm. From the figures we can see that the local dispersion of the CNTs in the matrix is homogeneous, despite the formation of a few CNTs agglomerates. The homogeneous dispersion along the fiber axis will be demonstrated via electrical characterization. The aggregation of CNTs in polymer matrix is inherent if there is no extra physical or chemical treatment, because of their high aspect ratios and large surface area, and the resulting high intrinsic van der Waals interactions between the tubes.<sup>146</sup>

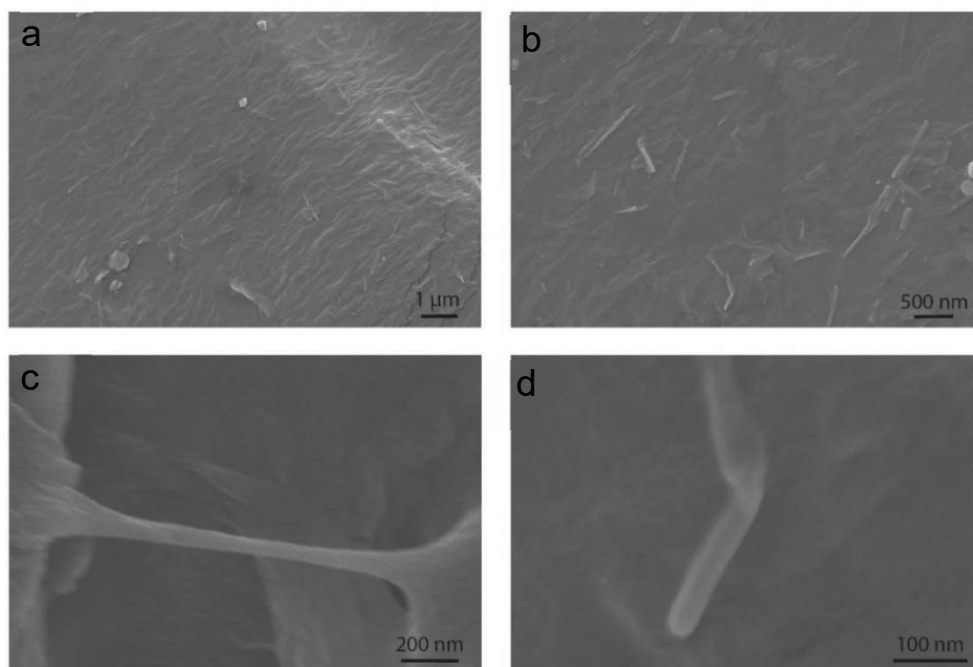


**Figure 4.5** SEM images of the CNT / HDPE / SEBS composite after thermal drawing.

To evaluate the distribution of CNTs, we performed resistance measurement of a 10 cm long sample, varying the distance between the two signal collecting probes using a 4-probe set-up. The results are plotted in Figure 4.6 and reveal a linear relationship between resistance and position of the contact, suggesting a uniform electrical conductivity, hence distribution of CNTs, of the composite along the fiber length.

In Figure 4.7, we show the stress-strain curves of the 6% CNT/34% HDPE/60% SEBS composite, together with the curves of 34% HDPE/60% SEBS and pure HDPE for comparison. HDPE exhibits a typical stress-strain feature of thermoplastics, with Young's modulus of 980.6 MPa, yield strength of 28.9 MPa, and average elongation at break of 395%. The introduction of HDPE significantly strengthened SEBS, resulting in a much higher values of modulus, fracture strain and stress as well as a reduced elastic limit. The addition of small amount of CNTs further enhanced the tensile strength and Young's modulus, suggesting the good dispersion of the CNTs and an efficient stress transfer from the matrix to the CNT networks via good interfacial interaction.<sup>147</sup>

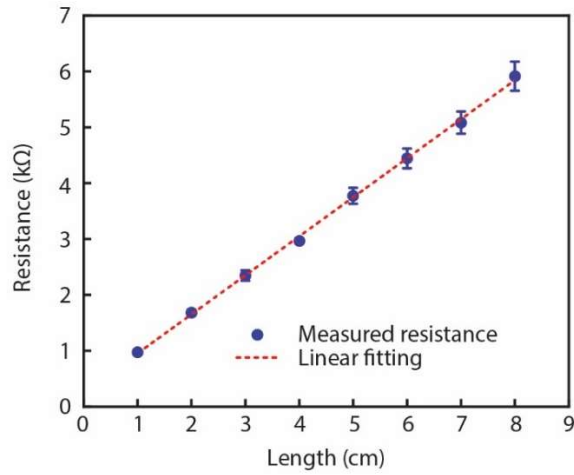


**Figure 4.6** Measurement of the resistance versus length showing their linear relationship results from the overall homogeneous distribution of CNTs.

To achieve high performance for triboelectric devices, there are two major parameters that we need to consider for the materials selection and engineering: surface features and triboelectric polarity. Since the surface features could be modified using micro/nanoengineering techniques, the triboelectric polarity is the most important inherent parameter that determines the final output performance. We therefore analyzed the triboelectric response of some materials by measuring the short circuit currents of TENG devices assembled with these materials. The detailed information about the measurement setup and assembled devices have been illustrated in Chapter 3. We characterized the relative triboelectric polarities of a few alternative materials and they could be classified as follows:

(+) SEBS > 6% CNT/94% SEBS > HDPE > 6% CNT/34% HDPE/60% SEBS (-)

From this list, we can find that the addition of HDPE to the composite tends to make the material more negative. Therefore, we prefer to take the composite 6% CNT/34% HDPE/60% SEBS as both the electrode material and one of the two triboelectric surface to generate triboelectric charges. Another triboelectric surface is SEBS.

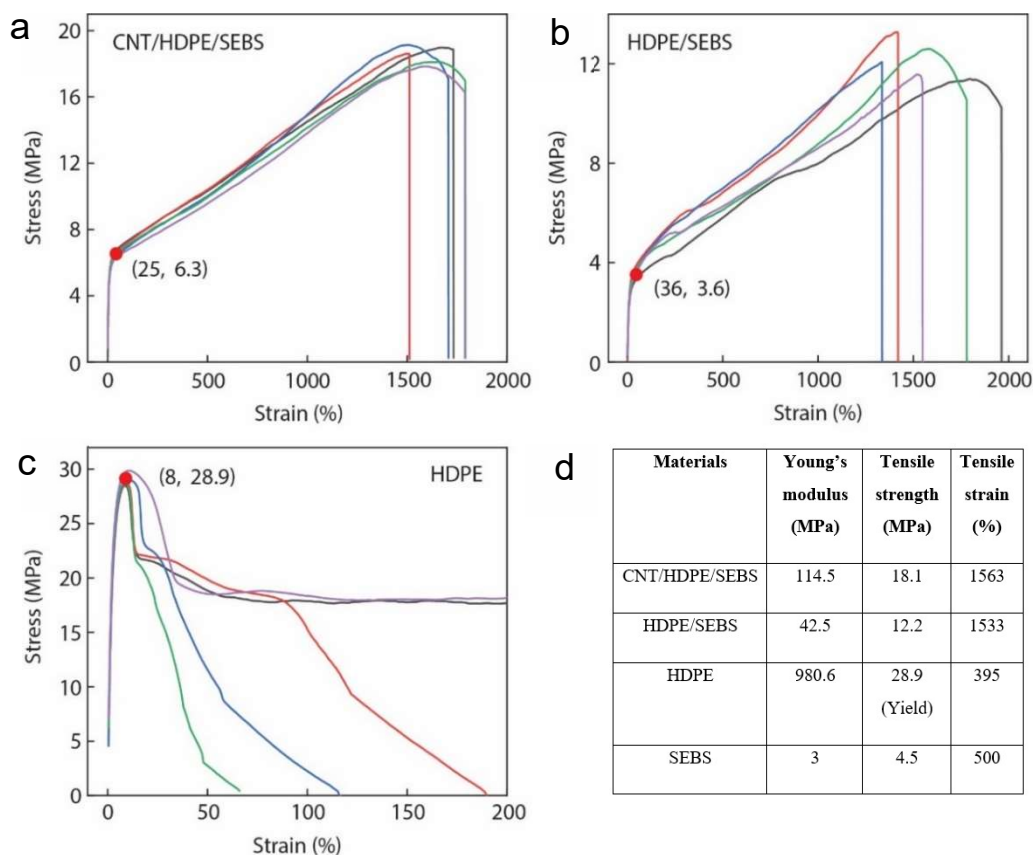


**Figure 4.7** Stress-strain curves of CNT/HDPE/SEBS (a), HDPE/SEBS (b), and HDPE (c). The red dots in the curves indicate the elastic limit of the materials. Five samples were used for each type of material. (d) A table summarize Young's modulus, tensile strength and strain of these materials. The data for SEBS is from literature.<sup>48</sup>

### 4.3 Fiber microstructure engineering, processing and characterization

After identifying the device architecture, and the proper encapsulating and electrically conducting materials, we now turn to the fabrication procedure of the targeted fibers. Figure 4.8a schematically shows the fabrication approach that we used to produce such complex multi-material fibers from a macroscopic preform. In figures 4.8b and c, we show clearly the detailed structures and preparation steps of the preforms. Overall, the asymmetric structure is composed of two different triboelectric parts separated by an air gap. Both of the triboelectric parts include a layer of stretchable CNT/HDPE/SEBS composite, and the only difference is that one part has an extra top layer of SEBS layer. We also

integrated a liquid metal channel on the back of the composites, for the purpose of achieving a good electrical conductivity, which is particularly important to reduce energy loss along the fiber axis.

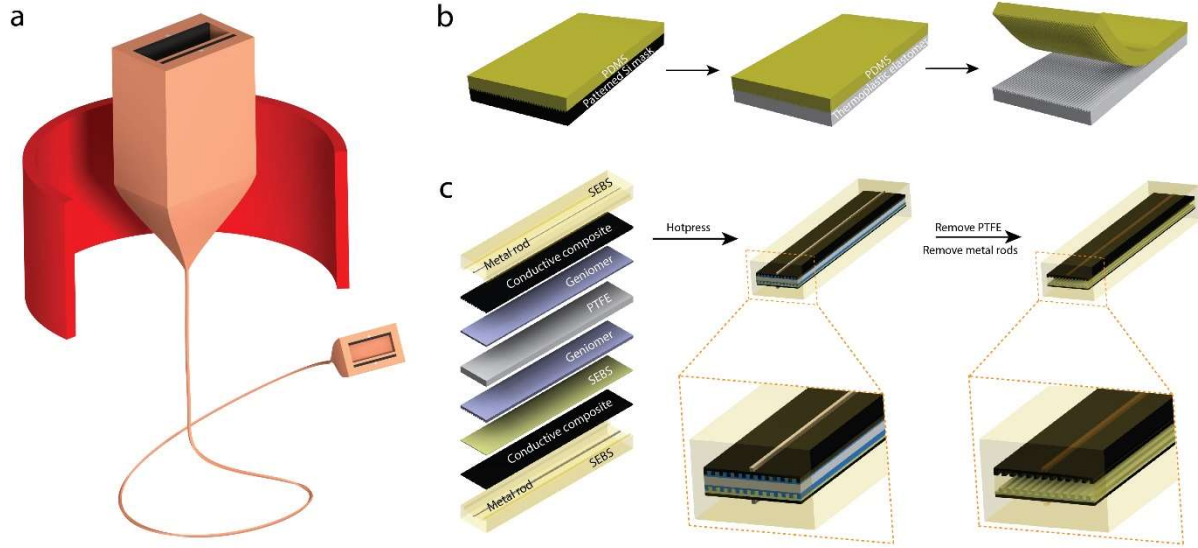


**Figure 4.8** Structural design and fabrication of the stretchable, self-encapsulated fiber power system. (a) Schematic showing the thermal processing of a multi-material preform into long fibers. (b) The preparation procedures of micro-textured thermoplastic elastomers from a patterned mask. (c) Schematic showing the detailed structure and fabrication of the preform. The zoom-in illustration highlights the micro-textured triboelectric surfaces.

The amount of charges on polymer surfaces induced by the contact-electrification effect largely depends on the surface area of the materials. Therefore, microstructure engineering of the triboelectric surfaces for a larger surface area is important for higher output performance of TENG devices. As schematically shown in Figure 4.8, we can exploit the unique versatility of the thermal drawing process to integrate surface micro-texture. Fabricated first at the preform level, we must be careful of the reflow mechanism driven by surface tension during the drawing process that can cause the distortion or even collapse of the textures in the resulting fibers.<sup>20,105</sup> In general, thermoplastic materials with high mechanical strength, for example polyetherimide (~127 MPa), can be processed at high viscosity to reduce reflow. However, this strategy is not applicable for thermoplastic elastomers because they have a very low mechanical strength of only several MPa, and hence can be drawn at relatively low viscosity. In Figure 4.9 we show SEM images of a fiber produced from a preform with surface textures of 100  $\mu\text{m}$ . It is clear that the micro-textures have almost disappeared. Therefore, we must introduce a sacrificial

material to form an intimate contact with the textured polymer in the preform, which will enable a significant reduction of the interfacial tension and thus lower the driving force behind the reflow.<sup>20,48</sup>

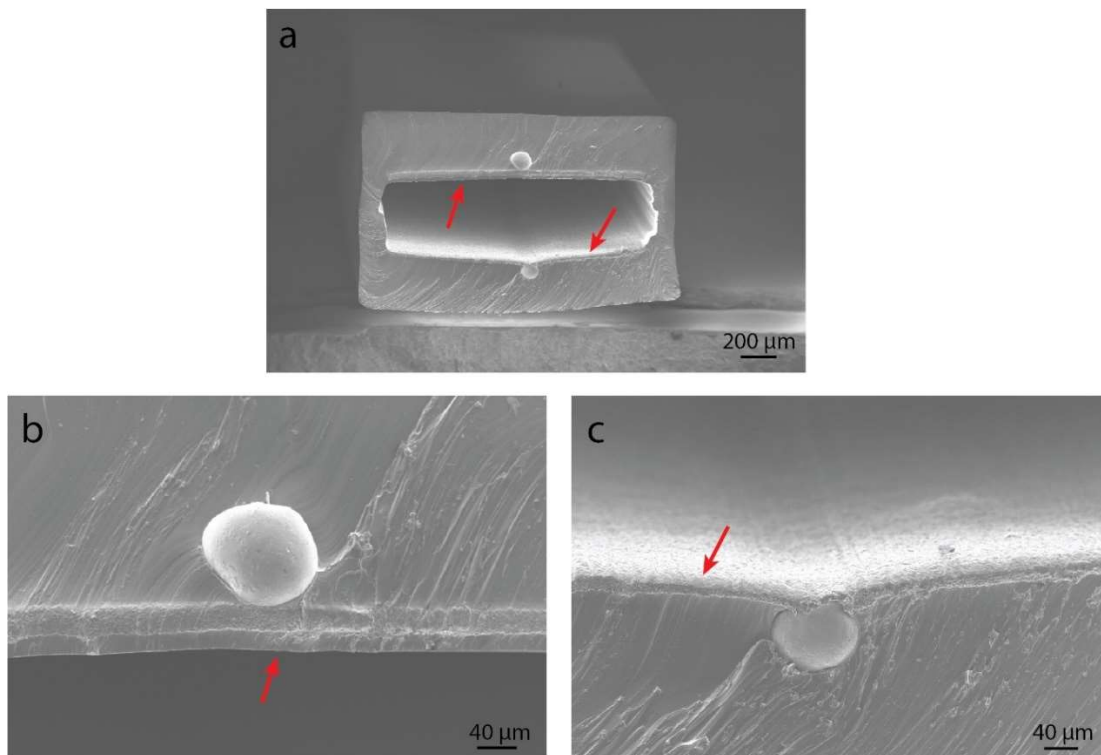


**Figure 4.9** SEM images of fibers drawn from a surface-textured preform: (a) overall structure, (b) magnification of the top part, (c) magnification of the bottom part. Red arrows indicate the surfaces that were textured at the preform level.

**Table 4.1** Surface tensions of the test liquids.

Solvent	Polar component (mN/m)	Dispersive component (mN/m)	Total surface tension (mN/m)	Contact angle with SEBS	Contact angle with CNT/HDPE/SEBS	Contact angle with Geniomer
Ethyl acetate	0	23.9	23.9	16.3±4.6	34.6±2.8	None
Ethylene glycol	16	32.8	48.8	78.6±1.6	83.2±3.3	95.6±2.2
water	46.4	26.4	72.8	103.9±1.5	None	110.9±0.2
ethanol	2.6	18.8	21.4	None	33.0±1.2	66.8±2.6

According to the established theories, the sacrificial material must fulfil the following requirements:

- It should exhibit a proper rheological behaviour so that it is co-drawable with the other selected materials.
- It should have a low interfacial tension with the contacted material to achieve the goal of reducing thermal reflow.
- In order to be removed easily after drawing, it should have a low adhesion energy with the contacting material so that it can be mechanically removed or alternatively there is a solvent for its selective etching.

For the selected materials of SEBS and the CNT/SEBS/HDPE composite, Geniomer was found to be an ideal candidate material that satisfies all the above requirements. Its rheological properties have been discussed in Chapter 3.1 and its processing temperature matches well with that of the other two materials. In addition, Geniomer is immiscible with both SEBS and the CNT/SEBS/HDPE composite, while the shear strength of the interface between the materials is strong enough to be co-drawn and low enough so that Geniomer can be mechanically removed after drawing.

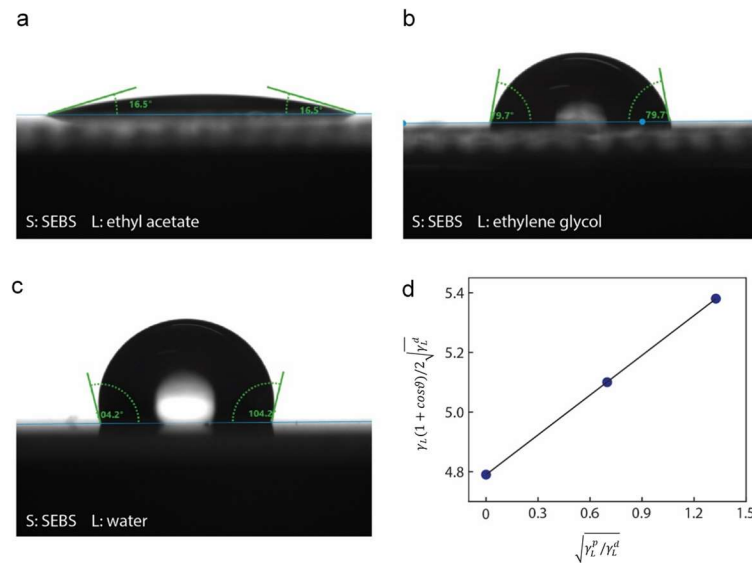


**Figure 4.10** Contact angle of SEBS with the test liquids (a-c) and a surface energy (polar and dispersive) calculation graph based on OWRK model (d).

Next, we will discuss the evaluation of interfacial tension of the associated elastomers. One common approach is to decompose the surface tension  $\gamma$  of a component into dispersive  $\gamma^d$  and polar  $\gamma^p$  interactions. The dispersive component originates from random fluctuations in the electron density, leading to an induced dipole-dipole interaction (van der Waals interaction). The polar component comprises Coulomb interactions between permanent dipoles and between permanent and induced dipoles (e.g. hydrogen bonds). The interfacial tension between two solid phases can be estimated by:<sup>148</sup>

$$\gamma_{12} = \gamma_1 + \gamma_2 - 4 \frac{\gamma_1^d \gamma_2^d}{\gamma_1^d + \gamma_2^d} - 4 \frac{\gamma_1^p \gamma_2^p}{\gamma_1^p + \gamma_2^p} \quad (4.2)$$

The analysis of the ratio between the dispersive and polar parts of the surface tension for two phases allows for a direct prediction of the adhesion between them. A higher match of the ratios means more possible interactions between the two phases, and thus a higher adhesion is expected. A high potential for interaction between two phases also leads to a small interfacial tension.

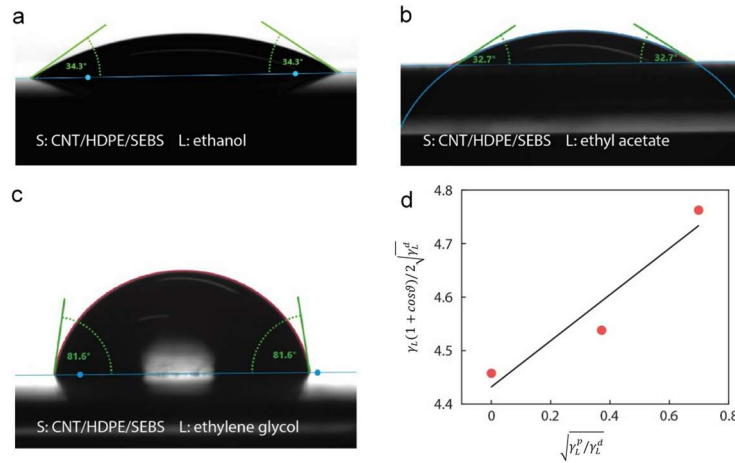


**Figure 4.11** Contact angle measurements of CNT/HDPE/SEBS.



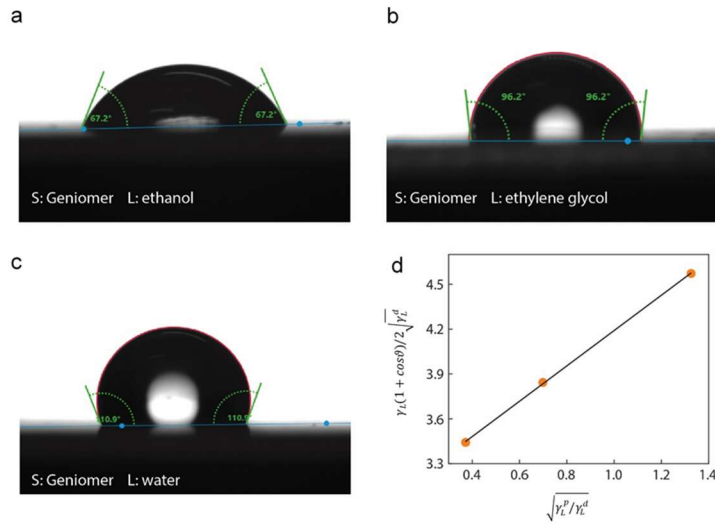


**Figure 4.12** Contact angle measurements of Geniomer.

**Table 4.2** Surface/interfacial tensions of SEBS and Geniomers at room temperature.

Materials	Polar component (mN/m)	Dispersive component (mN/m)	Total surface tension (mN/m)
SEBS	0.20	22.94	23.14
CNT/HDPE/SEBS	0.19	19.64	19.83
Geniomer	1.40	9.05	10.45
<b>Interfacial tension:</b> 6.94 (SEBS & Geniomer), 4.83 (CNT/HDPE/SEBS & Geniomer)			

To determine the surface tension of a solid, a common method is to measure the contact angles of several liquids whose surface tensions including their dispersive and polar parts are known. These dispersive and polar components can be used to calculate the interfacial tension between the solid and the liquid using the OWRK model:

$$\gamma_{SL} = \gamma_S + \gamma_L - 2\sqrt{\gamma_S^d \gamma_L^d} - 2\sqrt{\gamma_S^p \gamma_L^p} \quad (4.3)$$

Substituting this equation in the Young equation, the following expression can be deduced:

$$\frac{\gamma_L(1+\cos\theta)}{2\sqrt{\gamma_L^d}} = \sqrt{\gamma_S^p} \cdot \sqrt{\frac{\gamma_L^p}{\gamma_L^d}} + \sqrt{\gamma_S^d} \quad (4.4)$$

Hence, the  $\gamma_S^p$  and  $\gamma_S^d$  can be evaluated by extracting the slope and intercept of a regression line describing the relationship between  $\frac{\gamma_L(1+\cos\theta)}{2\sqrt{\gamma_L^d}}$  and  $\sqrt{\frac{\gamma_L^p}{\gamma_L^d}}$ , when contact angles of at least two test liquids are measured. The surface tension information of the test liquids is listed in Table 4.1.

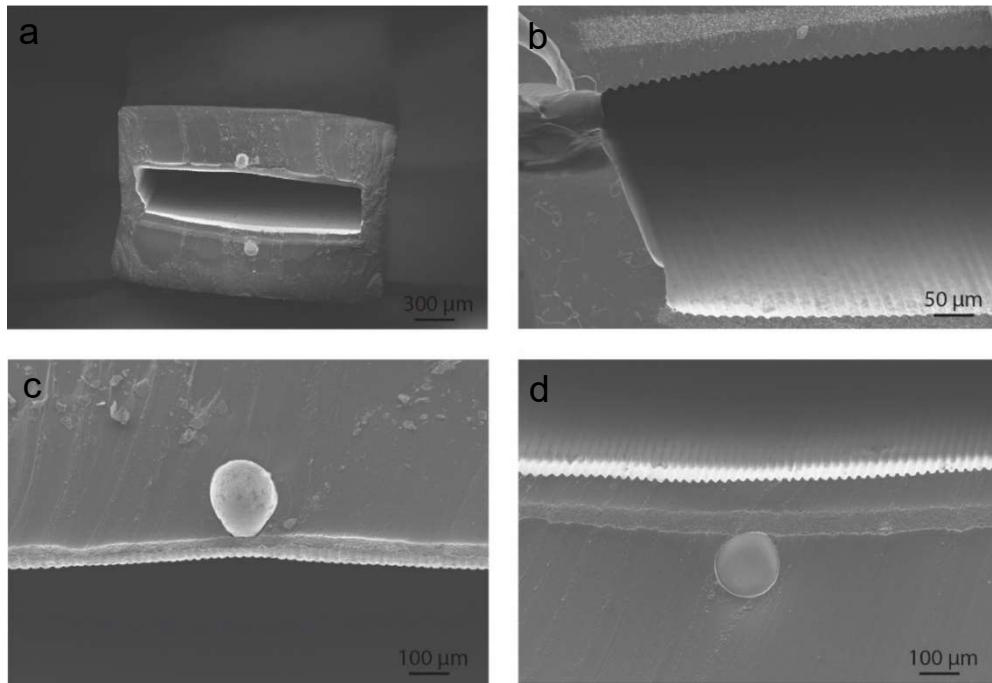


**Figure 4.13** SEM images of a fiber drawn from a micro-textured preform with extra sacrificial Geniomer layers.

Figures 4.10 – 4.12 show the measured contact angles of different liquids (Table 4.1) on clean SEBS, CNT/HDPE/SEBS and Geniomer films as well as the surface energy plots fitted using OWRK model. The model fits very well with our results. In Table 4.2 we summarize the extracted surface energy values. The interfacial tension between SEBS and Geniomer is much lower than the surface energy of SEBS at room temperature, which occurs to CNT/HDPE/SEBS and Geniomer also. In general, surface tension decreases when temperature increases because the cohesive forces decrease with an increase of

molecular thermal activity at higher temperature. For polymers, the  $dy/dT$  is independent of temperature, generally in the range from  $-0.05$  to  $-0.08 \text{ mN m}^{-1} \text{ deg}^{-1}$ . The interfacial tension varies more slowly with temperature than surface tensions, which is usually smaller than  $0.03 \text{ mN m}^{-1} \text{ deg}^{-1}$ .<sup>149,150</sup> Therefore, we deduced that the interfacial tension between SEBS and Geniomer at  $160^\circ\text{C}$  is around  $2.89 \text{ mN m}^{-1} \text{ deg}^{-1}$ , still much smaller than the surface tension of SEBS, which is in the range between  $12.3$  and  $16.35 \text{ mN m}^{-1} \text{ deg}^{-1}$ . Similarly, the interfacial tension between CNT/HDPE/SEBS and Geniomer at higher temperature is also much smaller than the surface tension of CNT/HDPE/SEBS. The analysis indicates the potential of Geniomer as a suitable sacrificial layer in our fiber design. Guided by the above analysis, fibers with extended length were obtained. In Figure 4.13, we show the structure of the fibers after the removal of Geniomer film. Comparing with the results in Figure 4.9, we can find that the lower interfacial tension significantly reduced thermal reflow, preserving the targeted texture.

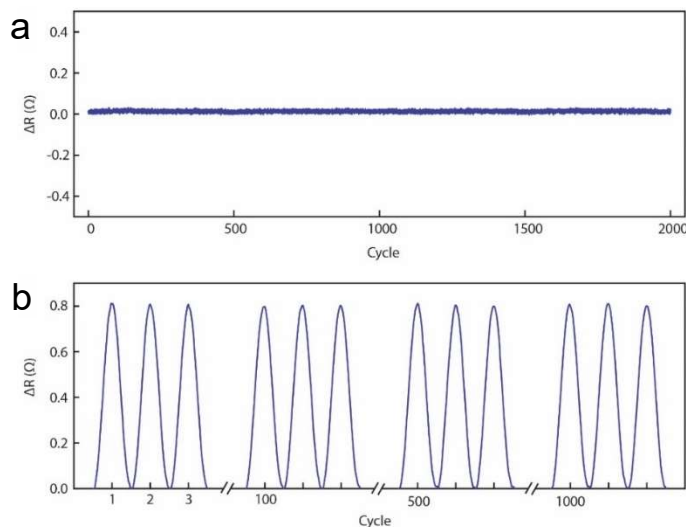


**Figure 4.14** (a) Resistance of the composite under repeated compression and relaxation for 2000 cycles. (b) Resistance of the composite under repeated stretching and relaxation for 1000 cycles. Only the data starting at cycle 1, 100, and 1000 are shown.

Since the fiber is designed to work under large deformations, we therefore subjected it to repeated cycles of controlled compression (20 N) and relaxation while simultaneously measuring the resistance of the electrodes. The resistance did not show any change with such a dynamic deformation over 2000 cycles (Figure 4.14a). Similarly, we also performed same measurement under repeated 40% strain and

relaxation, and the resistive response to such a deformation is quite stable throughout 1000 cycles (Figure 4.14b). Although the resistance increases a bit with elongation, it is acceptable and will not impact negatively on the output performance, as we will show. Indeed, the high impedance of TENG devices allows to accommodate for variation of the electrodes resistance to some extent, without performance degradation.

## 4.4 Methods

Before we summarize the achievements in this chapter, we describe in more details the methodology we have used for the various fabrication and characterization experiment described:

The conductive composite was fabricated with a micro-extruder with twin conical screws. To obtain the 6% CNT/34% HDPE/60% SEBS composite, 0.8 g 15%CNT/85%HDPE granules and 1.2 g SEBS granules were fed into the extruder for each mixing. The extruding temperature was set at 240 °C, and the rotation speed was 100 rpm. The materials were mixed for 5 min in the extruder before extracted as a filament. Similarly, the HDPE/SEBS composite was extruded with pure HDPE and SEBS granules at 200 °C.

All the preforms used in this chapter have a rectangular shape with a length of 170 mm, a width of 24 mm and a varied height depending on the elements in the preform. First, granules of the polymers were hot-pressed (Lauffer Pressen UVL 5.0 or Maschinenfabrik Herbert Meyer GmbH APV-2525/16) into geometrically defined plates. Then, the different polymer parts were assembled into a preform, where machined PTFE plates with 20 mm in width and 3 mm in total were placed at the center to create the hollow channel and two metal rods with the diameter of 1.5 mm was placed next to the composite parts to make empty channels. The preform was consolidated in the hot press at 140 °C for 10 min and the PTFE and metal rods were subsequently mechanically removed. Finally, the preforms were drawn into long fibers with a custom draw tower at 215 °C. The feeding speed was set as 0.6 mm/min, and the draw speed as 0.1 m/min. In order to make the fibers with micro-textures on the two inner triboelectric surfaces, a pre-textured PDMS mold was used as the template to imprint its patterns onto CNT/HDPE/SEBS composite and Geniomer films. It was completed by hot pressing at 140 °C for 5 min.

The sessile drop contact angle measurement was performed through a Drop Shape Analyzer. Tested polymer films were carefully cleaned before the tests because contact angles are extremely sensitive to

contamination. At least five drops were analyzed for each liquid to obtain an average contact angle value. Water vapor transmission rate of SEBS was tested with a water vapor permeation analyzer at the relative humidity of 50%. Measurements at different temperatures from 15 to 45 °C were carried out to extract the activation energy of water vapor permeation for SEBS. The triboelectric polarity of the materials was determined from the electrical outputs of a series of self-constructed contact-mode 2D TENG devices with the selected polymer films as the dielectric surfaces.

Scanning electron microscopy (SEM) was performed on a Zeiss Merlin field emission SEM with an acceleration voltage of 3 kV or 4 kV using the In-Lens detector and Analytic Column Mode. The fiber samples for SEM characterizations were prepared by immersing them into liquid nitrogen for one minute followed by an immediate cutting at room temperature. The fiber and the CNT/HDPE/SEBS samples were coated with 10 nm and 5 nm Au film respectively before characterization. The mechanical tensile tests were conducted on a universal testing machine (UTS) Series LFM-125 kN (*Walter+Bai AG*) with the tensile mode (1 kN load cell). The displacement was set to 1 mm min<sup>-1</sup>. Five tests were recorded for each material. The calculation of Young's modulus from the stress-strain curves is limited to the very low strain region of less than 3% strain. The resistance of CNT/HDPE/SEBS composite was measured with an electrical testing instrument (Keithley Sourcemeter 2450) in four-probe mode at a current of 1 mA.

## 4.5 Summary

In this chapter, we demonstrated the design and fabrication of a self-encapsulated and stretchable fiber, for triboelectric energy harvesting. First, we identified SEBS as the proper encapsulating material due to its high elasticity, good adhesion with other polymers, and good compatibility with fiber drawing technique. We then analyzed its contact angle with DI water and water vapor transmission rate at different temperatures, suggesting its hydrophobicity, much lower water vapor transmission rate than PDMS, as well as higher activation energy of permeation than common polymers. The analysis confirmed that SEBS is a good encapsulating material for stretchable devices, in particular those that are sensitive to the change of ambient environment. Since the output performance is highly dependent on relative humidity, the self-encapsulated structure with a water resistant cladding enables its efficient function even at high humidity conditions. Then, we identified a CNT/HDPE/SEBS composite as the main electrode material for the fiber scheme. The homogeneous dispersion of CNT in the polymeric

matrix was confirmed by SEM and electrical resistance test. The enhanced mechanical properties of the composite than the matrix also suggests the good distribution of CNTs and thus the efficient stress transfer from the matrix to CNTs.

Given their triboelectric polarity and mechanical properties, SEBS and the CNT-based composite were selected as the two triboelectric layers for the proposed contact-mode triboelectric fibers. To enhance the output performance of the device, we created micro-textures on the triboelectric surfaces and covered the structured polymer with a sacrificial Geniomer layer in order to drastically reduce the interfacial tension that drives the thermal reflow during drawing. The surface/interfacial tensions of the associated polymers were evaluated with contact angle analysis and the OWRK model. Guided by the above analysis, a self-encapsulated triboelectric fiber that gathers multiple stretchable materials, microstructural features and an empty gap was fabricated. The mechanical behavior and the electrical output performance of the resulting fibers will be discussed in the following chapter.

## **Chapter 5 Electrical and mechanical properties of contact-separation mode soft triboelectric fibers**

After the discussion about the architectural design, materials characterization and fabrication of the stretchable multi-material fibers, in this chapter we concentrate on the characterization of the fibers' electrical output performance and the understanding of their mechanical response that triggers these electrical signals. First, we schematically illustrate the working mechanism of the resulting fibers as conductor-to-dielectric mode TENG devices, specifically the charge generation and transfer process induced by repeated compressive loading and release. Afterwards, the electric potential distribution of the fiber system is revealed via the finite element simulation of a simplified 2D model. The open-circuit voltage between the two electrodes with respect to the distance between the two tribosurfaces is also extracted. Unlike the common dielectric-to-dielectric contact-mode TENGs, one of the two conductive composites work as both the triboelectric material and the electrode in the conductor-to-dielectric TENGs. The amount of transferred charge as a function of the relative movement of the two triboelectric parts in this case is therefore extracted in order to better understand the work principal and thus guide the cross-sectional architectural design of the fibers. Next, we compare the output performance of the obtained fibers with and without inner surface micro-textures, triggered by the same periodic vertical compression force at various frequencies. In addition to the study of the output power as a function of the loaded resistance, the endurance of the fiber to long-term mechanical compression as well as water infiltration is also evaluated to show the robustness and reliability of the fiber system working in harsh environments. Moreover, the impact of compressive pressure to the fiber's output performance will be presented, and the finite element analysis (FEA) of the mechanical response to external forces will be discussed in detail. The superior deformability of the resulting fibers potentially allows the electricity generation from different forms of mechanical stimuli without any structural failure. Taking stretching as an example, we will present the fiber's cross-sectional deformation, the FEA of the electric potential distribution as well as the experimental characterization of the electrical outputs under tensile strain.

## 5.1 Electrical output performance under compression

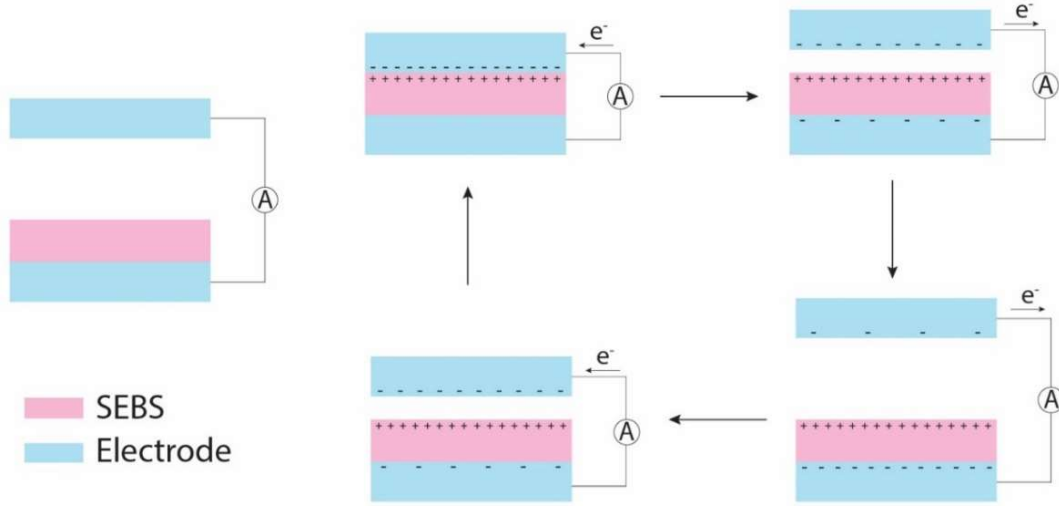


**Figure 5.1** Schematic illustration of the charge generation and short-circuit charge transfer process of the proposed contact-mode fiber TENG system under repeated external compression force. For simplicity, the charges are assumed to be uniformly distributed on the surfaces/interfaces of the materials.

We start by discussing the potential of stretchable multi-material fibers working as contact-mode TENG devices. Unlike the common dielectric-to-dielectric contact-mode devices, this fiber works in the conductor-to-dielectric mode, where the single conductive material function as both the triboelectric layer and the electrode. In Figure 5.1, we schematically show the main components and structure of the proposed triboelectric fiber, together with its working mechanism to generate electricity. The cladding and liquid metal are ignored in this schematic for simplicity. Specifically, we show in detail the charge generation and transfer process of the system under short circuit condition, triggered by repeated compressive excitation. As the two triboelectric layers are brought into contact, electrons will be injected from SEBS to the composite electrode due to the contact electrification effect. It will result in positive charges generated on the SEBS surface, and a similar amount of negative charges on the composite. As the composite moves away from the SEBS, it is exposed to a negative electrostatic field, and therefore electrons will flow from it to the bottom electrode under short-circuit condition. The open-circuit voltage and short-circuit transferred charges between the two composites will reach their maximum values when the upper composite stops moving. Similarly, as it moves back to contact again, a reversed electric field



change is induced, which will lead to a reversed charge flow. An alternating current is hence formed at working cycle.

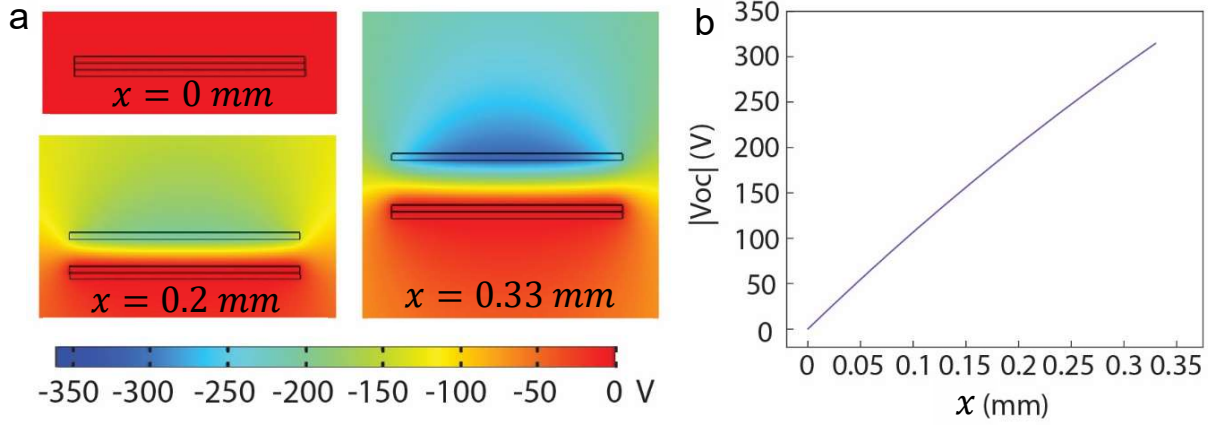


**Figure 5.2** Numerical calculations of the potential distributions of the fiber at different distance  $d$  between the two triboelectric surfaces. The maximum value of  $x$  is set 0.33 mm based upon the fiber's dimension without any external mechanical stimuli: (a) images showing the status when  $x$  is 0, 0.2 and 0.33mm respectively. (b) calculated open-circuit voltage between the two electrodes as a function of  $x$ .

For a better understanding of this working mechanism, the electric potential distribution of the fiber system was simulated via finite element simulation using the electrostatics module in COMSOL Multiphysics. To simplify the computation, a 2D finite element model was built based upon the real structures and dimensions of our fibers. The composites and SEBS have the same values of the width (1.7 mm) and thickness (0.05 mm). The positions of SEBS film and its electrode are fixed and the top electrode is movable along the vertical direction under external mechanical force. The distance between the two triboelectric surfaces, defined as  $x$ , has a maximum value of 0.33mm. The material properties were assigned in the software: the relative permittivity of SEBS is 2.45 (at frequencies between  $10^{-2}$  to  $10^6$  Hz)<sup>151</sup> and we assumed that the fiber system is in air with a set relative permittivity of 1. The SEBS film was set to carry net positive charges with a charge density of  $10 \mu\text{C m}^{-2}$  on its surface, due to the contact-electrification effect. Considering the excellent insulating properties of the elastomer, it is reasonable to assume that the charges are uniformly distributed on the surface. Meanwhile, there are equal amount of negative charges injected to the upper electrode. For simplicity, the potential of the bottom electrode was set to zero. With this model, the electric potential distribution in the open circuit condition (no electric charge transfer between the electrodes) with varied separation distance  $x$  was computed. As shown in the Figure 5.2a, due to the electrostatic induction effect, the electric potential at the upper electrode is negative, providing the driving force for current flow between the two electrodes once a circuit is built. To further quantitatively understand the electrical output

characteristics of the fiber device, the relationship between  $V_{oc}$  and  $x$  was investigated. As shown in the Figure 5.2b, the  $|V_{oc}|$  increases linearly with  $x$ , which is attributed to the capacitive behaviour of the system.

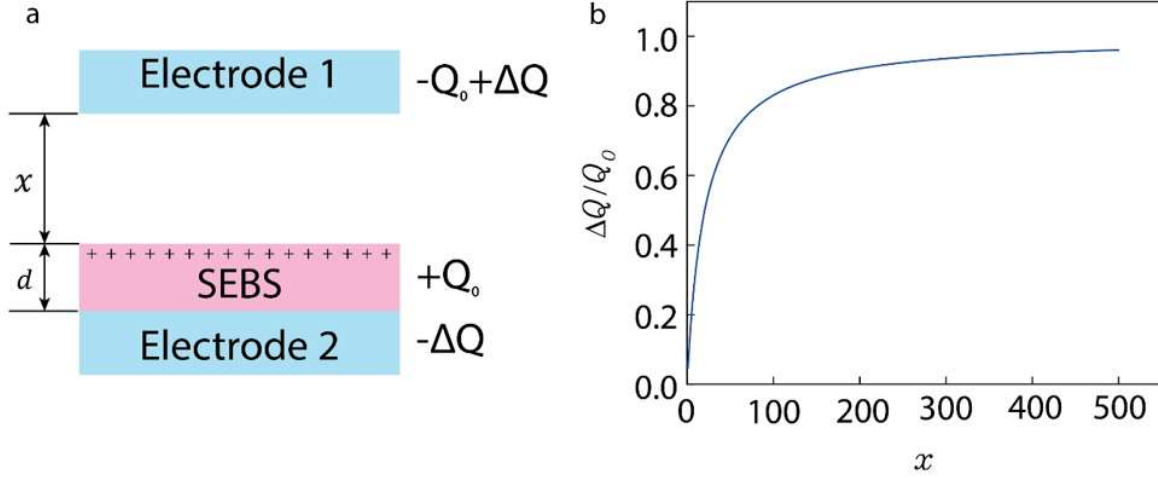


**Figure 5.3** (a) Schematic showing the theoretical model for conductor-to-dielectric contact-mode TENGs, where the two electrodes are electrically connected. (b) Extracted relationship between the amount of transferred charges and distance between the two triboelectric parts.

Figure 5.3a shows the theoretical model for the conductor-to-dielectric contact-mode TENGs. The thickness and dielectric constant of SEBS are defined as  $d$  and  $\epsilon_r$  respectively. The distance between the two triboelectric parts  $x(t)$  can be varied under the repeated compression force.  $Q$  represents the tribo charges due to triboelectricity and  $\Delta Q$  means the amount of transferred charges between the two electrodes once they are short-circuited. Since it plays the role of as both the triboelectric layer and electrode, the total amount of charges in Electrode 1 is  $-Q_0 + \Delta Q$ . We assume that the two electrodes are infinitely large in this model. From the Gauss theorem, the voltage drop  $\Delta V$  from Electrode 2 to 1 is:

$$\Delta V = \left( \frac{Q_0 - \Delta Q}{2\epsilon_0} + \frac{Q_0}{2\epsilon_0} - \frac{\Delta Q}{2\epsilon_0} \right) x(t) + \left( \frac{Q_0 - \Delta Q}{2\epsilon_0 \epsilon_r} - \frac{Q_0}{2\epsilon_0 \epsilon_r} - \frac{\Delta Q}{2\epsilon_0 \epsilon_r} \right) d = \frac{Q_0 - \Delta Q}{\epsilon_0} x(t) - \frac{\Delta Q}{\epsilon_0 \epsilon_r} d \quad (5.1)$$

As the charge transfer reaches equilibrium, namely  $\Delta V = 0$ , then we can get:

$$\frac{\Delta Q}{Q_0} = \frac{\epsilon_r x(t)}{\epsilon_r x(t) + d} \quad (5.2)$$

In our fiber power system,  $\epsilon_r$  of SEBS is  $2.45^{151}$  and  $d$  is about  $50 \mu\text{m}$ . Thus, the relationship between  $\Delta Q/Q_0$  and  $x(t)$  can be extracted and is displayed in Figure 5.3b. The amount of transferred charges increases sharply with the increased distance thanks to the relatively large dielectric constant of SEBS (the slop for  $x(t) = 0$  equals  $\epsilon_r/d$ ), but the derivative tends to reduce as the distance is larger than  $200 \mu\text{m}$ . In our fiber structure, the gap between the two triboelectric parts was designed to be larger than  $300 \mu\text{m}$  to guarantee that more than 90% of the tribo charges can be transferred between the two electrodes and thus produces high electrical outputs.

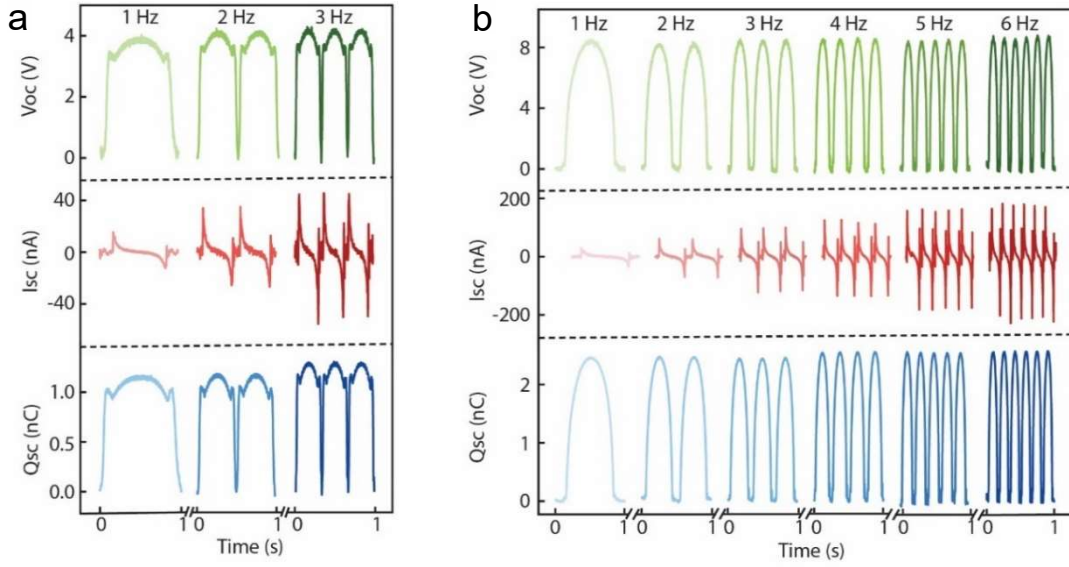


**Figure 5.4** The measured typical electrical responses including open-circuit voltage, short-circuit current and short-circuit transferred charge of fibers under pressing: (a) a fiber with smooth triboelectric surfaces, (b) a fiber with micro-textured triboelectric surfaces. The signals under different frequencies were recorded. The fiber in (a) is 2.1 mm in width and 1.3 mm in thickness, while the fiber in (b) is 2.3 mm in width and 1.4 mm in thickness. The effective lengths for both samples are the same: 3 cm.

In order to quantitatively evaluate the energy harvesting performance of the fibers, we first characterized their outputs triggered by a cyclic vertical compressive force, driven by a custom made DC motor. In Figure 5.4, we show typical outputs of short fibers (contact length: 3 cm) with smooth (Figure 5.4a) and micro-textured (Figure 5.4b) triboelectric surfaces under various compression frequencies. By comparison, we can find that all the output signals of the microtextured fiber are about two times of the one with smooth surfaces, indicating the enhancing effect of microstructured surfaces

on the performance. Compared with other reported triboelectric fiber-based TENG devices listed in Table 3.1, the outputs ( $\sim 8.5$  V,  $88.0$  V/cm<sup>3</sup>,  $2.5$  nC,  $25.9$  nC/cm<sup>3</sup>,  $218$  nA,  $2.3$   $\mu$ C/cm<sup>3</sup>) approaches state-of-the-art.

For both fibers, while the open-circuit voltage ( $V_{oc}$ ) and short-circuit transferred charge ( $Q_{sc}$ ) remain almost constant, the peak values of short-circuit current ( $I_{sc}$ ) keeps an increasing trend with the increased frequencies. As shown in Figure 5.5, both the extracted values of  $I_{sc}$  upon the pressing and releasing show a standard linear relationship with frequency. This can be explained with our abovementioned theoretical model. For Equation 5.1, when the device is at an open-circuit condition, there is no charge transfer between the two electrodes, i.e.  $\Delta Q = 0$ . Therefore, based on Equation 5.1, the  $V_{oc}$  is calculated as:

$$V_{oc} = \frac{Q_0 x(t)}{\epsilon_0} \quad (5.3)$$

At the short-circuit condition, the potential difference between the two electrodes is 0, i.e.  $\Delta V = 0$ . We can thus get  $Q_{sc}$  and  $I_{sc}$ :

$$Q_{sc} = \frac{\epsilon_r x(t)}{\epsilon_r x(t) + d} Q_0 \quad (5.4)$$

$$I_{sc} = \frac{dQ_{sc}}{dt} = \frac{d}{dt} \left( \frac{\epsilon_r x(t)}{\epsilon_r x(t) + d} Q_0 \right) = \frac{\epsilon_r d Q_0}{(\epsilon_r x(t) + d)^2} \frac{dx(t)}{dt} = \frac{\epsilon_r d Q_0 v(t)}{(\epsilon_r x(t) + d)^2} \quad (5.5)$$

where  $v(t)$  is the moving velocity of the upper triboelectric part. From Equations 5.3-5.5, we can conclude that  $V_{oc}$ ,  $Q_{sc}$  and  $I_{sc}$  are all proportional to triboelectric charges  $Q_0$ , a parameter that is mainly determined by the intrinsic triboelectric polarity of the triboelectric materials and their surface morphology. The value of  $d$  and maximum value of  $x(t)$  are constant for a certain fiber device, therefore  $V_{oc}$  and  $Q_{sc}$  remain unchanged, while  $I_{sc}$  is proportional to  $v(t)$ .

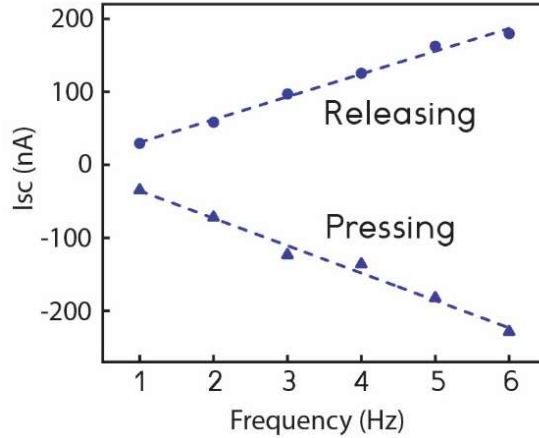


**Figure 5.5** Dependence of the current on the frequencies of the repeated compression and relaxation stimuli.

In addition to the frequencies of mechanical stimuli, we also studied the impact of compression pressure to the fiber's output performance. First, we measured the mechanical response of the fiber device under compression. As shown in Figure 5.6a, the pressure increases more sharply as the displacement reaches 350 – 400  $\mu\text{m}$ , which is due to the high stiffness of the structure as the two inner surfaces come into contact. The corresponding pressure is around 110 – 140 kPa. Afterwards, we recorded the output current signal under various compression pressures. The results are shown in Figure 5.6b and the pressure region of 110 – 140 kPa is highlighted with red color. We can see that the current increases linearly with the pressure before this contact region, while the increase tends to be slow and reaches a plateau under higher pressure. It indicates that once the two triboelectric surfaces are fully in contact, higher force will no longer contribute to the outputs. The linear relationship between the output current and pressure indicates another potential function of the fiber construct – a self-powered pressure sensor.

The output power of a TENG device to resistive loads depends on the impedance match between the power source and the loaded resistors. The output current and voltage of the fiber device when connected to various resistors are shown in Figure 5.6c, and the calculated output power and power density is shown in Figure 5.6d. By fitting the experimental data, we can find that the fiber reaches its maximum instantaneous output power density of 3  $\mu\text{W}/\text{m}$  at the load resistance of around 58  $\text{M}\Omega$ .

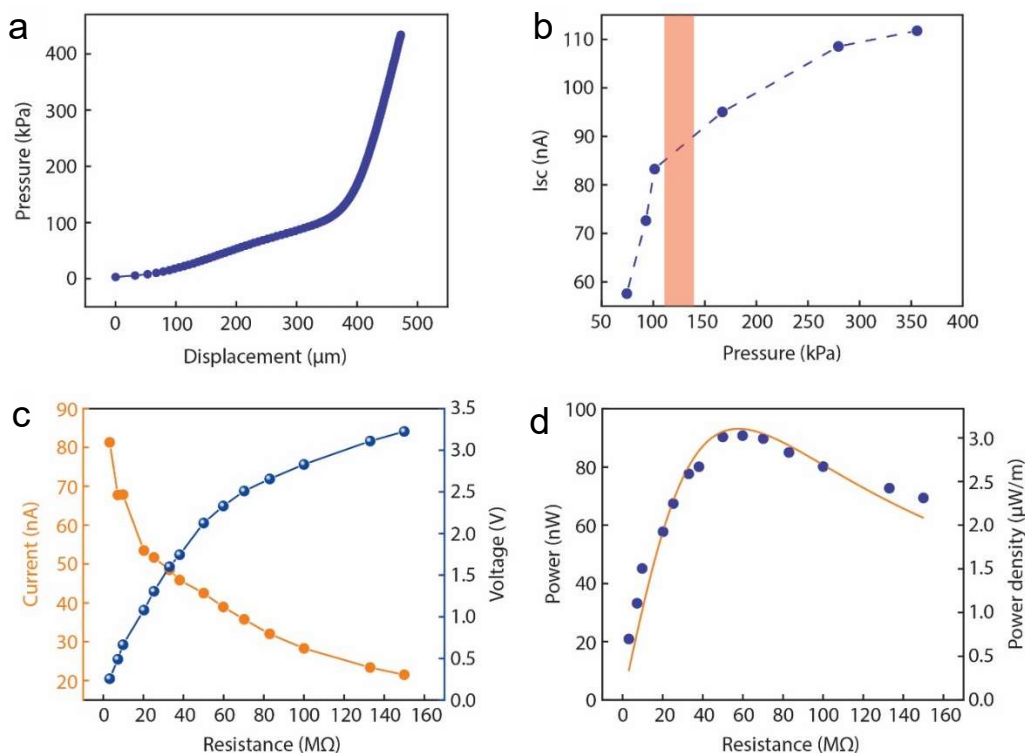


**Figure 5.6** (a) The compression pressure on the fiber structure as a function of displacement. (b) Dependence of the output current on the compressing pressure. (c) The output current and voltage as the fiber is connected to various resistors at the frequency of 3 Hz. (d) Calculated output power and power density from the data in (c). A fitting curve based on the theory of TENGs is also shown. The maximum average output power is obtained at the matched resistive load of  $\sim 58 \text{ M}\Omega$ .

To evaluate the endurance of the fiber when subjected to long-term mechanical deformation, we imposed repeated pression and relaxation stimulation at 2 Hz while simultaneously recording the current waveforms (Figure 5.7a). The magnitude of the current after 70 000 cycles still remains 93% of its initial value. As we have discussed in Chapter 4, we meticulously selected the stretchable and waterproof encapsulating material to guarantee the proper function of the fiber in water or high humidity conditions. To confirm this design, we immersed the fiber in water after sealing the cavity at its both extremities, and recorded the voltage output before and after immersion for a few days. The stable waveforms in Figure 5.7b indicate the good tolerance of the fiber construct to water infiltration.

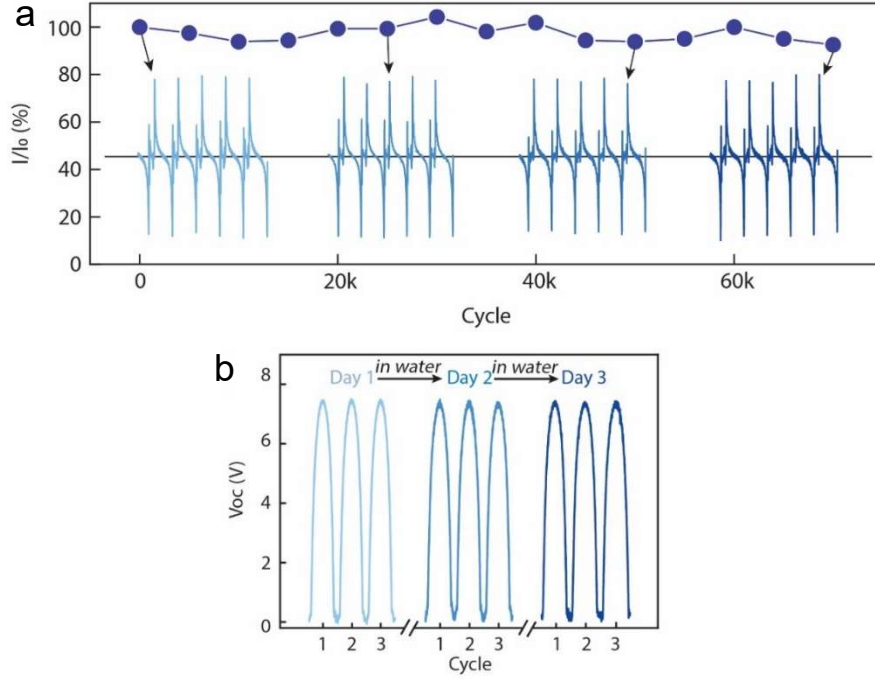


**Figure 5.7** (a) Long-term output stability tests under continuous pressing for 70 000 cycles. The current waveforms at the cycles of 1, 25 000, 50 000, and 70 000 are presented also. (b) comparison of the voltage output of the fiber before and after being immersed in water for 1 and 2 days. The fiber was tested directly without further drying after being taken out from water.

## 5.2 Finite element analysis of the mechanical deformation under compression

To further explore the compressive deformation that induces the electrical outputs, we performed finite element analysis (FEA) of the fiber structure using Abaqus/Explicit. Given the uniform features along the length, we simplified the geometry of the fiber structure to a plane stress (2D) model by only considering its cross-section. The efficiency and reliability of the simulation were further enhanced by building the geometry and dimensions of the fiber based on the sample's optical microscopy image (Figure 5.8). The two liquid metal channels were ignored in the model after we could confirm their negligible effect on the simulation results. The two side walls of the large hollow channel are set curved with a maximum deviation of 22.5  $\mu\text{m}$  at the outer surfaces. The imperfection on the inner surfaces of each side wall was simplified to two connected arc shapes.

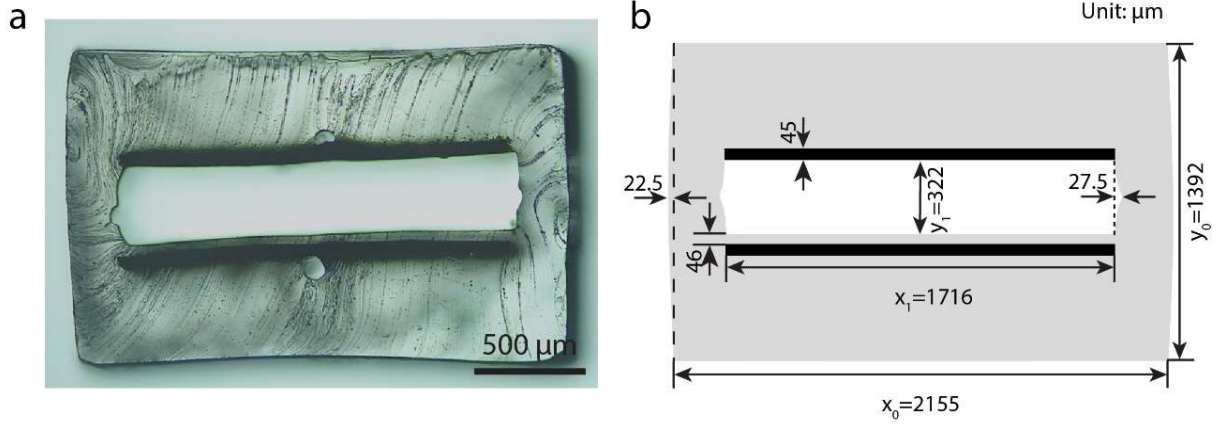


**Figure 5.8** Cross-sectional structure of the fiber: (a) measured by an optical microscope, (b) simplified in the FEA. The critical dimensions are indicated in the schematic. The symbols of  $x_1$ ,  $x_0$ ,  $y_1$ ,  $y_0$  represent the width and height of the open channel and the whole structure respectively, which will be used in the following discussions.

Considering the nonlinear mechanical behavior of SEBS and its large deformation in this work, it was modeled by using the isotropic incompressible Yeoh hyperelastic material with the strain energy potential  $U = C_1(I_1 - 3) + C_2(I_1 - 3)^2 + C_3(I_1 - 3)^3$ , where  $I_1 = \lambda_1^2 + \lambda_2^2 + \lambda_3^2$  is the first invariant of the right Cauchy-Green deformation tensor, and  $\lambda_1$ ,  $\lambda_2$ , and  $\lambda_3$  are principal stretches. The material constants  $C_1 = 482.2 \pm 1.8$  kPa,  $C_2 = -82.8 \pm 2.2$  kPa, and  $C_3 = 11.3 \pm 0.8$  kPa were determined based on the data of uniaxial tensile and compression tests on SEBS. The material of the composite electrode was assumed to be a linear elastic material in its elastic deformation region with a Young's modulus of 114.5 MPa determined from tensile tests in Figure 4.6. The Poisson's ratio was set to 0.46. The contact between any two surfaces including self-contact was assumed to be a "hard" contact, which can minimize the penetration of the slave surfaces into the master surfaces at the constraint locations. During loading, the bottom surface of the structure was firmly clamped, and the top surface was compressed with a gradually increasing uniaxial displacement from 0 to 500 μm in 10 ms.



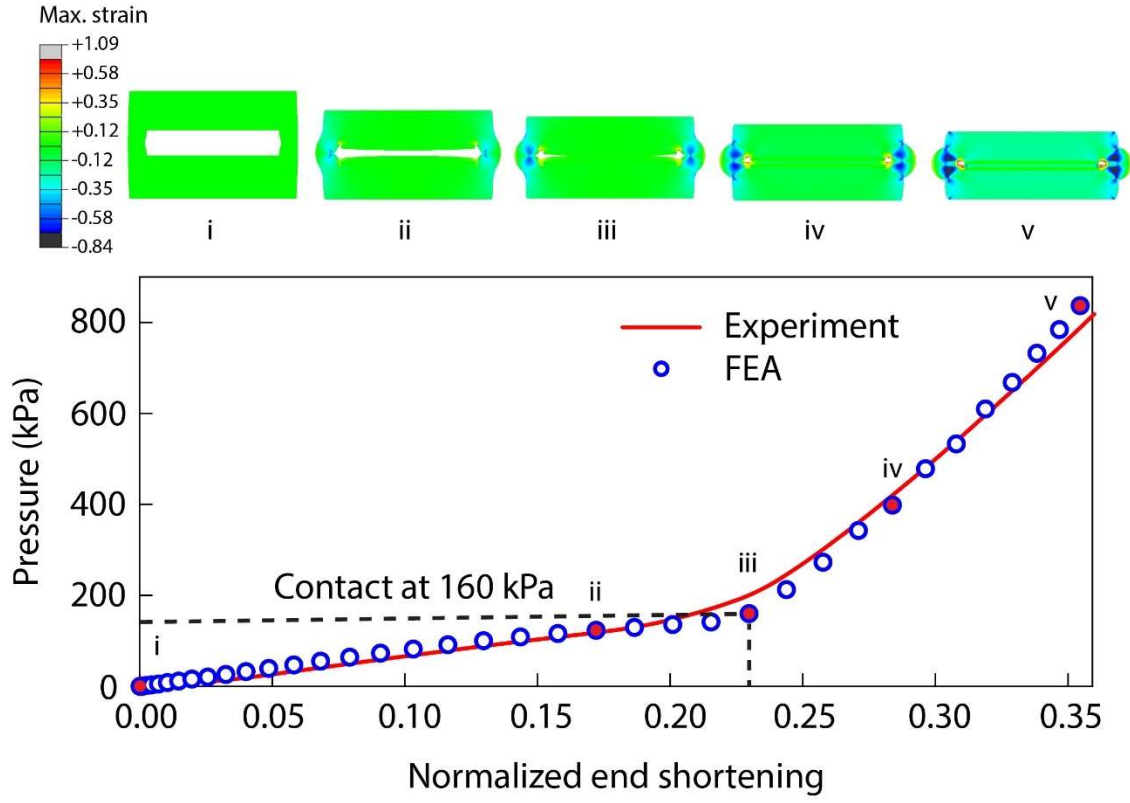


**Figure 5.9** Comparison of the mechanical response of the compressed fiber structure obtained through experimentation and the FEA. Normalized end shortening means the value of displacement divided by the original height of the fiber structure  $y_0$ . The top images show the simulated maximum principal logarithmic strain of the fiber under increasing pressures. The corresponding pressures and displacements are indicated in the pressure – normalized end shortening curve labelled by red dots.

In Figure 5.9, we compare the experimental and simulated pressure under compression, as a function of normalized end shortening of the fiber structure. “Normalized end shortening” in our discussion is defined as the induced displacement divided by the original thickness of the whole fiber structure. In Figure 5.9, we also show the maximum principal logarithmic strain distribution of four representative deformation states during the loading including its original state (i) for comparison. At low pressures, the entire applied force is undertaken by the two side walls of the open channel (ii). As the pressure increases, the two walls bend progressively, and eventually induces the contact between the top and bottom surfaces of the open channel. Meanwhile, both the top and bottom surfaces bend towards the

inner side of the channel during loading, making their contact a gradual process rather than an abrupt movement. Figures (iii) and (iv) show the moments of their first contact and full contact respectively. The FEA results indicate that the first contact occurs at the pressure of 160 kPa and normalized end shortening of 0.23 (displacement: 322  $\mu\text{m}$ ), which corresponds very well with the experimental results. With further loading, there is an increase of the stiffness of the structure, as indicated by the slope of pressure – normalized end shortening curve, given the compressive deformation of the SEBS body in addition to the continued bending of the two side walls (v). Note that the maximum principal logarithmic strain associated with this loading process achieves values as high as +1.09 and -0.84 (the positive and negative signs mean the tensile and compressive strains respectively). These large strain values highlight again the necessity of using SEBS elastomer rather than common thermoplastic materials, which cannot support such high levels of reversible deformation.

The excellent agreement between the experimentation values and the FEA model demonstrates the efficacy and robustness of our simulation, which enables us to quantitatively analyze the effects of the fibers' dimensions on their mechanical behaviors. Indeed, among various dimensional features, we anticipate that the width and height of the open channel play key roles on the trigger pressure and displacement. We therefore first varied the width of the channel  $x_1$ , while keeping all the other sizes unchanged. Figure 5.10a shows the pressure – normalized end shortening curves of fiber models with different channel widths. As the  $x_1/x_0$  varies from 0.5 to 0.95, the stiffness of the structures in the lower pressure region is reduced, as indicated by the decreased slopes before the contact point. The extracted values of end shortening at the contact point are the same, while the pressure decreases linearly with the  $x_1/x_0$ . This is due to the combined effect of the thinner side walls to sustain the load and the lower Euler's critical load for the occurrence of buckling at higher levels of  $x_1/x_0$ . We anticipate that a lower trigger pressure will be preferred for the TENG applications, therefore higher  $x_1/x_0$  values are desired provided that the drawability of the structure could be guaranteed.

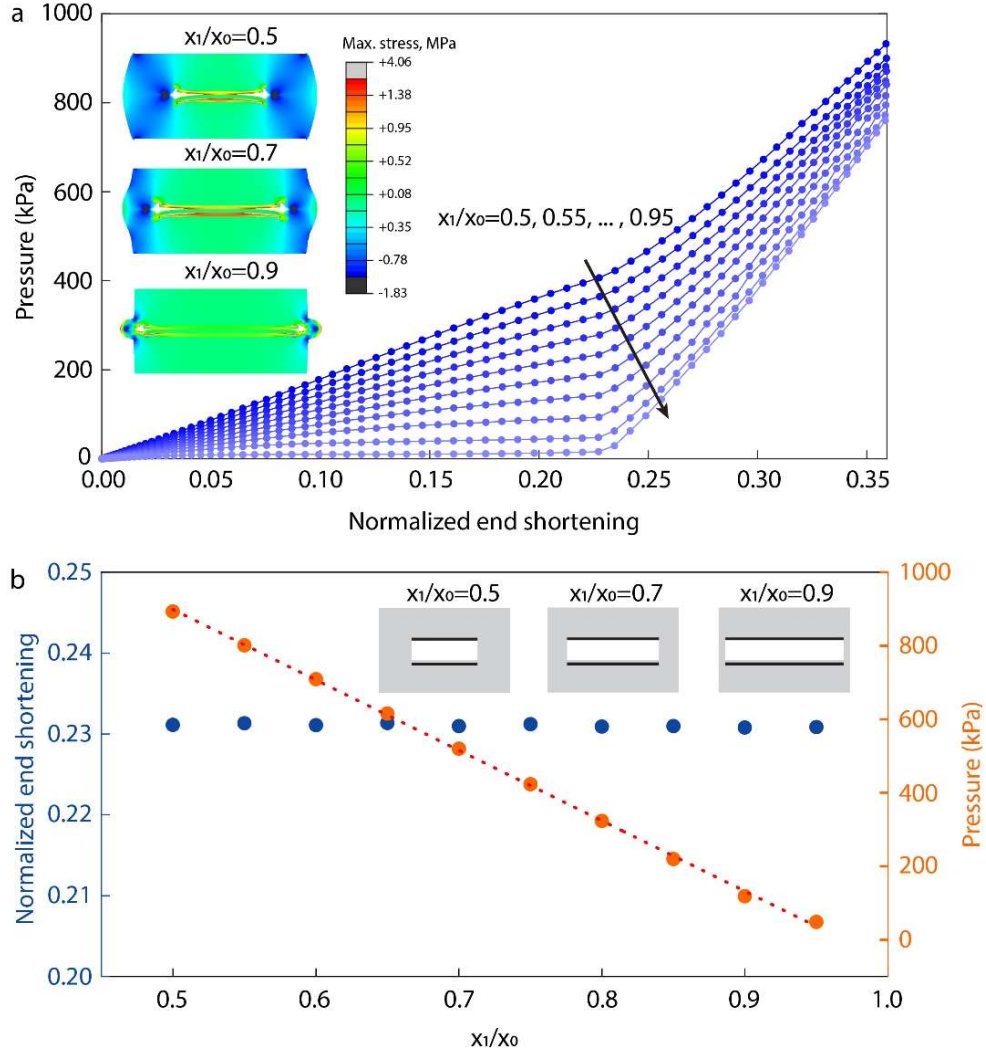


**Figure 5.10** The effects of the variation on the width of the open channel obtained from the FEA. (a) Simulated pressure as a function of normalized end shortening at various values of  $x_1/x_0$  ranging from 0.5 to 0.95. The values of  $x_1$  are varied, while  $x_0$ ,  $y_1$  and  $y_0$  are kept the same as the dimensions of the sample in our experiment, as shown in Figure 5.8. (b) Extracted values of end shortening and pressure as the top and bottom surfaces surrounding the channel come into contact. Insets in (a) show the maximum principal stress distribution of the fiber structure at the first contact as  $x_1/x_0$  equals to 0.5, 0.7 and 0.9 respectively. Schematics of their corresponding initial geometries are shown in the insets of (b).

Similarly, we also quantitatively investigated the effect of the height of the channel  $y_1$  on the deformation at the contact point. The mechanical curves of the fiber structures with  $y_1/y_0$  ranging from 0.05 to 0.35 are shown in Figure 5.11a. The same slopes of the curves reveal the identical stiffness of the structures. As shown in Figure 5.11b, the pressure at the contact point shows an initial increment with the height of the channel, followed by a decrease after reaching a plateau as  $y_1/y_0$  equals to 0.30, due to the occurrence of buckling. Nevertheless, the displacement at the contact point is only associated with the prescribed height of the channel.

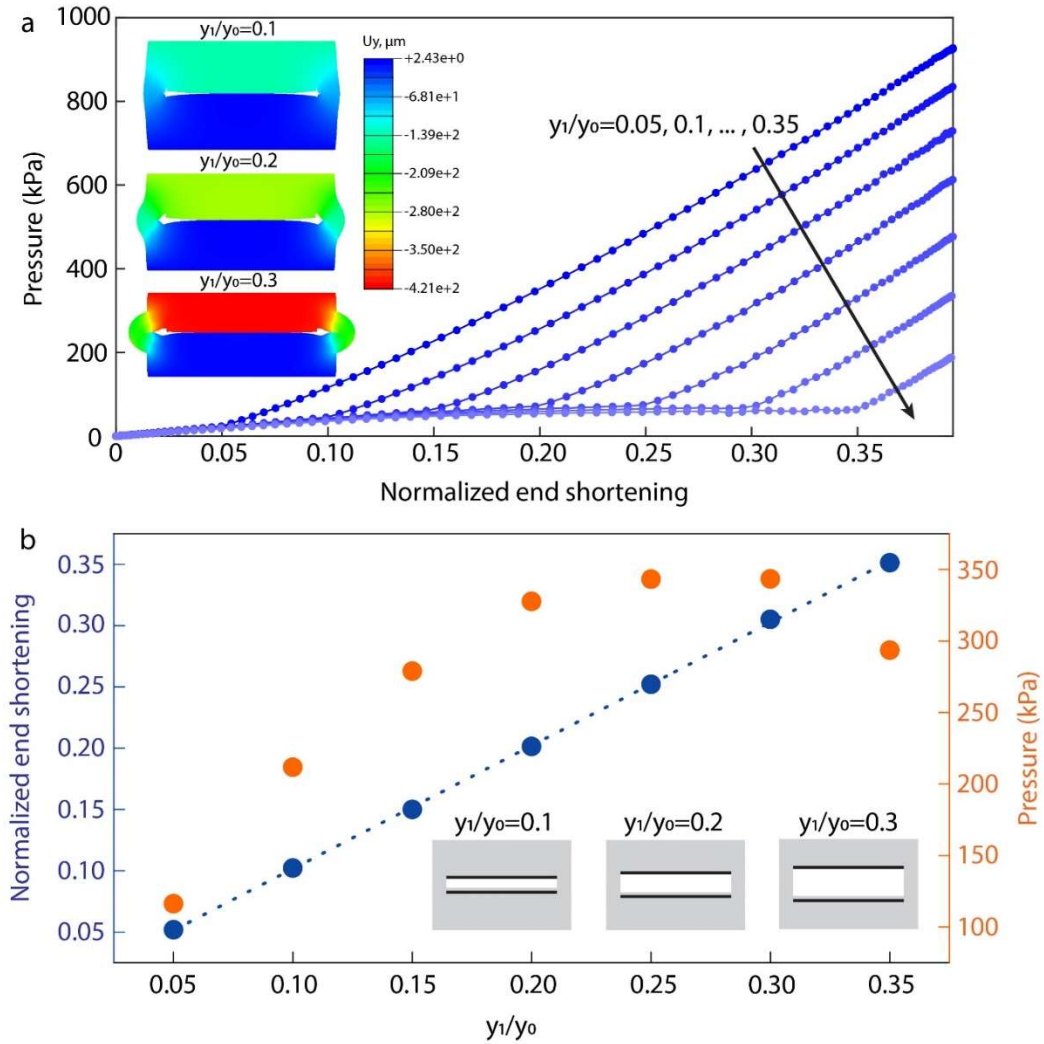


**Figure 5.11** Variation of the height of the open channel. (a) Simulated pressure as a function of normalized end shortening at various  $y_1/y_0$  between 0.05 and 0.35. The values of  $y_1$  are varied, while  $y_0$ ,  $x_1$  and  $x_0$  maintain the

same values as of the sample shown in Figure 5.8. (b) Extracted values of end shortening and pressure as the top and bottom surfaces surrounding the channel come into contact. Insets in (a) show the displacement distribution of the fiber structure at the first contact as  $y_1/y_0$  equals to 0.1, 0.2 and 0.3 respectively. Schematics of their corresponding initial geometries are shown in the insets of (b).

Overall, the mechanical response of the triboelectric fibers that we have developed can be divided into two regimes that are separated by the critical pressure corresponding to the contact between the two tribosurfaces. Above this critical pressure, we could observe and model an increase in stiffness, but the electrical output signals remain relatively constant, resulting in a reduced energy harvesting efficiency. However, our design is highly customizable to meet different ranges of critical pressure, and hence ranges of optimized output. Guided by FEA simulation, we can design preforms and fibers to meet requirements for a variety of applications.

### 5.3 Energy harvesting from other mechanical stimuli

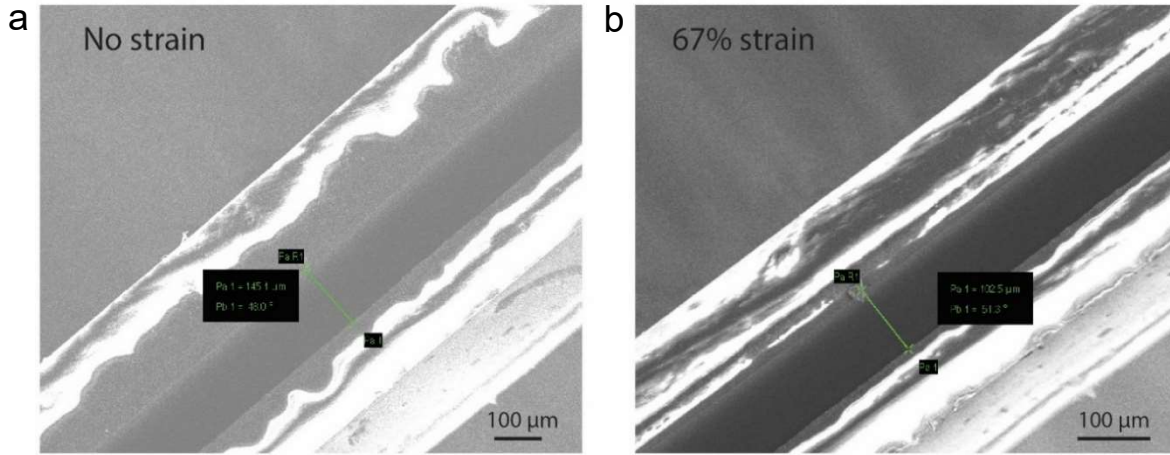


**Figure 5.12** SEM images of a fiber in the original state (a) and in the stretched state (b).

Due to the excellent deformability, the fiber has the potential to be capable of generating electrical outputs under different mechanical stimuli, without mechanical failure. We first characterized the fiber's mechanical response and electrical performance under stretching. As we have shown in the last section Chapter 5.1, the electrical output is highly dependent on the distance between the two triboelectric

surfaces. The hollow channel of the fiber is enclosed by two different super-elastic materials, and thus it is complex to analyze the changes of the dimensions of the gap upon stretching. We therefore cut a fiber along its longitudinal direction and performed in situ stretching SEM on the cross-section of the fiber to directly observe the change of gap size on tensile strain. The effective length of the fiber sample was 12 mm and the maximum extension was 8 mm. The original spacing between the two triboelectric parts was  $\sim 145.1 \mu\text{m}$  and reduced to  $\sim 102.5 \mu\text{m}$  at 67% strain (Figure 5.12).

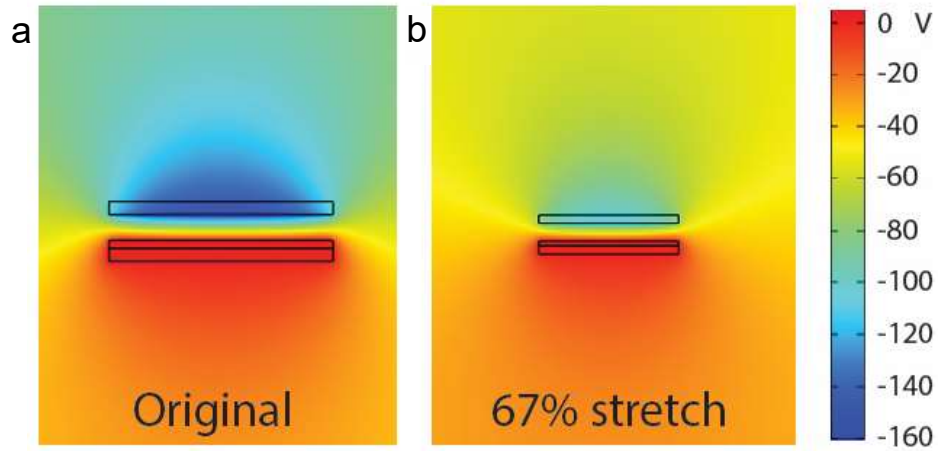


**Figure 5.13** Finite element analysis of the electric potential distribution of the fiber system before and after being stretched with a 67% strain.

**Table 5.2** Parameters set for the finite element simulation in Figure 5.9.

Parameters	No strain	67% Stretch
Length (cm)	1.2	2.0
Gap thickness (mm)	0.15	0.104
Bottom electrode width and thickness (mm)	1.3, 0.076	0.814, 0.0476
SEBS width and thickness (mm)	1.3, 0.044	0.814, 0.0275
Surface charge density ( $\text{C}/\text{m}^2$ )	$1.0\text{E-}5$	$1.046\text{e-}5$

In order to predict the effect of such a deformation to energy harvesting performance, we performed FEA to simulate the electric potential distribution at different tensile states, as shown in Figure 5.13. The dimensions of the fiber model are based on the in situ stretching SEM images. Considering the charge conservation principle, the total charge on the triboelectric layers remain the same. Hence, the

set charge density was modified accordingly based upon the areal change during the deformation. The detailed parameters for this simulation are listed in Table 5.2. As shown in figure, despite the increase of surface charge density, the open-circuit voltage between the two electrodes still decreases for the stretched fiber due to the reduced gap thickness.

To quantitatively evaluate the fiber's energy-harvesting performance triggered by stretching, we subjected the fiber to repeated stretching and relaxation deformation with various strain. As shown in Figure 5.14, the magnitude of both  $V_{oc}$  and  $Q_{sc}$  increase with the increased elongation of the fiber, which is consistent with the simulation results. By comparison, we can find that the fiber exhibits higher outputs under compression than stretching, due to the much larger relative displacement between the two triboelectric parts and more effective contact area under pressing.

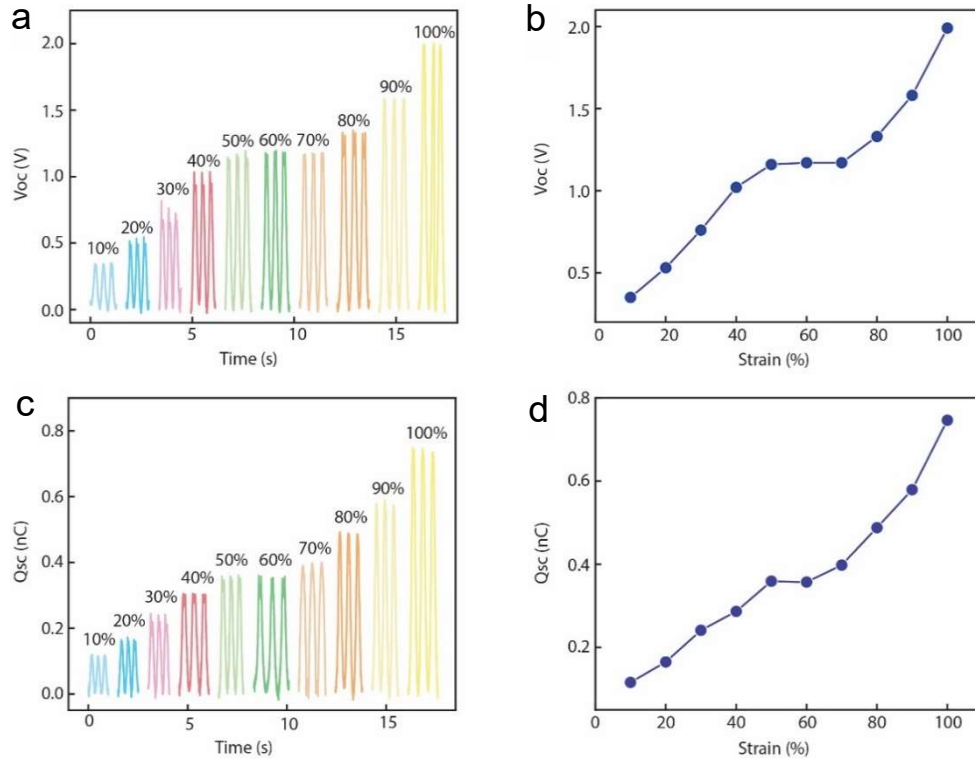


**Figure 5.14** Output performance of the TENG fiber under different strain: (a, b) open-circuit voltage, (c, d) short-circuit transferred charge.

## 5.4 Methods

The electrical connection for the tested fibers was realized by partially inserting metallic wires to the liquid metal channels followed by sealing with epoxy. Both the two extremities of the fiber were well sealed for the waterproofness test of the fiber in case water will flow into the channel that separates the two triboelectric parts. For the electrical output measurements of the fiber devices, a programmable electrometer (Keithley model 6517) was utilized to record the open-circuit voltage, short-circuit current and transferred charge. The data were collected and recorded by a Digilent Analog Discovery and computer-controlled software written in Labview. Custom setup composed of DC motors were used to apply cyclic pressing and stretching force to the tested fibers. A force sensitive resistor was attached to the DC motor for cyclic pressing to sense the applied compression force to the fiber sample. The resistor was calibrated with a dynamic mechanical analysis instrument (DMA, TA Instrument DMA Q800) before use. The relationship between the applied force and displacement of the fibers under compression was measured using the DMA, where the fibers were compressed between a top (15 mm) and bottom (30 mm) plates. The ramp force was set 5 N/mm. FEA simulations of the fibers' mechanical behavior was performed using the commercial Abaqus/Explicit package, which provides a more efficient and robust convergence performance in simulations involving complex structures compared to Abaqus/Standard.

## 5.5 Summary

In this chapter, we explored the potential of self-encapsulated stretchable fibers as conductor-to-dielectric contact-mode TENG devices. We first performed FEA simulation on the electric potential distribution of the fiber system under open-circuit conditions. The extracted voltage between the two electrodes increases linearly with the distance between them, due to the capacitive behaviour of the system. We performed Gauss theorem analysis on a simplified theoretical model of our fiber system to obtain the effect of the relative movement of the two tribosurfaces on the amount of transferred charges between the electrodes under short-circuit conditions. The analysis suggests that a relative movement distance around 300  $\mu\text{m}$  enables the flow back and forth of at least 90% of the net tribo charges, which provides us a solid guidance on the structural design to achieve a high working efficiency.

The advantageous effect of surface roughness on TENG devices' performance was confirmed by experimentally comparing the output waveforms of fibers with similar dimensions but with different



surface features. Thanks to the superior elasticity and water repelling properties of the cladding material, the proposed fiber system exhibited high robustness and reliability toward long-term operations under repeated large deformations or several days' storage in water. Our results showed that the electrical output signals of the fibers are significantly dependent on the compressive pressure. Overall, the output current increases linearly at low pressures and reaches a saturation as the pressure is high enough to trigger the contact of two tribosurfaces.

FEA simulation was performed to better understand the kinetic deformations of the fiber system under compression. The excellent agreement between the experimental and FEA results confirmed the applicability and efficacy of the established model. The quantitative analysis of the maximum principal logarithmic strain confirmed the high deformations of the structure during the loading, and highlight, once more, the necessity of using SEBS as the body material. The validity of the simulation enabled us to explore the effects of parametric modifications of the open channel's dimensions on the mechanical response of the fiber structures. With the overall dimensions of the fiber structures maintained unchanged, the critical pressure at the contact point decreases in a linear fashion with the width of the channel, while the critical displacement is directly proportional to the height of the channel. This understanding enables the precise prediction of the mechanical behavior of such fibers under compression and thus guides our customized designs for specific applications. In addition, we also demonstrated that the proposed fiber is capable of capturing energy from its stretching deformation. While the performance is still lower than in the pressure mode, such a mode of activation has rarely been demonstrated.

Finally, in addition to an increased specific surface area brought by the utilization of nano-/micro-scale materials, exploiting multilayer structures is another strategy to enhance the harvested energy. As shown in Figure 5.15a, the versatility of the thermal drawing process allows the realization of fibers with complex multilayer architectures. As indicated by the dash lines, the whole device can be divided into two parts, each of which equals to one discussed above. By connecting these two functional parts in parallel, the output signals almost doubled comparing with a single part triggered by repeated compressive force (Figure 5.15b). While this result is very recent and requires optimization, it demonstrates the versatility of the thermal drawing process and its potential to generate, in a scalable way, highly efficient triboelectric based energy harvesters and sensors with multiple modes of activation.

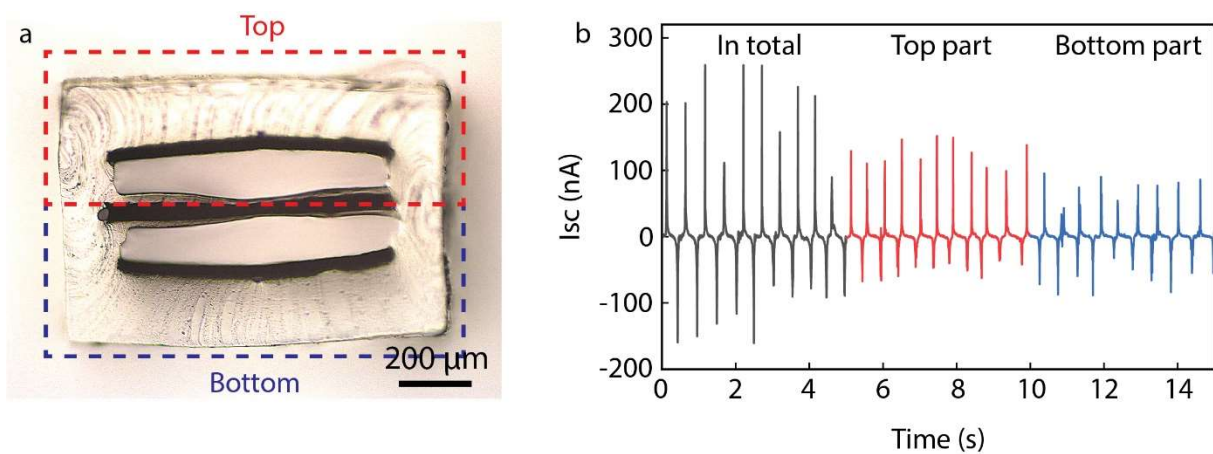


**Figure 5.15** Multilayered triboelectric fibers. (a) Cross-sectional structure. (b) Output currents of the whole device, top part and bottom part of the device respectively.

## Chapter 6 Conclusions

### 6.1 Conclusions

In this thesis, based on the scalable thermal drawing process conventionally utilized to manufacture optical fibers, we designed, fabricated and characterized several advanced electronic fibers. We proposed novel soft and stretchable materials, innovative and complex architectures with microscale feature sizes, and intriguing properties and functionalities in microfluidic and deformation sensing, as well as energy harvesting.

We first demonstrated the fabrication of a uniform capillary-like polymer fiber integrating a hollow channel of controlled size (potentially from a few to a few hundred micrometers), with polymer composite and metal electrodes running along its entire length. We showed that the fiber device is capable of sensing the presence and travel distance of a fluid, as well as detecting the flowrate in real-time and over a very wide range of velocities compared to other techniques. The capacitive fiber can also identify the static dielectric constant of the fluid inside the microchannel with high accuracy. Beyond such performance, the novel fabrication approach we propose, based on fiber processing, is highly scalable and can potentially yield tens-of-kilometers of such fibers in a single draw, equating millions of short (few centimeters) working capillaries. It offers significant opportunities for reliable monitoring and manipulation of complex microfluidics, especially in cases requiring flexible and disposable sensors, at a scalability and cost traditionally associated with fiber processing technologies. In addition, it also paves the way towards other novel opportunities in the fields of multi-functional medical probes, nerve scaffolds, and cell growth analysis.

We then demonstrated the design and scalable manufacture of novel liquid metal based triboelectric fibers and textiles with output performance orders of magnitude better than existing fiber technologies, and comparable to, or better than, the state-of-the-art planar configurations. Thanks to the combination of elastomeric materials and highly deformable liquid electrodes, the advanced fibers are capable of sustaining up to 560% elongation, ranging the highest deformation levels in triboelectric systems demonstrated thus far. The superior deformability of such fibers participates to their high performance, and enables their integration into large-area, elastic and machine-washable energy-harvesting textiles, with an open-circuit voltage of 490 V, and a short-circuit transferred charge of 175 nC. The fibers have

unique 3D microstructures (2D in the fiber cross-section, reproduced in 1D along the fiber axis), that only the special thermal drawing process can generate. While they can harvest energy, they can also sense deformation from a variety of mechanical stimuli, and maintain high outputs regardless of repeated extreme deformations. This work represents several breakthroughs: i) A new material never used before with better triboelectric performance than the best materials used thus far such as PTFE, yet adapted for advanced fiber-processing. ii) A new fiber processing approach for TENG devices that can microstructure this novel material in a scalable way while at the same time allowing it to encapsulate liquid metal electrodes. iii) This brings new design flexibility, fibers with unprecedented and innovative architectures capable of being very thin and long, and integrated in any platform including textiles. iv) We go beyond fiber and textile-based TENG devices by order of magnitude in terms of performance. We reach performance comparable to state-of-the-art 2D TENG devices, in a fiber form!

In a final part, we proposed conceptual advances to fiber-based energy harvesting systems in the aspects of materials, processes and device designs that bring novel materials, unprecedentedly complex architectures, peculiar properties as well as robust multifunctionalities. Specifically, we developed a highly soft and stretchable microstructured triboelectric fiber that integrates all the necessary functional components, including two triboelectric parts and an encapsulated large gap in between, within a water repellent elastomeric cladding. While patterning micro-textures on the soft triboelectric surfaces within a fiber is quite challenging, it was realized based on our studies of interfacial tensions and identification of a proper sacrificial layer to reduce thermal reflow during drawing. Working in the contact-separation mode, the produced fiber is capable of harvesting energy from a variety of mechanical deformations including but not limited to compression and stretching. The functionalities come from a structural subtlety that warrant a closer look. We therefore performed advanced FEA simulation on a 2D model representing the structure of the demonstrated fiber system and showed the level of control and engineering of the mechanical behaviors that can be achieved based on application-targeted fiber designs. The studies on triboelectric fibers in this thesis indeed brings innovative solutions to the scientific and technological challenges that the field of TENG devices, and fiber-based ones in particular, have been facing in the last years, i.e. a lack of well-thought out strategy regarding materials, processes and device architectures to go beyond proof-of-concepts and realize real applications.

## 6.2 Novel perspectives: Hydrogel-integrated functional fibers

Throughout the thesis, we gave different directions to further improve the materials and fiber devices that we have developed. Recently, I have started to take a different route to explore innovative compatible materials with an extreme softness, looking into the thermal drawing of hydrogel. This entails shining an entirely new light on the engineering of materials and their rheology in the context of thermal drawing that can unlock a wide range of novel functional applications in different technological fields. In this part, we briefly introduce our vision and strategies to realize advanced electronic fibers with unprecedented mechanical softness.

Implantable neuromodulation probes have been widely used to treat neurological diseases. However, current probes suffer from high rigidity and are limited by both low spatial resolution and mechanical mismatch with tissues, which always causes severe tissue damage and adverse immune responses. Designing and fabricating soft and stretchable electronics, especially with mechanical properties that match the ones of tissues, are becoming imperative. Among many engineering materials, hydrogels, owing to their unique tissue-mimicking mechanical properties, show great promise for various applications such as cell cultures, soft tissue adhesives, drug delivery, and implantations. However, pure ionic hydrogels lack electronic conductivity and the slow ion movement results in a slow response time, preventing them from, for example, interrogating at high-speed ( $> 1,000$  Hz) single-neuron-single-spike neural activity.

Besides their desirable mechanical properties, hydrogels allow the incorporation of various conductive materials into their porous structure to enhance their electrical conductivity. From the perspectives of materials processing and fiber fabrication, three challenging objectives need to be realized: (1) discover hydrogels that can be processed by fiber drawing; (2) introduce methods to incorporate conductive materials into their porous structure to realize electrical conductive hydrogel; (3) find processable stretchable insulation materials with low modulus that offer tissue-level softness.

Despite a wide range of polymeric materials for hydrogels, most commercially available hydrogels (natural hydrogels such as heparin and alginate, or synthetic hydrogels such as poly(vinyl alcohol)s and polyethylene glycols) are not compatible with the thermal drawing technique, due to their chemical crosslinking. Synthesized hydrogels, in particular, are not favored in this case due to their poor biocompatibility. Therefore, it is necessary to scan the library of natural hydrogels to find candidate

materials that are physically crosslinked, show proper viscosity profile at higher temperature to match with the drawing process, and can be chemically crosslinked afterwards.

Previously, Our group reported a controlled fabrication of gelatin-based fully edible fibers, by tailoring its viscosity profile with the addition of a plasticizer (e.g. glycerol), to ensure a plastic deformation at relatively high viscosity during fiber drawing.<sup>51</sup> We can take advantage of and modify this strategy to achieve our purpose, since gelatin is able to swell and retain large volume of water in its swollen three-dimensional structure, and form a hydrogel, once it is placed in excess water at room temperature. A challenge, however, is posed for their biomedical applications since gelatin dissolves rapidly in aqueous environments at body temperature. This problem can be solved by post-processing treatments, including the use of crosslinking chemicals (e.g. glutaraldehyde and genipin) and chemical modification to support photo-crosslinking (e.g., methacrylic anhydride). However, attention should be paid for these treatments since the use of such cross-linkers can lead to toxic side effects. Maillard reaction, a non-enzymatic reaction between the reactive functional groups of amino acids and reducing sugars, represents an alternative strategy to modify physical and mechanical properties of gelatin. Since it is a heating-promoted reaction, one strategy can be to trigger the Maillard reaction during the fiber drawing process with the assistance of high temperature in the furnace. We can prepare a gelatin hydrogel with proper pre-crosslinkage and viscosity profile with the addition of glycerol and a reducing sugar (e.g. ribose) to ensure a successful drawing. The degree of crosslinking can be controlled by tuning the type and amount of sugar and the water content in the gel, as well as the drawing temperature and the storage environment. The viscosity of such material system at high temperature can be influenced by the amount of water and glycerol inside. Taking this strategy, we have already drawn crosslinked gelatin fibers with much slower dissolution rate in 37 °C water. Besides serving as a matrix material for bioelectrodes, the successful fabrication of such fibers also opens their applications in other fields like biocompatible and biodegradable wound healing, nerve guiding scaffolds, or controlled drug release. In addition, agarose, a linear polysaccharide derived from algae, possesses a higher upper critical solution temperature so that it can be in a stable gel state in body environment. Preliminary experiments have shown that agarose has a good compatibility with the drawing process, while its mechanical properties needs to be further tailored for practical applications.

The conductive materials that can potentially be incorporated in hydrogels can be conductive polymers such as polypyrrole, poly(3,4-ethylenedioxythiophene) polystyrene sulfonate (PEDOT:PSS),

or metal-based nanomaterials like silver nanowires. Expected challenge is that, the hydrogels after processing should satisfy several rigorous requirements, including homogeneous structure, gel ability, good electrical conductivity and mechanical properties, stable and reliable operation in body environment. We hope to realize this goal by transferring existing fabrication technology from other fields.

## Bibliography

1. Yan, W. *et al.* Thermally drawn advanced functional fibers: New frontier of flexible electronics. *Mater. Today* **35**, 168–194 (2020).
2. Shi, J. *et al.* Smart Textile-Integrated Microelectronic Systems for Wearable Applications. *Adv. Mater.* **32**, 1–37 (2020).
3. Li, J., Wong, W. Y. & Tao, X. M. Recent advances in soft functional materials: Preparation, functions and applications. *Nanoscale* **12**, 1281–1306 (2020).
4. Rogers, J. A., Someya, T. & Huang, Y. Materials and Mechanics for Stretchable Electronics. *Science* **327**, 1603–1607 (2010).
5. Mannsfeld, S. C. B. *et al.* Highly sensitive flexible pressure sensors with microstructured rubber dielectric layers. *Nat. Mater.* **9**, 859–864 (2010).
6. Jeong, H., Rogers, J. A. & Xu, S. Continuous on-body sensing for the COVID-19 pandemic: Gaps and opportunities. *Sci. Adv.* **6**, 1–5 (2020).
7. Han, M. *et al.* Catheter-integrated soft multilayer electronic arrays for multiplexed sensing and actuation during cardiac surgery. *Nat. Biomed. Eng.* **4**, 997–1009 (2020).
8. Pham, T. A. *et al.* A Versatile Sacrificial Layer for Transfer Printing of Wide Bandgap Materials for Implantable and Stretchable Bioelectronics. *Adv. Funct. Mater.* **2004655**, 1–10 (2020).
9. Mineev, I. R. *et al.* Electronic dura mater for long-term multimodal neural interfaces. *Science* **347**, 159–163 (2015).
10. Lacour, S. P., Courtine, G. & Guck, J. Materials and technologies for soft implantable neuroprostheses. *Nat. Rev. Mater.* **1**, 16063 (2016).
11. Sitti, M. Miniature soft robots — road to the clinic. *Nat. Rev. Mater.* **3**, 74–75 (2018).
12. Yin, R. *et al.* Wireless Multistimulus-Responsive Fabric-Based Actuators for Soft Robotic, Human–Machine Interactive, and Wearable Applications. *Adv. Mater. Technol.* **5**, 1–11 (2020).



13. Zou, Y. *et al.* A bionic stretchable nanogenerator for underwater sensing and energy harvesting. *Nat. Commun.* **10**, 1–10 (2019).
14. Bandodkar, A. J. *et al.* Sweat-activated biocompatible batteries for epidermal electronic and microfluidic systems. *Nat. Electron.* **3**, 554–562 (2020).
15. Tao, X. Study of Fiber-Based Wearable Energy Systems. *Acc. Chem. Res.* **52**, 307–315 (2019).
16. Yan, W. *et al.* Advanced Multimaterial Electronic and Optoelectronic Fibers and Textiles. *Adv. Mater.* **31**, 1802348 (2019).
17. Weng, W., Chen, P., He, S., Sun, X. & Peng, H. Smart Electronic Textiles. *Angew. Chemie Int. Ed.* **55**, 6140–6169 (2016).
18. Hart, S. D. External Reflection from Omnidirectional Dielectric Mirror Fibers. *Science (80-. ).* **296**, 510–513 (2002).
19. Bayandir, M. *et al.* Metal – insulator – semiconductor optoelectronic fibres. *Nature* **431**, 826–829 (2004).
20. Nguyen-Dang, T. *et al.* Controlled Sub-Micrometer Hierarchical Textures Engineered in Polymeric Fibers and Microchannels via Thermal Drawing. *Adv. Funct. Mater.* **27**, 1605935 (2017).
21. Yan, W. *et al.* Structured nanoscale metallic glass fibres with extreme aspect ratios. *Nat. Nanotechnol.* **15**, 875–882 (2020).
22. Shadman, S. *et al.* Microstructured Biodegradable Fibers for Advanced Control Delivery. *Adv. Funct. Mater.* **30**, 1–9 (2020).
23. Canales, A. *et al.* Multifunctional fibers for simultaneous optical, electrical and chemical interrogation of neural circuits in vivo. *Nat. Biotechnol.* **33**, 277–284 (2015).
24. Lu, C. *et al.* Polymer Fiber Probes Enable Optical Control of Spinal Cord and Muscle Function In Vivo. *Adv. Funct. Mater.* **24**, 6594–6600 (2014).
25. Guo, Y. *et al.* Polymer Composite with Carbon Nanofibers Aligned during Thermal Drawing as

- a Microelectrode for Chronic Neural Interfaces. *ACS Nano* **11**, 6574–6585 (2017).
26. Yuan, R. *et al.* Microfluidics in structured multimaterial fibers. *Proc. Natl. Acad. Sci.* **115**, E10830–E10838 (2018).
  27. Park, J. *et al.* In situ electrochemical generation of nitric oxide for neuronal modulation. *Nat. Nanotechnol.* **15**, 690–697 (2020).
  28. Nguyen-Dang, T. *et al.* Multi-material micro-electromechanical fibers with bendable functional domains. *J. Phys. D. Appl. Phys.* **50**, 144001 (2017).
  29. Chen, B., Kwok, C., Nguyen, T. N. & Wang, Z. Integrated Fiber Flow Sensors for Microfluidic Interconnects. *Adv. Mater. Technol.* **3**, 1800175 (2018).
  30. Lee, J. T., Grena, B. J.-B., Khudiyev, T., Hou, C. & Fink, Y. Thermally-Drawn Fiber Including Electrochemically Active Gels. U.S. Patent Application No. 16/361,157 (2020).
  31. Rein, M. *et al.* Diode fibres for fabric-based optical communications. *Nature* **560**, 214–218 (2018).
  32. Yu, L. *et al.* Flexible Multi-Material Fibers for Distributed Pressure and Temperature Sensing. *Adv. Funct. Mater.* **1908915**, 1–8 (2020).
  33. Yan, W. *et al.* Semiconducting Nanowire-Based Optoelectronic Fibers. *Adv. Mater.* **29**, 1700681 (2017).
  34. Yan, W. *et al.* Microstructure tailoring of selenium-core multimaterial optoelectronic fibers. *Opt. Mater. Express* **7**, 1388 (2017).
  35. Abouraddy, A. F. *et al.* Large-scale optical-field measurements with geometric fibre constructs. *Nat. Mater.* **5**, 532–536 (2006).
  36. Gumennik, A. *et al.* All-in-Fiber Chemical Sensing. *Adv. Mater.* **24**, 6005–6009 (2012).
  37. Bayindir, M., Abouraddy, A. F., Arnold, J., Joannopoulos, J. D. & Fink, Y. Thermal-Sensing Fiber Devices by Multimaterial Codrawing. *Adv. Mater.* **18**, 845–849 (2006).

38. Zhang, T. *et al.* High-performance, flexible, and ultralong crystalline thermoelectric fibers. *Nano Energy* **41**, 35–42 (2017).
39. Danto, S., Ruff, Z., Wang, Z., Joannopoulos, J. D. & Fink, Y. Ovonic memory switching in multimaterial fibers. *Adv. Funct. Mater.* **21**, 1095–1101 (2011).
40. Danto, S. *et al.* Fiber field-effect device via in situ channel crystallization. *Adv. Mater.* **22**, 4162–4166 (2010).
41. Lestoquoy, G., Chocat, N., Wang, Z., Joannopoulos, J. D. & Fink, Y. Fabrication and characterization of thermally drawn fiber capacitors. *Appl. Phys. Lett.* **102**, 152908 (2013).
42. Gorgutsa, S., Gu, J. F. & Skorobogatiy, M. A woven 2D touchpad sensor and a 1D slide sensor using soft capacitor fibers. *Smart Mater. Struct.* **21**, 015010 (2012).
43. Egusa, S. *et al.* Multimaterial piezoelectric fibres. *Nat. Mater.* **9**, 643–648 (2010).
44. Chocat, N. *et al.* Piezoelectric fibers for conformal acoustics. *Adv. Mater.* **24**, 5327–5332 (2012).
45. Wang, S. *et al.* Flexible Piezoelectric Fibers for Acoustic Sensing and Positioning. *Adv. Electron. Mater.* **3**, 1–7 (2017).
46. Khudiyev, T. *et al.* Electrostrictive microelectromechanical fibres and textiles. *Nat. Commun.* **8**, 1435 (2017).
47. Lu, C. *et al.* Flexible and stretchable nanowire-coated fibers for optoelectronic probing of spinal cord circuits. *Sci. Adv.* **3**, e1600955 (2017).
48. Qu, Y. *et al.* Superelastic Multimaterial Electronic and Photonic Fibers and Devices via Thermal Drawing. *Adv. Mater.* **30**, 1707251 (2018).
49. Leber, A. *et al.* Compressible and Electrically Conducting Fibers for Large-Area Sensing of Pressures. *Adv. Funct. Mater.* **30**, 1–10 (2020).
50. Leber, A. *et al.* Soft and stretchable liquid metal transmission lines as distributed probes of multimodal deformations. *Nat. Electron.* **3**, 316–326 (2020).

51. Sordo, F. *et al.* Microstructured Fibers for the Production of Food. *Adv. Mater.* **31**, 1807282 (2019).
52. Dong, C., Page, A. G., Yan, W., Nguyen-Dang, T. & Sorin, F. Microstructured Multimaterial Fibers for Microfluidic Sensing. *Adv. Mater. Technol.* **4**, 1900417 (2019).
53. Whitesides, G. M. The origins and the future of microfluidics. *Nature* **442**, 368–373 (2006).
54. Haneveld, J. *et al.* Modeling, design, fabrication and characterization of a micro Coriolis mass flow sensor. *J. Micromechanics Microengineering* **20**, 125001 (2010).
55. Lien, V. & Vollmer, F. Microfluidic flow rate detection based on integrated optical fiber cantilever. *Lab Chip* **7**, 1352–1356 (2007).
56. Polynkin, P., Polynkin, A., Peyghambarian, N. & Mansuripur, M. Evanescent field-based optical fiber sensing device for measuring the refractive index of liquids in microfluidic channels. *Opt. Lett.* **30**, 1273 (2005).
57. Hu, R. P. & Huang, X. G. A Simple Fiber-Optic Flowmeter Based on Bending Loss. *IEEE Sens. J.* **9**, 1952–1955 (2009).
58. Berthet, H., Jundt, J., Durivault, J., Mercier, B. & Angelescu, D. Time-of-flight thermal flowrate sensor for lab-on-chip applications. *Lab Chip* **11**, 215–223 (2011).
59. Collins, J. & Lee, A. P. Microfluidic flow transducer based on the measurement of electrical admittance. *Lab Chip* **4**, 7–10 (2004).
60. Alvarado, J., Mireles, J. & Soriano, G. Development and characterization of a capacitance-based microscale flowmeter. *Flow Meas. Instrum.* **20**, 81–84 (2009).
61. Kuo, J. T. W., Yu, L. & Meng, E. Micromachined Thermal Flow Sensors—A Review. *Micromachines* **3**, 550–573 (2012).
62. Zhang, Q. *et al.* A self-bended piezoresistive microcantilever flow sensor for low flow rate measurement. *Sensors Actuators A Phys.* **158**, 273–279 (2010).
63. Szekely, L., Reichert, J. & Freitag, R. Non-invasive nano-flow sensor for application in micro-

- fluidic systems. *Sensors Actuators A Phys.* **113**, 48–53 (2004).
64. Wang, P. & Anderko, A. Computation of dielectric constants of solvent mixtures and electrolyte solutions. *Fluid Phase Equilib.* **186**, 103–122 (2001).
  65. Temiz, Y. & Delamarche, E. Sub-nanoliter, real-time flow monitoring in microfluidic chips using a portable device and smartphone. *Sci. Rep.* **8**, 10603 (2018).
  66. Chiang, C. & Huang, Y. A Semicylindrical Capacitive Sensor With Interface Circuit Used for Flow Rate Measurement. *IEEE Sens. J.* **6**, 1564–1570 (2006).
  67. Stolyarov, A. M. *et al.* Fabrication and characterization of fibers with built-in liquid crystal channels and electrodes for transverse incident-light modulation. *Appl. Phys. Lett.* **101**, 011108 (2012).
  68. Mohsen-Nia, M., Amiri, H. & Jazi, B. Dielectric constants of water, methanol, ethanol, butanol and acetone: measurement and computational study. *J. Solution Chem.* **39**, 701–708 (2010).
  69. Nagai, T. & Prakongpan, S. Solubility of acetaminophen in cosolvents. *Chem. Pharm. Bull.* **32**, 340–343 (1984).
  70. Ishai, P. Ben, Talary, M. S., Caduff, A., Levy, E. & Feldman, Y. Electrode polarization in dielectric measurements: a review. *Meas. Sci. Technol.* **24**, 102001 (2013).
  71. Gregory, A. P. & Clarke, R. N. Traceable measurements of the static permittivity of dielectric reference liquids over the temperature range 5–50 C. *Meas. Sci. Technol.* **16**, 1506 (2005).
  72. Jouyban, A., Soltanpour, S. & Chan, H.-K. A simple relationship between dielectric constant of mixed solvents with solvent composition and temperature. *Int. J. Pharm.* **269**, 353–360 (2004).
  73. Dong, C. *et al.* High-efficiency super-elastic liquid metal based triboelectric fibers and textiles. *Nat. Commun.* **11**, 3537 (2020).
  74. Cherenack, K. & van Pieterse, L. Smart textiles: Challenges and opportunities. *J. Appl. Phys.* **112**, 091301 (2012).
  75. Stoppa, M. & Chiolerio, A. Wearable Electronics and Smart Textiles: A Critical Review. *Sensors*

- 14**, 11957–11992 (2014).
76. Hu, Y. & Zheng, Z. Progress in textile-based triboelectric nanogenerators for smart fabrics. *Nano Energy* **56**, 16–24 (2019).
  77. Leber, A., Cholist, B., Sandt, J., Vogel, N. & Kolle, M. Stretchable Thermoplastic Elastomer Optical Fibers for Sensing of Extreme Deformations. *Adv. Funct. Mater.* **29**, 1802629 (2018).
  78. Lu, N. & Kim, D.-H. Flexible and Stretchable Electronics Paving the Way for Soft Robotics. *Soft Robot.* **1**, 53–62 (2014).
  79. Sun, H., Zhang, Y., Zhang, J., Sun, X. & Peng, H. Energy harvesting and storage in 1D devices. *Nat. Rev. Mater.* **2**, 17023 (2017).
  80. O'Regan, B. & Grätzel, M. A low-cost, high-efficiency solar cell based on dye-sensitized colloidal TiO<sub>2</sub> films. *Nature* **353**, 737–740 (1991).
  81. Bubnova, O. *et al.* Optimization of the thermoelectric figure of merit in the conducting polymer poly(3,4-ethylenedioxythiophene). *Nat. Mater.* **10**, 429–433 (2011).
  82. Luo, J. & Wang, Z. L. Recent advances in triboelectric nanogenerator based self-charging power systems. *Energy Storage Mater.* **23**, 617–628 (2019).
  83. Wang, Z. L., Chen, J. & Lin, L. Progress in triboelectric nanogenerators as a new energy technology and self-powered sensors. *Energy Environ. Sci.* **8**, 2250–2282 (2015).
  84. Zhao, J. *et al.* Remarkable merits of triboelectric nanogenerator than electromagnetic generator for harvesting small-amplitude mechanical energy. *Nano Energy* **61**, 111–118 (2019).
  85. Fan, F.-R., Tian, Z.-Q. & Lin Wang, Z. Flexible triboelectric generator. *Nano Energy* **1**, 328–334 (2012).
  86. Zhang, Q. *et al.* Green hybrid power system based on triboelectric nanogenerator for wearable/portable electronics. *Nano Energy* **55**, 151–163 (2019).
  87. Zeng, W. *et al.* Fiber-Based Wearable Electronics: A Review of Materials, Fabrication, Devices, and Applications. *Adv. Mater.* **26**, 5310–5336 (2014).

88. Huang, Q., Wang, D. & Zheng, Z. Textile-Based Electrochemical Energy Storage Devices. *Adv. Energy Mater.* **6**, 1600783 (2016).
89. Yu, X. *et al.* A coaxial triboelectric nanogenerator fiber for energy harvesting and sensing under deformation. *J. Mater. Chem. A* **5**, 6032–6037 (2017).
90. Dong, K. *et al.* 3D Orthogonal Woven Triboelectric Nanogenerator for Effective Biomechanical Energy Harvesting and as Self-Powered Active Motion Sensors. *Adv. Mater.* **29**, 1702648 (2017).
91. He, X. *et al.* A Highly Stretchable Fiber-Based Triboelectric Nanogenerator for Self-Powered Wearable Electronics. *Adv. Funct. Mater.* **27**, 1604378 (2017).
92. Li, X. *et al.* 3D Fiber-Based Hybrid Nanogenerator for Energy Harvesting and as a Self-Powered Pressure Sensor. *ACS Nano* **8**, 10674–10681 (2014).
93. Dong, K. *et al.* A Highly Stretchable and Washable All-Yarn-Based Self-Charging Knitting Power Textile Composed of Fiber Triboelectric Nanogenerators and Supercapacitors. *ACS Nano* **11**, 9490–9499 (2017).
94. Ryu, J. *et al.* Intrinsically stretchable multi-functional fiber with energy harvesting and strain sensing capability. *Nano Energy* **55**, 348–353 (2019).
95. Zhong, J. *et al.* Fiber-Based Generator for Wearable Electronics and Mobile Medication. *ACS Nano* **8**, 6273–6280 (2014).
96. Zhao, Z. *et al.* Machine-Washable Textile Triboelectric Nanogenerators for Effective Human Respiratory Monitoring through Loom Weaving of Metallic Yarns. *Adv. Mater.* **28**, 10267–10274 (2016).
97. Yang, Y. *et al.* Liquid-Metal-Based Super-Stretchable and Structure-Designable Triboelectric Nanogenerator for Wearable Electronics. *ACS Nano* **12**, 2027–2034 (2018).
98. Lai, Y.-C. *et al.* Single-Thread-Based Wearable and Highly Stretchable Triboelectric Nanogenerators and Their Applications in Cloth-Based Self-Powered Human-Interactive and Biomedical Sensing. *Adv. Funct. Mater.* **27**, 1604462 (2017).

99. Zhu, G. *et al.* Triboelectric-Generator-Driven Pulse Electrodeposition for Micropatterning. *Nano Lett.* **12**, 4960–4965 (2012).
100. Diaz, A. F. & Felix-Navarro, R. M. A semi-quantitative tribo-electric series for polymeric materials: the influence of chemical structure and properties. *J. Electrostat.* **62**, 277–290 (2004).
101. Wang, Z. L. Triboelectric Nanogenerators as New Energy Technology for Self-Powered Systems and as Active Mechanical and Chemical Sensors. *ACS Nano* **7**, 9533–9557 (2013).
102. Zhu, S. *et al.* Ultrastretchable Fibers with Metallic Conductivity Using a Liquid Metal Alloy Core. *Adv. Funct. Mater.* **23**, 2308–2314 (2013).
103. Fassler, A. & Majidi, C. Liquid-Phase Metal Inclusions for a Conductive Polymer Composite. *Adv. Mater.* **27**, 1928–1932 (2015).
104. Seung, W. *et al.* Nanopatterned Textile-Based Wearable Triboelectric Nanogenerator. *ACS Nano* **9**, 3501–3509 (2015).
105. Nguyen Dang, T., Richard, I., Goy, E., Sordo, F. & Sorin, F. Insights into the fabrication of sub-100 nm textured thermally drawn fibers. *J. Appl. Phys.* **125**, 175301 (2019).
106. Zhong, J. *et al.* Finger typing driven triboelectric nanogenerator and its use for instantaneously lighting up LEDs. *Nano Energy* **2**, 491–497 (2013).
107. Yang, Y. *et al.* Coaxial Triboelectric Nanogenerator and Supercapacitor Fiber-Based Self-Charging Power Fabric. *ACS Appl. Mater. Interfaces* **10**, 42356–42362 (2018).
108. Gong, W. *et al.* A wearable, fibroid, self-powered active kinematic sensor based on stretchable sheath-core structural triboelectric fibers. *Nano Energy* **39**, 673–683 (2017).
109. Gong, W. *et al.* Continuous and scalable manufacture of amphibious energy yarns and textiles. *Nat. Commun.* **10**, 868 (2019).
110. Sim, H. J. *et al.* Stretchable Triboelectric Fiber for Self-powered Kinematic Sensing Textile. *Sci. Rep.* **6**, 35153 (2016).
111. Cheng, Y. *et al.* A stretchable fiber nanogenerator for versatile mechanical energy harvesting



- and self-powered full-range personal healthcare monitoring. *Nano Energy* **41**, 511–518 (2017).
112. Yi, F. *et al.* A highly shape-adaptive, stretchable design based on conductive liquid for energy harvesting and self-powered biomechanical monitoring. *Sci. Adv.* **2**, e1501624 (2016).
  113. Kwak, S. S. *et al.* Fully Stretchable Textile Triboelectric Nanogenerator with Knitted Fabric Structures. *ACS Nano* **11**, 10733–10741 (2017).
  114. Zhou, T. *et al.* Woven Structured Triboelectric Nanogenerator for Wearable Devices. *ACS Appl. Mater. Interfaces* **6**, 14695–14701 (2014).
  115. Yu, A. *et al.* Core–Shell-Yarn-Based Triboelectric Nanogenerator Textiles as Power Cloths. *ACS Nano* **11**, 12764–12771 (2017).
  116. Pu, X. *et al.* Wearable Self-Charging Power Textile Based on Flexible Yarn Supercapacitors and Fabric Nanogenerators. *Adv. Mater.* **28**, 98–105 (2016).
  117. Shin, Y.-E. *et al.* Sewing machine stitching of polyvinylidene fluoride fibers: programmable textile patterns for wearable triboelectric sensors. *J. Mater. Chem. A* **6**, 22879–22888 (2018).
  118. Jiang, C. *et al.* All-electrospun flexible triboelectric nanogenerator based on metallic MXene nanosheets. *Nano Energy* **59**, 268–276 (2019).
  119. Chen, J. *et al.* Micro-cable structured textile for simultaneously harvesting solar and mechanical energy. *Nat. Energy* **1**, 16138 (2016).
  120. He, T. *et al.* Beyond energy harvesting - multi-functional triboelectric nanosensors on a textile. *Nano Energy* **57**, 338–352 (2019).
  121. Qiu, Q. *et al.* Highly flexible, breathable, tailorable and washable power generation fabrics for wearable electronics. *Nano Energy* **58**, 750–758 (2019).
  122. Pu, X. *et al.* A Self-Charging Power Unit by Integration of a Textile Triboelectric Nanogenerator and a Flexible Lithium-Ion Battery for Wearable Electronics. *Adv. Mater.* **27**, 2472–2478 (2015).
  123. Gong, J. *et al.* Towards truly wearable energy harvesters with full structural integrity of fiber materials. *Nano Energy* **58**, 365–374 (2019).

124. Tian, Z. *et al.* Performance-boosted triboelectric textile for harvesting human motion energy. *Nano Energy* **39**, 562–570 (2017).
125. Xiong, J. *et al.* Wearable All-Fabric-Based Triboelectric Generator for Water Energy Harvesting. *Adv. Energy Mater.* **7**, 1701243 (2017).
126. Chen, J. *et al.* Traditional weaving craft for one-piece self-charging power textile for wearable electronics. *Nano Energy* **50**, 536–543 (2018).
127. Chen, C. *et al.* 3D double-faced interlock fabric triboelectric nanogenerator for bio-motion energy harvesting and as self-powered stretching and 3D tactile sensors. *Mater. Today* **32**, 84–93 (2020).
128. Xiong, J. *et al.* Skin-touch-actuated textile-based triboelectric nanogenerator with black phosphorus for durable biomechanical energy harvesting. *Nat. Commun.* **9**, 4280 (2018).
129. Huang, T. *et al.* Fabric texture design for boosting the performance of a knitted washable textile triboelectric nanogenerator as wearable power. *Nano Energy* **58**, 375–383 (2019).
130. Kim, K. N. *et al.* Highly Stretchable 2D Fabrics for Wearable Triboelectric Nanogenerator under Harsh Environments. *ACS Nano* **9**, 6394–6400 (2015).
131. Amjadi, M., Kyung, K.-U., Park, I. & Sitti, M. Stretchable, Skin-Mountable, and Wearable Strain Sensors and Their Potential Applications: A Review. *Adv. Funct. Mater.* **26**, 1678–1698 (2016).
132. Dong, K., Peng, X. & Wang, Z. L. Fiber/Fabric-Based Piezoelectric and Triboelectric Nanogenerators for Flexible/Stretchable and Wearable Electronics and Artificial Intelligence. *Adv. Mater.* **1902549**, 1902549 (2019).
133. Wang, Z. *et al.* Designer patterned functional fibers via direct imprinting in thermal drawing. *Nat. Commun.* **11**, 1–9 (2020).
134. Feng, Z. *et al.* Scalable, washable and lightweight triboelectric-energy-generating fibers by the thermal drawing process for industrial loom weaving. *Nano Energy* **74**, (2020).
135. Zhang, X.-S., Brugger, J. & Kim, B. A silk-fibroin-based transparent triboelectric generator suitable for autonomous sensor network. *Nano Energy* **20**, 37–47 (2016).

136. Kurusu, R. S. & Demarquette, N. R. Blending and morphology control to turn hydrophobic SEBS electrospun mats superhydrophilic. *Langmuir* **31**, 5495–5503 (2015).
137. Le Floch, P. *et al.* Wearable and Washable Conductors for Active Textiles. *ACS Appl. Mater. Interfaces* **9**, 25542–25552 (2017).
138. Ferdinand, A. & Springer, J. Gas permeability of block copolymers of styrene and butadiene. *Colloid Polym. Sci.* **267**, 1057–1063 (1989).
139. Kang, D., Matsuki, S. & Tai, Y. Study of the hybrid parylene/PDMS material. in *2015 28th IEEE International Conference on Micro Electro Mechanical Systems (MEMS)* 397–400 (IEEE, 2015).
140. Yun, S. J. *et al.* Water vapor transmission rate property of SiNx thin films prepared by low temperature (<100 °C) linear plasma enhanced chemical vapor deposition. *Vacuum* **148**, 33–40 (2018).
141. Andringa, A. M. *et al.* Low-Temperature Plasma-Assisted Atomic Layer Deposition of Silicon Nitride Moisture Permeation Barrier Layers. *ACS Appl. Mater. Interfaces* **7**, 22525–22532 (2015).
142. Call, J. *et al.* Methodology and systems to ensure reliable thin-film PV modules. *Reliab. Photovolt. Cells, Modul. Components, Syst.* **7048**, 70480S (2008).
143. Domansky, K. *et al.* SEBS elastomers for fabrication of microfluidic devices with reduced drug absorption by injection molding and extrusion. *Microfluid. Nanofluidics* **21**, 1–12 (2017).
144. Madhavan, K. & Reddy, B. S. R. Poly(dimethylsiloxane-urethane) membranes: Effect of hard segment in urethane on gas transport properties. *J. Memb. Sci.* **283**, 357–365 (2006).
145. Chinma, C. E., Ariahu, C. C. & Alakali, J. S. Effect of temperature and relative humidity on the water vapour permeability and mechanical properties of cassava starch and soy protein concentrate based edible films. *J. Food Sci. Technol.* **52**, 2380–2386 (2015).
146. Wang, L., Qiu, J., Sakai, E. & Wei, X. Effects of multiwalled carbon nanotube mass fraction on microstructures and electrical resistivity of polycarbonate-based conductive composites. *Sci. Eng. Compos. Mater.* **24**, 163–175 (2017).

147. Zhang, P. *et al.* Dispersion of multi-walled carbon nanotubes modified by rosemary acid into poly(vinyl alcohol) and preparation of their composite fibers. *RSC Adv.* **5**, 55492–55498 (2015).
148. Wu, S. *Polymer Interface and Adhesion*. M. Dekker. (1982).
149. Wu, S. Interfacial Energy, Structure, and Adhesion between Polymers. in *Polymer Blends* 243–293 (Elsevier, 1978). doi:10.1016/B978-0-12-546801-5.50012-8.
150. Petke, F. D. & Ray, B. R. Temperature dependence of contact angles of liquids on polymeric solids. *J. Colloid Interface Sci.* **31**, 216–227 (1969).
151. Grigorescu, R. M. *et al.* Mechanical and dielectric properties of SEBS modified by graphite inclusion and composite interface. *J. Phys. Chem. Solids* **89**, 97–106 (2016).

# Curriculum Vitae

Email: [chaoqun.dong@epfl.ch](mailto:chaoqun.dong@epfl.ch)

Tel: +41 21 69 32907

Address: EPFL-STI-IMX-FIMAP, MXG 334, Station 12, CH-1015 Lausanne, Switzerland

## Education

---

- 10/2016 – now      **PhD, École polytechnique fédérale de Lausanne (EPFL)**, Lausanne, Switzerland
- Materials Science & Engineering, Laboratory of Photonic Materials and Fiber Devices
  - Advisor: Prof. Fabien Sorin
- 09/2013 – 06/2016      **Master, Shandong University**, Jinan, China
- Materials Science & Engineering, Key Laboratory for Liquid-Solid Structural Evolution and Processing of Materials
  - Advisor: Zhonghua Zhang
- 09/2009 – 06/2013      **Bachelor, University of Jinan**, Jinan, China
- Materials Science & Engineering
  - Advisor: Yan Wang    GPA ranking: 1/484

## Research Experience

---

### *École polytechnique fédérale de Lausanne (EPFL)*

- Super-elastic liquid metal based triboelectric fibers and textiles for energy harvesting and self-powered sensing.
- Self-encapsulated stretchable and waterproof multi-material fibers for energy harvesting.
- Flexible microstructured multi-material fibers for microfluidic sensing.
- *In-situ* crosslinked gelatin hydrogel fibers during thermal drawing for controlled drug release.
- Soft and stretchable transmission lines for measuring multiple types of deformations simultaneously.
- Stretchable and conductive polymer composite fibers and their application in mechanical sensing.

### *Shandong University*

- Dealloying-directed synthesis of mesoporous transition metal-based oxides/hydroxides for water splitting.
- Cu<sub>2</sub>O@Cu nanoneedle array electrodes for high-performance asymmetric supercapacitors.
- Nanostructured electrodes driven by anodization and electrochemical oxidation for glucose sensing.

## Skills

---

### *Materials fabrication and processing*

- thermal drawing, micro-extrusion, spin coating, dip-coating, thermal evaporation, sputtering, dealloying, melt spinning, hot-pressing, electrochemical anodization

### *Materials and devices characterization*

- XRD, SEM, TEM, XPS, BET, UTM, DMA, rheological properties, moisture vapor transmission test, sessile/pendant drop, gas chromatography, electrical characterization, electrochemical characterization

### *Software skills*

- finite-element analysis (Abaqus, Comsol), computer-aided design (AUTOCAD, Inventor), general-purpose programming (Matlab, Python-beginner), graphic design (Illustrator, Photoshop), data analysis

## Awards

---

- 2016, 2013      Outstanding Graduates Award of Shandong **Province**
- 2016, 2013      Outstanding Graduates Award of the university
- 2015            **National** Scholarship
- 2015, 2011      Merit Students/Postgraduates Award of the university

2015	Outstanding Academic Achievement of Shandong University
2013	Best Undergraduate Thesis Award of University of Jinan
2011, 2010	<b>National</b> Encouragement Scholarship
2011, 2010	First Class Scholarship of University of Jinan

## Research Guidance

I have trained and guided 2 master students and 1 bachelor for their scientific research and thesis at Shandong University and supervised 3 master students for their semester projects at EPFL.

## Publications

**Summary:** more than 20 papers in international peer reviewed journals.

**Citations:** 899    **h-index:** 16    **i10-index:** 17    [Link to Google Scholar Account](#)

*10 selected publications in peer-reviewed journals:*

1. **C. Dong**, A. Leber, T. Das. Gupta, M. Volpi, Y. Qu, T. Nguyen-Dang, N. Bartolomei, W. Yan, F. Sorin, "High-efficiency super-elastic liquid metal based triboelectric fibers and textiles", *Nature Communications*, 2020, 11, 3537.
2. A. Leber, **C. Dong**, R. Chandran, T.D. Gupta, N. Bartolomei, F. Sorin, "Soft and stretchable liquid metal transmission lines as distributed probes of multimodal deformations", *Nature Electronics*, 2020, 3, 316-326.
3. W. Yan, **C. Dong**, Y. Xiang, S. Jiang, A. Leber, G. Loke, W. Xu, C. Hou, S. Zhou, M. Chen, R. Hu, P.P. Shum, L. Wei, X. Jia, F. Sorin, X. Tao, G. Tao, "Thermally drawn advanced functional fibers: New frontier of flexible electronics", *Materials Today*, 2020, 35, 168-194.
4. **C. Dong**, A.G. Page, W. Yan, T. Nguyen-Dang, F. Sorin, "Microstructured Multimaterial Fibers for Microfluidic Sensing", *Advanced Materials Technologies*, 2019, 4, 1900417.
5. **C. Dong**<sup>#</sup>, L. Han<sup>#</sup>, C. Zhang, Z. Zhang, "Scalable dealloying route to mesoporous ternary CoNiFe layered double hydroxides for efficient oxygen evolution", *ACS Sustainable Chemistry & Engineering*, 2018, 6, 16096-16104. (**co-first author**)
6. Y. Chen<sup>#</sup>, **C. Dong**<sup>#</sup>, J. Zhang, C. Zhang, Z. Zhang, "Hierarchically porous Mo-doped Ni-Fe oxide nanowires efficiently catalyzing oxygen/hydrogen evolution reactions", *Journal of Materials Chemistry A*, 2018, 6, 8430-8440. (**co-first author**)
7. **C. Dong**, T. Kou, H. Gao, Z. Peng, Z. Zhang, "Eutectic-derived mesoporous Ni-Fe-O nanowire network catalyzing oxygen evolution and overall water splitting", *Advanced Energy Materials*, 2018, 8, 1701347. **Google Scholar Citations: 170.**
8. **C. Dong**, X. Yan, C. Si, H. Gao, W. Ma, G. Cheng, W. Yang, H. Zhong, Z. Zhang, "New-type nickel oxalate nanostructures for ultrahigh sensitive electrochemical biosensing of glucose", *Advanced Materials Interfaces*, 2016, 3, 1600197.
9. **C. Dong**, H. Zhong, T. Kou, J. Frenzel, G. Eggeler, Z. Zhang, "Three-dimensional Cu foam-supported single crystalline mesoporous Cu<sub>2</sub>O nanothorn arrays for ultra-highly sensitive and efficient nonenzymatic detection of glucose", *ACS Applied Materials & Interfaces*, 2015, 7, 20215-20223. **Google Scholar Citations: 84.**
10. **C. Dong**, Y. Wang, J. Xu, G. Cheng, W. Yang, T. Kou, Z. Zhang, Y. Ding, "3D binder-free Cu<sub>2</sub>O@Cu nanoneedle arrays for high-performance asymmetric supercapacitors", *Journal of Materials Chemistry A*, 2014, 2, 18229-18235. **Google Scholar Citations: 138.**

## Patents

2. F. Sorin, W. Esposito, V. Michaud, **C. Dong**, B. Çağlar, T. Nguyen-Dang, "Elongated microstructured capacitive sensors". US Patent. Application No: 19193949.5. Applied in September 2019.
1. Z. Zhang, **C. Dong**, G. Cheng, J. Xu, "A copper oxide based asymmetric supercapacitor and its fabrication method". Chinese Patent. Patent No: ZL201410102347.7.

## Conference Oral Presentations

- *Materials Research Society (MRS), 2019 Fall meeting* Boston, USA 2019  
Title: Thermal Drawing of Stretchable Triboelectric Fibers for Efficient Energy Harvesting
- *European Materials Research Society (EMRS), 2019 Spring meeting* Nice, France 2019  
Title: Thermal Drawing of Intrinsically Stretchable Triboelectric Fibers